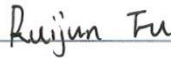


# Empirical RF Propagation Modeling of Human Body Motions for Activity Classification

A Thesis Submitted to the Faculty of  
WORCESTER POLYTECHNIC INSTITUTE  
in partial fulfillment of the requirements for the  
Degree of Master of Science

In  
Electrical and Computer Engineering

By

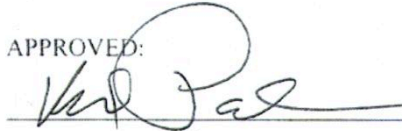


Ruijun Fu

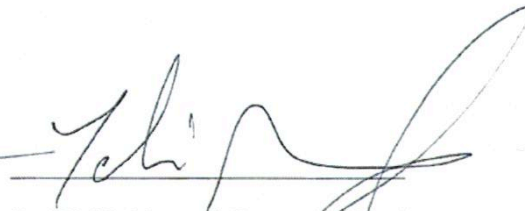
(rjfu@wpi.edu)

November 2012

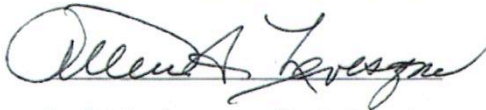
APPROVED:



Prof. Kaveh Pahlavan, Thesis Advisor



Prof. Yehia Massoud, Department Head



Prof. Allen Levesque, Thesis Committee



Prof. Sergey Makarov, Thesis Committee



Dr. Kamran Sayrafian, NIST, Thesis Committee

For My Beloved Families

# Table of Contents

1	Introduction.....	11
1.1	Background.....	11
1.2	Motivation.....	13
1.3	Contribution of the Thesis .....	15
1.4	Outline of the Thesis.....	17
2	Background and Methodology of Channel Modeling.....	19
2.1	Channel Modeling.....	19
2.2	Path Loss Channel Model.....	21
2.3	Fading.....	23
2.4	Power Spectral Density.....	23
2.5	Statistical Description of Received Power.....	24
2.6	Experimental Method .....	25
2.6.1	Measurement Environment .....	25
2.6.2	Measurement Setup.....	26
3	Propagation Characteristics of Human Body Motions.....	30
3.1	Path Loss Model .....	30
3.2	Statistical Analysis of Human Body Motions.....	34
3.3	First Order Statistical Characterization.....	34
3.4	Second Order Statistical Characterization .....	43
3.4.1	Level Crossing Rate .....	44
3.4.2	Average Fade Duration .....	46
3.4.3	Outage Probability.....	48
3.5	Doppler Spread Spectrum.....	48
3.6	RMS Doppler Spread.....	52
3.7	Shape of Doppler Spread Spectrum.....	53
3.8	Coherence Time.....	57
4	Activity Classification with Inertial Sensors.....	59
4.1	Sensors on Smartphones .....	59
4.2	Behavior of Sensors.....	60
4.2.1	Data Collection.....	60
4.2.2	Mean and Variance.....	63
4.2.3	Energy .....	63
4.2.4	Frequency-domain entropy.....	63
4.3	Activity Classification .....	64
4.3.1	Activity Recognition Architecture and Methods.....	64
4.3.2	Feature Extraction .....	66
4.3.3	Backpropagation Network.....	66
4.3.4	Probabilistic Neural Network (PNN) .....	68
4.3.5	$k$ -Nearest Neighbor ( $k$ -NN).....	69
4.3.6	Support Vector Machine (SVM).....	70
5	Conclusion and Future Work.....	72
5.1	Conclusion .....	72
5.2	Future Work.....	73
6	Reference .....	74
7	Appendix.....	81
7.1	Appendix I: Time Domain and Frequency Domain Data .....	81
7.2	Appendix II: Statistical Distribution.....	83
7.3	Appendix III: Level Crossing Rate .....	86
7.4	Appendix IV: Averaged Fade Duration.....	88
7.5	Appendix V: Coherence Time .....	91

## Abstract

Many current and future medical devices are wearable, using the human body as a conduit for wireless communication, which implies that human body serves as a crucial part of the transmission medium in body area networks (BANs). Implantable medical devices are designed to provide patients with timely monitoring and clinical diagnostic tools to detect physiological abnormalities. Body-mounted sensors are investigated for use in providing a ubiquitous monitoring environment. In order to better design these medical devices, it is important to understand the propagation characteristics of channels for in-body and on-body wireless communication in BANs.

This thesis is focused on the propagation characteristics of human body movements. Specifically, standing, walking and jogging motions are measured, evaluated and analyzed using an empirical approach. Using a network analyzer, probabilistic models are derived for the communication links in the medical implant communication service band (MICS), the industrial scientific medical band (ISM) and the ultra-wideband (UWB) band. Statistical distributions of the received signal strength and second order statistics are presented to evaluate the link quality and outage performance for on-body to on-body communications at different antenna separations. The Normal distribution, Gamma distribution, Rayleigh distribution, Weibull distribution, Nakagami-m distribution, and Lognormal distribution are considered as potential models to describe the observed variation of received signal strength. Doppler spread in the frequency domain and coherence time in the time domain from temporal variations is analyzed to characterize the stability of the channels induced by human body movements. The shape of the Doppler spread spectrum is also investigated to describe the relationship of the power and frequency in the frequency domain. All these channel characteristics could be used in the design of communication protocols in BANs, as well as providing features to classify different human body activities.

Realistic data extracted from built-in sensors in smart devices were used to assist in modeling and classification of human body movements along with the RF sensors. Variance, energy and frequency domain entropy of the data collected from accelerometer and orientation sensors are pre-processed as features to be used in machine learning algorithms. Activity classifiers with Backpropagation Network, Probabilistic Neural Network,  $k$ -Nearest Neighbor algorithm and Support Vector Machine are discussed and evaluated as means to discriminate human body motions. The detection accuracy can be improved with both RF sensors and inertial sensors.

## Acknowledgement

First of all, I would like to thank to my advisor Professor Kaveh Pahlavan for his great guidance and support in my research and life. He is far more than a wisdom advisor to me. He does not only teach me the insight, knowledge and attitude, but also enlighten me with his true philosophy of academics and life. I would not accomplish this thesis without his guidance and encouragement in the past two years.

I am also greatly thankful to my dissertation members, Professor Allen Levesque, Dr. Kamran, Professor Yehia Massoud and Professor Sergey Makarov for their guidance and review of my thesis. Their comments and assistance are extremely precious in finalizing this thesis.

I shall extend my thanks to all my colleagues at CWINS lab: Ferit Ozan Akgul, Yunxing Ye, Yi Wang, Umair Khan, Dr. Ning Yang, Monirul Islam, Jie He, Shen Li, Pranay Swar, Dr. Kaveh Ghabooshi, GuanQun Bao, Xin Zheng, Yishuan Geng and other colleagues for their help and kindness while I was completed my Master Degree.

I would like to express my sincere gratitude to my best friends: Yuan Li, Rui Pang, Xiaodong Huang, Sisi Luo, Qingping Yu, Qi Ao, Zhenyu Yang and Hanfei Zhao for their encouragement and understanding in the past years. And our friendships would be everlasting.

Last but not least, my heartfelt appreciation goes out to all my families. Grateful thanks go to my dear husband Dr. Ning Cao. I would not come to this point without his support, understanding and help. I would also like to send my deepest appreciation to my father Genfa Fu, my mother Yali Yang, my uncle Yaan Yang, my aunt Xiaolin Xing, my brother-in-law Fan Yang and my dearest grandfather Jiesan Yang for their continuous love to me in the past twenty years. Special thanks also go to my father-in-law Fengjin Cao and mother-in-law Enying Liang. This thesis is dedicated to all my families.

# List of Figures

Figure 1: Possible Communication Links for Body Area Network.....	20
Figure 2: Power Spectral Density .....	24
Figure 3: Experimental Environment.....	25
Figure 4: Experimental Environment.....	26
Figure 5: Three Sets of Antenna used in Measurement.....	27
Figure 6: Agilent E8363B Vector Network Analyzer.....	28
Figure 7: Antenna placement on the surface of human body.....	29
Figure 8: Time Domain Data for Standing, Walking and Jogging Motions, Left Ankle to Right Hip, 2.25GHz.....	31
Figure 9: Maximum, Minimum and Mean of Path Loss at 400 MHz, 2.25 GHz, 4.5 GHz for Standing Motion .....	32
Figure 10: Cumulative Distribution Function Fittings for the transmission link from left ankle to right hip of at 2.25 GHz for standing, walking and jogging movements .....	38
Figure 11: Second Order Statistics: Level-Crossing Rate and Fade Duration.....	44
Figure 12: Level Crossing Rate for Scenario Set S1 .....	45
Figure 13: Fade Duration for Scenario Set S1 .....	47
Figure 14: Time Domain and Frequency Domain Analysis of Scenario Set S1.....	50
Figure 15: Shape of Doppler Spread Spectrum for Scenario Set S2 .....	55
Figure 16: Coherence Time for Scenario Set S1 .....	58
Figure 17: Coordinate System that is used by the Android Smartphones .....	59
Figure 18: Time Domain data of accelerometer sensor.....	61
Figure 19: Time Domain data of orientation sensor.....	62
Figure 20: Activity Classification Architecture .....	64
Figure 21: Propagation Network Architecture .....	67
Figure 22: Performance Validation.....	67
Figure 23: Neural Network Architecture for Classification .....	68
Figure 24: Time Domain and Frequency Domain, Back to Right Hip, Standing, Walking, Jogging, 400 MHz.....	81
Figure 25: Time Domain and Frequency Domain, Left Wrist to Right Hip, Standing, Walking, Jogging, 400 MHz.....	81
Figure 26: Time Domain and Frequency Domain, Left Ankle to Right Hip, Standing, Walking, Jogging, 400 MHz....	81
Figure 27: Time Domain and Frequency Domain, Right Ankle to Right Hip, Standing, Walking, Jogging, 400 MHz .	81
Figure 28: Time Domain and Frequency Domain, Back to Right Hip, Standing, Walking, Jogging, 2.25 GHz .....	82
Figure 29: Time Domain and Frequency Domain, Left Wrist to Right Hip, Standing, Walking, Jogging, 2.25 GHz ....	82
Figure 30: Time Domain and Frequency Domain, Left Ankle to Right Hip, Standing, Walking, Jogging, 2.25 GHz ...	82
Figure 31: Time Domain and Frequency Domain, Right Ankle to Right Hip, Standing, Walking, Jogging, 2.25 GHz .	82
Figure 32: Time Domain and Frequency Domain, Back to Right Hip, Standing, Walking, Jogging, 4.5 GHz .....	82
Figure 33: Time Domain and Frequency Domain, Left Wrist to Right Hip, Standing, Walking, Jogging, 4.5 GHz .....	83
Figure 34: Time Domain and Frequency Domain, Left Ankle to Right Hip, Standing, Walking, Jogging, 4.5 GHz .....	83
Figure 35: Time Domain and Frequency Domain, Right Ankle to Right Hip, Standing, Walking, Jogging, 4.5 GHz ...	83
Figure 36: Statistical Distribution, Back to Right Hip, Standing, Walking, Jogging, 400 MHz .....	83
Figure 37: Statistical Distribution, Left Wrist to Right Hip, Standing, Walking, Jogging, 400 MHz.....	83
Figure 38: Statistical Distribution, Left Ankle to Right Hip, Standing, Walking, Jogging, 400 MHz.....	84
Figure 39: Statistical Distribution, Right Ankle to Right Hip, Standing, Walking, Jogging, 400 MHz.....	84

Figure 40: Statistical Distribution, Back to Right Hip, Standing, Walking, Jogging, 2.25 GHz.....	84
Figure 41: Statistical Distribution, Left Wrist to Right Hip, Standing, Walking, Jogging, 2.25 GHz.....	84
Figure 42: Statistical Distribution, Left Ankle to Right Hip, Standing, Walking, Jogging, 2.25 GHz.....	84
Figure 43: Statistical Distribution, Right Ankle to Right Hip, Standing, Walking, Jogging, 2.25 GHz.....	85
Figure 44: Statistical Distribution, Back to Right Hip, Standing, Walking, Jogging, 4.5 GHz.....	85
Figure 45: Statistical Distribution, Left Wrist to Right Hip, Standing, Walking, Jogging, 4.5 GHz.....	85
Figure 46: Statistical Distribution, Left Ankle to Right Hip, Standing, Walking, Jogging, 4.5 GHz.....	85
Figure 47: Statistical Distribution, Right Ankle to Right Hip, Standing, Walking, Jogging, 4.5 GHz.....	85
Figure 48: Level Crossing Rate, Back to Right Hip, Standing, Walking, Jogging, 400 MHz.....	86
Figure 49: Level Crossing Rate, Left Wrist to Right Hip, Standing, Walking, Jogging, 400 MHz.....	86
Figure 50: Level Crossing Rate, Left Ankle to Right Hip, Standing, Walking, Jogging, 400 MHz.....	86
Figure 51: Level Crossing Rate, Right Ankle to Right Hip, Standing, Walking, Jogging, 400 MHz.....	86
Figure 52: Level Crossing Rate, Back to Right Hip, Standing, Walking, Jogging, 2.25 GHz.....	87
Figure 53: Level Crossing Rate, Left Wrist to Right Hip, Standing, Walking, Jogging, 2.25 GHz.....	87
Figure 54: Level Crossing Rate, Left Ankle to Right Hip, Standing, Walking, Jogging, 2.25 GHz.....	87
Figure 55: Level Crossing Rate, Right Ankle to Right Hip, Standing, Walking, Jogging, 2.25 GHz.....	87
Figure 56: Level Crossing Rate, Back to Right Hip, Standing, Walking, Jogging, 4.5 GHz.....	87
Figure 57: Level Crossing Rate, Left Wrist to Right Hip, Standing, Walking, Jogging, 4.5 GHz.....	88
Figure 58: Level Crossing Rate, Left Ankle to Right Hip, Standing, Walking, Jogging, 4.5 GHz.....	88
Figure 59: Level Crossing Rate, Right Ankle to Right Hip, Standing, Walking, Jogging, 4.5 GHz.....	88
Figure 60: Averaged Fade Duration, Back to Right Hip, Standing, Walking, Jogging, 400 MHz.....	88
Figure 61: Averaged Fade Duration, Left Wrist to Right Hip, Standing, Walking, Jogging, 400 MHz.....	89
Figure 62: Averaged Fade Duration, Left Ankle to Right Hip, Standing, Walking, Jogging, 400 MHz.....	89
Figure 63: Averaged Fade Duration, Right Ankle to Right Hip, Standing, Walking, Jogging, 400 MHz.....	89
Figure 64: Averaged Fade Duration, Back to Right Hip, Standing, Walking, Jogging, 2.25 GHz.....	89
Figure 65: Averaged Fade Duration, Left Wrist to Right Hip, Standing, Walking, Jogging, 2.25 GHz.....	89
Figure 66: Averaged Fade Duration, Left Ankle to Right Hip, Standing, Walking, Jogging, 2.25 GHz.....	90
Figure 67: Averaged Fade Duration, Right Ankle to Right Hip, Standing, Walking, Jogging, 2.25 GHz.....	90
Figure 68: Averaged Fade Duration, Back to Right Hip, Standing, Walking, Jogging, 4.5 GHz.....	90
Figure 69: Averaged Fade Duration, Left Wrist to Right Hip, Standing, Walking, Jogging, 4.5 GHz.....	90
Figure 70: Averaged Fade Duration, Left Ankle to Right Hip, Standing, Walking, Jogging, 4.5 GHz.....	90
Figure 71: Averaged Fade Duration, Right Ankle to Right Hip, Standing, Walking, Jogging, 4.5 GHz.....	91
Figure 72: Coherence Time, Back to Right Hip, Standing, Walking, Jogging, 400 MHz.....	91
Figure 73: Coherence Time, Left Wrist to Right Hip, Standing, Walking, Jogging, 400 MHz.....	91
Figure 74: Coherence Time, Left Ankle to Right Hip, Standing, Walking, Jogging, 400 MHz.....	91
Figure 75: Coherence Time, Right Ankle to Right Hip, Standing, Walking, Jogging, 400 MHz.....	92
Figure 76: Coherence Time, Back to Right Hip, Standing, Walking, Jogging, 2.25 GHz.....	92
Figure 77: Coherence Time, Left Wrist to Right Hip, Standing, Walking, Jogging, 2.25 GHz.....	92
Figure 78: Coherence Time, Left Ankle to Right Hip, Standing, Walking, Jogging, 2.25 GHz.....	92
Figure 79: Coherence Time, Right Ankle to Right Hip, Standing, Walking, Jogging, 2.25 GHz.....	92
Figure 80: Coherence Time, Back to Right Hip, Standing, Walking, Jogging, 4.5 GHz.....	93
Figure 81: Coherence Time, Left Wrist to Right Hip, Standing, Walking, Jogging, 4.5 GHz.....	93

Figure 82: Coherence Time, Left Ankle to Right Hip, Standing, Walking, Jogging, 4.5 GHz ..... 93  
Figure 83: Coherence Time, Right Ankle to Right Hip, Standing, Walking, Jogging, 4.5 GHz ..... 93

## List of Tables

Table 1 Channel Model Scenarios.....	20
Table 2: Implant to Implant (S1) for MICS.....	21
Table 3: Implant to Body Surface (S2) for MICS .....	21
Table 4: Average Path Loss (dB) .....	22
Table 5: Peak-to-through path loss variation.....	22
Table 6: Antenna Separations for on-body to on-body link .....	29
Table 7: Path Loss for 400 MHz .....	33
Table 8: Path Loss for 2.25 GHz.....	33
Table 9: Path Loss for 4.5 GHz .....	34
Table 10: Cumulative Distribution Fittings for 400 MHz, 2.25 GHz and 4.5 GHz.....	40
Table 11: Fitted Statistical Distribution for Each Scenario .....	43
Table 12: Level Crossing Rate .....	46
Table 13: Doppler Spread for All the Scenarios at 400 MHz, 2.25 GHz, 4.5 GHz.....	51
Table 14: Comparison of Doppler Spread for Scenario Set S2 .....	52
Table 15: Estimate Doppler Spread Shape for Scenario Set S .....	55
Table 16: Stability of Accelerometer Sensor.....	60
Table 17: Stability of Orientation Sensor .....	60
Table 18: Comparison of Different Machine Learning Algorithms .....	67

## Glossary

RF: Radio Frequency  
BANs: Body Area Network  
ICD: Implantable Cardiac Defibrillator  
MICS: Medical Implant Communication Service band  
ISM: Industrial Scientific and Medical band  
WMTS: Wireless Medical Telemetry Service  
UWB: Ultra-wideband  
VNA: Vector Network Analyzer  
PL: Path Loss  
PDF: Probability Density Function  
CDF: Cumulative Density Function  
RMS: Root Mean Square  
RSS: Received Signal Strength  
TG: Task Group  
CM: Channel Model  
LOS: Line of Sight  
NLOS: Non Line of Sight  
TX: Transmitter  
RX: Receiver  
PSD: Power Spectral Density  
PDP: Power Delay Profile  
MEMS: Micro-Electromechanical Systems  
HMM: Hidden Markov Model  
SVM: Support Vector Machine  
PNN: Probabilistic Neural Network  
BP: Back Propagation  
kNN:  $k$ -Nearest Neighbor  
GI: Gastrointestinal

# 1 Introduction

## 1.1 Background

In recent years, there has been a growing interest in Body Area Networks (BANs) for a variety of healthcare applications. The development of micro-electromechanical systems (MEMS) technology as well as the advancement in digital electronics and wireless communications made it possible to design small size, low cost, energy efficient, power scavenging, harmless medical and non-medical devices that could be placed inside or on the surface of the human body. Traditionally, healthcare monitoring is performed on a periodic check basis where the doctor must remember the symptoms, perform some tests and plan the diagnostic in the treatment in the hospital. And medical devices are usually attached to patients by wires. Many current and future medical devices are wearable and the human body is used as a conduit for wireless communication, which implies that the human body becomes a crucial part of the transmission medium in BANs <sup>[1, 2]</sup>. Implantable devices such as Endoscopy Capsule are also investigated to effectively detect abnormalities <sup>[4-7]</sup>. These new emerging technology enables the development of in-home assistance, smart nursing homes, and efficiently handling of emergency cases, where physicians could be aware of the patients' situations and prepare immediately for needed treatment <sup>[10]</sup>.

The healthcare applications of wireless networks can be divided into two main categories: in-body and on-body medical devices. On one hand, the in-body medical devices include Pacemaker, Endoscopy Capsule, Implantable Cardiac Defibrillator (ICD) <sup>[11]</sup>, Glucose Sensor, pH Monitor, etc. The Pacemaker performs daily remote monitoring and provides the patients with timely notification of emergency situation. This implantable, long-durable medical device is also capable of remote follow-up through back-end networks. Traditional clinical diagnostic of the stomach is performed with gastroscopy where the physicians operate with a long wire connected to the medical device on one end, while the needle camera on the other end is put into the mouth and goes from esophagus to stomach to detect problem problems in the stomach. Recently, the Endoscopy Capsule <sup>[12]</sup> replaces the wired apparatus in visualizing the stomach and small intestine to detect, diagnose and monitor abnormalities. This swallowable capsule does not only reduce the

patient's discomfort, but also increases the efficiency of the treatment from the physician's perspective. Moreover, the Implantable Cardiac Defibrillator is intended to protect patients against ventricular arrhythmias and helps patients to recover from inappropriate shocks. As a result, the patients are able to self-cure from unexpected accidents instead of waiting for an ambulance. On the other hand, the on-body medical devices include blood pressure sensor, motion sensor, temperature sensor, etc. As the percentage of elders grows in the whole population, "smart healthcare" is increasingly viewed as a means of assisting residents and caregivers by providing continuous medical monitoring, medical records access and emergency communication. Information on residents' health and life habits can be helpful for on-going diagnostics and future treatment. These in-body and on-body medical devices greatly help patients to recover from emergency situations while informing physicians of the patients' health status.

Many medical devices are emerging in the industrial fields. The GivenImaging company<sup>[12]</sup> has developed the PillCam platform to detect the abnormalities in the GI tract, along with pH monitoring to help treat gastroesophageal reflux disease, etc. The St. Jude Medical organization has provided patients with Pacemakers to perform daily monitoring, ICDs to efficiently deliver the right therapy at the right time, etc. At the same time, research projects are also carried out to solve the challenges in BANs. The UbiMon<sup>[13]</sup> is designed to provide a ubiquitous monitoring environment for wearable and implantable sensors. The CodeBlue<sup>[14, 15]</sup> is an ad hoc sensor network infrastructure for emergency medical care project developed at Harvard University. The MobiHealth<sup>[16]</sup> is a project based on a European initiative to create in-home healthcare assistance. However, challenges still remain to be solved in the research and industrial fields. The design and integration of Biosensor and system requires the medical device to be small in size, assuring reduced risk to body tissues. The lifetime of medical devices needs to be longer, achievable with the miniaturization of power sources. For the security issues, medical devices are potentially vulnerable to interference and intrusion, which can result in life-threatening situations as well as compromises of privacy. For system robustness, the failure of one node should be detectable and recoverable immediately to protect patients from harm. These key technologies are essential to future pervasive healthcare systems in BANs<sup>[17]</sup>.

The IEEE 802.15.6 Task Group 6 is working on the standardization of Body Area Networks <sup>[18-22]</sup>, include propagation characteristics and Medium Access Control protocols for the Medical Implant Communication Service (MICS) band, the Industrial Scientific and Medical (ISM) band and the Ultra-wideband (UWB) band. Seven channel models are defined in the standard specifications to describe the possible communication links for the implant node, body surface node and external node in BANs. Considering the effects of small scale fading, large scale fading and shadowing due to the energy absorption, reflection and diffraction by the body tissues, a variety of path loss models are statistically derived for different scenarios at all possible bands. A power delay profile (PDP) model for ultra-wideband is given along with the corresponding parameters. Except for the research of fading effects of the human body, real time channel measurements by use of a channel sounder has also been performed <sup>[23]</sup>. Various body surface positions and three human body motions are considered in this thesis. The Normal, Lognormal and Weibull distributions are considered as the possible statistical descriptions of the received power. The channel Power Spectral Density (PSD) is also discussed to show the frequency selective fading effects for standing and walking motions at different frequency bands and different antenna separations <sup>[22]</sup>.

But there are still many challenges in BANs, which call for increasing mobility, higher capacity and lower power consumption. In order to better design wireless devices for health care applications, it is essential to understand the propagation characteristics in BANs <sup>[24-36]</sup>. Furthermore, understanding the performance of on-body communication links is also important in designing and evaluating Medium Access Control protocols for specific scenarios <sup>[37, 38]</sup>.

## 1.2 Motivation

As more and more elders suffer from heart attack, stroke, Parkinson's syndrome <sup>[39]</sup> or paralysis, remote healthcare monitoring systems <sup>[40-43]</sup> become of increasing importance as means to notify and update physicians about the current status of their patients. Also patients could receive treatment immediately in emergency situations, which can be aided by accurate human body motion detection and wireless connection to the emergency alarm system in the hospital. In addition to in-hospital applications, there are also needs

to track daily steps, distance walked, calories burned, hours slept, stairs climbed in people's daily lives. A lot of mobile applications on the iPhone and on the Android devices are emerging online in the market to meet a variety of daily needs. Activity recognition would also improve localization accuracy in tracking a person's location inside a building or in a downtown area and updating positions in the navigation systems. Moreover, human body motion detection is appealing for application in the entertainment environment. For example, the inertial sensors are employed in Wii or PS3 to record, classify and visualize human motions via hand-held controllers.

With body mounted sensors, the human body motions can be recognized and remotely detected in a variety of situations. In BANs, temporal variations of the communication channel are related to body conditions, body motions, antenna positions, frequency bands and the surrounding environment. The general characterization of on-body fading channels can best be analyzed thoroughly in a scenario-based approach<sup>[23]</sup>. Among all the influenced factors mentioned above, the human body motion is a key factor leading to a greater variation of the communication channel. This RF propagation modeling of human body motions utilizing Receive Signal Strength (RSS) information obtained from narrowband measurements. This quantitative approach provides features for activity classification, with features extracted from inertial sensors in smart devices. A variety of human body motions can then be discriminated using pattern recognition algorithms.

A measurement campaign has been performed with regard to fading effects caused by body movements. Studies of propagation characteristics for these dynamic channels have been done in indoor environments at frequencies around 400 MHz<sup>[44]</sup>, 868 MHz<sup>[45, 46]</sup>, 2.4 GHz<sup>[47-49]</sup> and 5 GHz<sup>[50-53]</sup>. Measurements related to dynamic channels were conducted in an anechoic chamber, office room and hospital room using either a channel sounder in wideband experiments or a vector network analyzer (VNA) in narrowband experiments<sup>[54-66]</sup>. Some of past researches are analysis of on-body propagation effects, including the modeling of path loss (PL) model<sup>[18]</sup> for a variety of scenarios at 400 MHz, 600 MHz, 900 MHz, 2.4 GHz, and UWB bands. Some previous papers are concentrated on statistical characterization of channels for a given scenario by using a probability density function (PDF)<sup>[58]</sup>, that is Lognormal, Weibull, Nakagami-m and Gamma

distributions were considered to characterize on-body dynamic channels. Also cumulative distribution functions (CDFs) have been analyzed, where Nakagami-m distribution used to model indoor channels at 868 MHz. Other papers have concentrated on analysis of second-order temporal statistics <sup>[59]</sup> by extracting fading rate and fading duration from measurement data. Channel temporal stability is also discussed <sup>[60]</sup>. More other papers are researched on the dynamic channels induced by a variety of body movements <sup>[63-66]</sup>.

Starting with the quantitative description of human body movements, body motion detection algorithms can be investigated and derived to help in tracking human daily activities as well as a subject's consumed calories. Moreover, this health information is extremely important to patients and elder people, who may seek monitoring and treatment from physicians. A number of machine learning techniques have been studied and applied to activity recognition using features extracted from body mounted sensors such as accelerometer. Supervised learning algorithms are used for activity classification include a probabilistic approach (Naïve Bayes, Gaussian Mixture Model, Logic classifier), a geometric approach (Support Vector Machine, Nearest Neighbor mean, multilayer perceptron) or a binary decision approach (C4.5 Binary Decision Tree). Decision Table, IBL, C4.5 and Naïve Bayes classifiers are discussed and evaluated to discriminate a variety of activities using five accelerometers placed at hip, wrist, arm, ankle and thigh <sup>[67]</sup>. The unsupervised learning method includes Hidden Markov Model (HMM) which can be used to model simple activities. A chief goal of this approach is to determine the hidden state sequence that corresponds to the observed sequence. However, it can be difficult to classify complex or unfamiliar activities. Machine learning algorithms are investigated and evaluated as an approach to classify different human body activities, assisted with the features of RF sensor and inertial sensors.

### 1.3 Contribution of the Thesis

Though a considerable amount of prior research has been devoted to the channel modeling and motion detection in BANs, little of the work describes dynamic channels for human body motions in a quantitative and thorough manner. And no previous work applied these RF characteristics to the human body activity classification field.

This thesis is focused on the RF propagation modeling of human body motions using an empirical approach <sup>[1, 2]</sup>. The characteristics of on-body to on-body channel model, induced by continuous human body motions are measured and investigated for the purpose of activity classification. The measurements are performed in a shielded room which is constructed of thin metal. Based on a scenario approach, the probability distributions and the second order statistics are measured and analyzed case by case.

Three categories of scenario are investigated: standing, walking and jogging. The Rayleigh distribution is found not suitable to describe any of three human body movement scenarios. However, the Weibull distribution is considered as a suitable description of human body motions in most of the cases studied. The Lognormal distribution is found to provide a better fit for standing scenario in several cases, The Nakagami-m distribution is found to provide better fit for walking motion in several scenarios, and the Gamma distribution fits better in a few cases for jogging motions.

Doppler spread spectrum, RMS Doppler bandwidth and the shape of Doppler spread spectrum are measured and analyzed by the use of Vector Network Analyzer (VNA) to provide a quantitative description of different body motions. Doppler spread is the width of received spectrum when a single tone waveform has been transmitted, which provides information about the fading rate induced by human body movements. For the standing scenario, the Doppler spread is always below 1 Hz. For the walking motion, the Doppler spread is greater than that for the standing scenario around 3 Hz. The jogging motion will introduce maximum Doppler spread which is greater than 6 Hz. Also RMS Doppler bandwidth is used to describe the spectral distribution of the power. Doppler spread and RMS Doppler bandwidth are also of great importance to determine the maximum signaling rate allowable for coherence demodulation and to improve detection and optimize transmission at the physical layer. Coherence time, which is an alternative description of Doppler spread in the frequency domain, is analyzed in the time domain for different scenarios. The coherence time is usually below 90 *ms* for jogging motion, around 100 *ms* for walking motion and more than 200 *ms* for the standing scenario. Moreover, the shape of the Doppler spread spectrum is described with a Laplacian model, a 4<sup>th</sup> order Gaussian model and a 4<sup>th</sup> order Polynomial model. In comparing with the

RMSE of values found with the three shape models, it is found that most of the Doppler spread shape could be described with a 4<sup>th</sup> order Gaussian model for the power. Yet, several cases could also be described with a Laplacian model or a Polynomial model.

The propagation model effectively quantizes different body motions, which could be utilized to classify different human body movements. Additionally, with pervasive deployment of computing devices, smartphones are an option for use as the base station to communicate with implant devices and other medical devices. This thesis also investigates into the performance of motion sensors in the smart devices for use in body motion detection. The variance, energy and entropy of sensors are extracted as features for patterns recognition of human body motions. Combined with RSS features, Backpropagation, Probabilistic Neural Network,  $k$ -Nearest Neighbor algorithm are analyzed and evaluated as potential solutions to the activity classification problem with improved detection accuracy.

#### 1.4 Outline of the Thesis

Section 1 is the introduction of this thesis, describing the background, and motivation for the work, and summarizing the contribution of the thesis. Section 2 discusses prior work on channel modeling of BANs; path loss modeling, small scale fading, large scale fading and effects of multipath fading are described in this section. At the end of the section, the measurement environment, measurement equipment and measurement scenarios are described. Section 3 presents a thorough discussion of channel modeling using narrowband measurement experiment. In this section, probabilistic distributions of the received signal strength for different scenarios and second order statistics are investigated, including statistical distributions, fading rate and fading duration. The analysis of Doppler spread spectrum, Doppler spreads, Root Mean Square (RMS) Doppler spreads and coherence time are also investigated in this section. A set of time domain waveforms and frequency spectra are shown visually to compare Doppler spreads for different human body motions. Section 4 analyzes the performance of the inertial sensors in smart devices to be used as features in activity classification algorithms. Backpropagation,  $k$ -Nearest Neighbor ( $k$ -NN), Probabilistic Neural Network (PNN) and Support Vector Machine (SVM) are discussed and evaluated in this section. Finally,

conclusions are drawn to summarize propagation characteristics of channel modeling for human body motions in BANs. Section 5 discusses potential avenues of the future work.

## 2 Background and Methodology of Channel Modeling

### 2.1 Channel Modeling

The channel modeling is usually performed with an extensive physical measurement, where measurement system is a crucial part in the modeling. The measurement techniques, experimental environment, equipment, antennas and attenuators are also important factors in constructing the actual physical channel models. Traditionally, there are two physical measurement techniques: narrowband and wideband. In the narrowband communication, the data speed is lower than wideband communication, but it could provide stable long-range communication. But narrowband measurement could not differentiate directed path and undirected paths, so wideband measurement is more suitable in studying multi-path propagation. Different experimental environments may result in a variety of channel models due to the multipath effects. In the indoor environment, the transmitted signal arrives at the receiver from various directions over a multiplicity of paths <sup>[69, 70]</sup>, including directed path, reflected paths, diffracted paths, etc. Wireless communication from the transmitter to the receiver can be modeled with several paths, line-of-sight (LOS), non-line-of-sight (NLOS). The LOS is the directed path from the transmitter to the receiver. The NLOS is much more complex than LOS, where the multipath is caused by the effects from floors, walls, objects. The Ray Tracing method is derived to model multipath propagation from a geometric point of view, which is a simplified solution for the Maxwell's equation. The propagation effects are also closely related to the center frequency and radiation pattern of the transmitter and receiver. Taking consideration of the factors mentioned above, a relative accurately characterized channel model would be effective in design, assessment and installation of a radio network. And a lot of applications could be developed in the network.

IEEE 802.15.6 Task Group TG6 is intended to develop Body Area Networks for medical devices and non-medical devices that could be placed inside or on the surface of human body. The path loss is caused by the reflection, diffraction and absorption of the human body tissues. The small scale fading and large scale fading are a result of the structure of human body and body motions.

In order to describe the characterization of the electromagnetic wave propagation from the devices those are close to or inside the human body, TG6 group has defined three

types of nodes <sup>[18]</sup>.

- Implant node: A node that is placed inside the human body. This could immediately below the skin to further deeper inside the body tissue.
- Body Surface node: A node that is placed on the surface of human skin or at most 2 centimeters away.
- External node: A node that is not in contact with human skin, between a few centimeters up to 5 meters away from the body.

Seven scenarios are defined in which the medical devices will be operating <sup>[18]</sup>. These scenarios along with the location of the communication nodes are listed in Table 1, corresponding to different frequency bands. The scenarios are grouped into classes that can be represented by the same Channel Models (CM).

Table 1 Channel Model Scenarios

Scenario	Description	Frequency Band	Channel Model
S1	Implant to Implant	402 – 405 MHz	CM1
S2	Implant to Body Surface	402 – 405 MHz	CM2
S3	Implant to External	402 – 405 MHz	CM2
S4	Body Surface to Body Surface (LOS)	13.5, 50, 400, 600, 900 MHz 2.4, 3.1-10.6 GHz	CM3
S5	Body Surface to Body Surface (NLOS)	13.5, 50, 400, 600, 900 MHz 2.4, 3.1-10.6 GHz	CM3
S6	Body Surface to External (LOS)	900 MHz 2.4, 3.1-10.6 GHz	CM4
S7	Body Surface to External (NLOS)	900 MHz 2.4, 3.1-10.6 GHz	CM4

The communication distance varies from a few centimeters up to 5 meters. Possible communication links are shown in fig. 1 below.

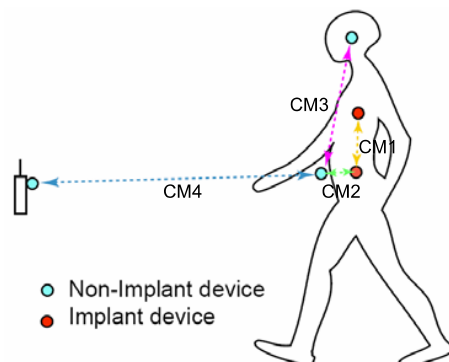


Figure 1: Possible Communication Links for Body Area Network

Based on various scenarios defined in the draft, we discuss some existing channel models from previous work, including path loss models and fading models.

## 2.2 Path Loss Channel Model

In traditional wireless communications, path loss model is both frequency and distance dependent. The channel path loss at a given time is given by

$$PL(t) = P_{tx} - P_{rx}(t) + G_{amplifier} - L_{cable} \quad (1)$$

where  $P_{tx}$  is the transmitted power,  $P_{rx}(t)$  is the RMS received power at given time  $t$ ,  $G_{amplifier}$  is amplifier gain and  $L_{cable}$  is cable loss.

Normally, the path loss is modeled from extensive physical experiments. A variety of measurements have been performed in channel modeling to characterize this power distance relationship. Since the physical measurement inside human body is not feasible, a 3D immersive simulation and visualization platform was developed to study the propagation characteristics of MICS <sup>[56]</sup>. A multi-thread loop antenna is used as the antenna for implant inside a male object in the simulation. A statistical path loss model has been derived in the form of the following equation.

$$PL(d) = PL(d_0) + 10n \log_{10} \left( \frac{d}{d_0} \right) + S \quad (2)$$

Where  $S \sim N(0, \sigma_s)$  and  $d_0 = 50mm$ . The parameters extracted for the implant to implant (S1) and implant to body surface (S2) are expressed in table 2 and table 3 <sup>[56]</sup>.

Table 2: Implant to Implant (S1) for MICS

Implant to Implant	$PL(d_0)$ (dB)	n	$\sigma_s$ (dB)
Deep Tissue	35.04	6.26	8.18
Near Surface	40.94	4.99	9.05

Table 3: Implant to Body Surface (S2) for MICS

Implant to Body Surface	$PL(d_0)$ (dB)	n	$\sigma_s$ (dB)
Deep Tissue	47.14	4.26	7.85
Near Surface	49.81	4.22	6.81

Various scenarios at different frequency bands (400 MHz, 600 MHz, 900 MHz, 2.4 GHz and UWB) and various transmission ranges have corresponding proposed path loss models and corresponding parameters for scenarios defined in table 1.

When it comes to the path loss model for different human body motions, it would be difficult to generalize a formal equation to represent the fading effects of the channels. Therefore, the channel variation at 800 MHz and 2.36 GHz are measured and discussed [71, 72] for different human body motions and antenna placement. The average path loss is shown in table 4 and the peak-to-through path loss variation is shown in table 5.

Table 4: Average Path Loss (dB)

(a) 820 MHz

	Receiver at Right Hip; Transmitter at:						Receiver at Chest; Transmitter at:		
	Chest	Right Wrist	Left Wrist	Right Ankle	Left Ankle	Back	Back	Right Wrist	Right Ankle
Standing	57.4	50.2	59.8	54.3	68.7	61.8	66.3	54.5	54.3
Walking	52.9	38.4	63.6	48.1	55.5	57.1	63.8	51.3	56.9
Running	44.1	37.2	60.2	48.9	54.2	62.3	66.3	49.4	54.1

(b) 820 MHz

	Receiver at Right Hip; Transmitter at:						Receiver at Chest; Transmitter at:		
	Chest	Right Wrist	Left Wrist	Right Ankle	Left Ankle	Back	Back	Right Wrist	Right Ankle
Standing	65.3	44.5	74.7	60.9	70.7	75.3	73.0	70.5	66.3
Walking	59.1	47.3	59.8	53.9	58.5	67.4	72.0	64.9	62.4
Running	55.9	36.3	52.5	55.0	59.0	68.5	71.7	57.4	63.3

Table 5: Peak-to-through path loss variation

(a) 2.36 GHz

	Receiver at Right Hip; Transmitter at:						Receiver at Chest; Transmitter at:		
	Chest	Right Wrist	Left Wrist	Right Ankle	Left Ankle	Back	Back	Right Wrist	Right Ankle
Standing	1.6	0.7	2.2	5.1	1.8	5.1	3.0	2.2	0.7
Walking	30.0	35.1	24.4	24.4	26.5	13.5	23.7	34.0	17.2
Running	38.0	45.6	28.0	32.8	27.9	23.8	30.9	27.8	32.5

(b) 2.36 GHz

	Receiver at Right Hip; Transmitter at:						Receiver at Chest; Transmitter at:		
	Chest	Right Wrist	Left Wrist	Right Ankle	Left Ankle	Back	Back	Right Wrist	Right Ankle
Standing	3.3	2.0	1.8	2.4	7.1	1.4	4.2	1.3	11.3
Walking	20.0	39.6	24.5	22.5	21.1	14.1	8.6	21.2	20.4
Running	30.3	46.8	33.7	28.4	24.1	16.3	9.3	29.4	19.5

### 2.3 Fading

In the Body Area Networks, the human body is used as a medium of communication, which may cause energy absorption, diffraction, reflection. The fading effects may be also caused by different body posture and surrounding environment.

The fading consists of small scale fading and large scale fading. Small scale fading refers to the fast changes in the amplitude and phase of received signal strength in a small local area. Large scale fading is the fading due to the motions in large area.

In IEEE 802.15.6 documents, the small scale fading is modeled as a Ricean distribution<sup>[18]</sup> with K factor that decreases as the path loss increases. The K factor is defined as:

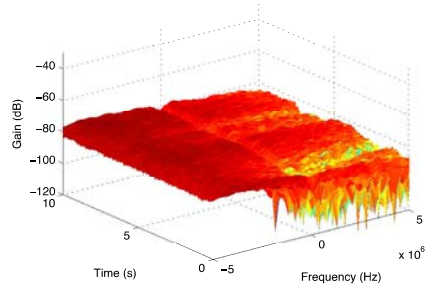
$$K_{dB} = K_0 - m_K P_{dB} + \sigma_K n_K \quad (3)$$

Where  $K_0$  is the fit with measurement data for the K-factor for low path loss,  $m_K$  is the slope of the linear correlation between path loss and K-factor,  $\sigma_K$  is the log-normal variance of the measured data between path loss and K-factor,  $n_K$  is the zero mean and unit variance Gaussian random variable and  $P_{dB}$  is the path loss in dB.

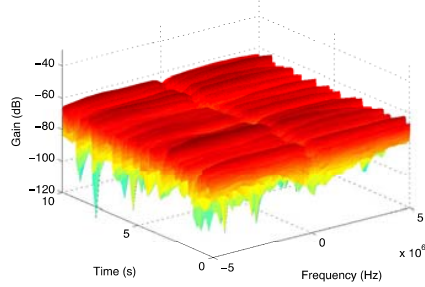
For the different scenarios defined in Table 1, the small scale fading is represented by Ricean distribution with corresponding parameters  $K_0$ ,  $m_K$ ,  $\sigma_K$  and  $n_K$ .

### 2.4 Power Spectral Density

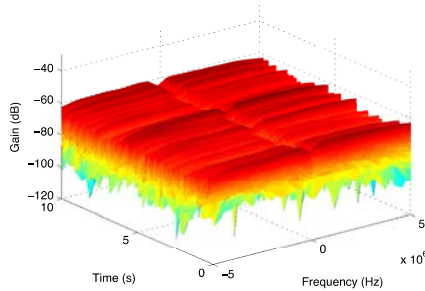
The channel's power spectral density (PSD) is a visual description of the channel response. PSD analysis of three common body motions is presented in [71] at 820 MHz and 2.36 GHz with illustration of figures. A 10s measurement for each scenario is performed with Vector Signal Generator, Vector Signal Analyzer, Low Noise Amplifiers and antennas for 802 MHz and 2.36 GHz. The power spectral density for each of  $40\mu s$  sample  $v$  is calculated by correlating  $v$  with a replica of the transmitted PN sequence and then applying a Fast Fourier Transform. The variation of PSD reflects the frequency-selective fading effects of channels and is consistent with the movement of the test subject. The PSD for the standing motion is generally flatter than those when the object is moving. And running movement caused more variation in the PSD than walking. An example of PSD for three human body motions is illustrated in Figure 2 below.



(a) Back to Right Hip, standing, 2.36 GHz



(b) Back to Right Hip, walking, 2.36 GHz



(c) Back to Right Hip, running, 2.36 GHz

Figure 2: Power Spectral Density

## 2.5 Statistical Description of Received Power

Channel Sounder has been used to perform the real-time channel measurements <sup>[59]</sup> in the anechoic chamber room at a center frequency of 4.5 GHz for body movements. The fading effects caused by human body motions are analyzed statistically. Normal distribution, log-normal distribution and Weibull distribution are considered as possible probability density functions, and are tried to fill the measurement results. The negative log likelihood is used to evaluate the fitting effects of the distributions. Moreover, link margin based performance is also analyzed to verify possible implementation and help in system design. The fade duration is defined as the continuous duration when the received

signal power drops below the mean of the received signal strength during the measurement and is fitted into Gamma distribution <sup>[18]</sup>. The fade magnitude, defined as the maximum fade depth with respect to the mean, is used as the indicator of the attenuation level a signal may encounter. And the level crossing rate is used to represent the statistics of the signal across into a fade when it next crosses into a fade.

## 2.6 Experimental Method

### 2.6.1 Measurement Environment

The channel measurements were performed by using two antennas placed on a test subject in a shielded room with a size of 2.32m × 2.41m × 2.29m at Center for Wireless Information Network Studies (CWINS) lab of Worcester Polytechnic Institute. The shielded room is designed to block external static and non-static electric fields and to provide a radio-silent environment. This copper room would keep RF energy within the cage rather than keep it out. The experimental environment is shown in Figure 3 with the relative location of the room and the test subject.

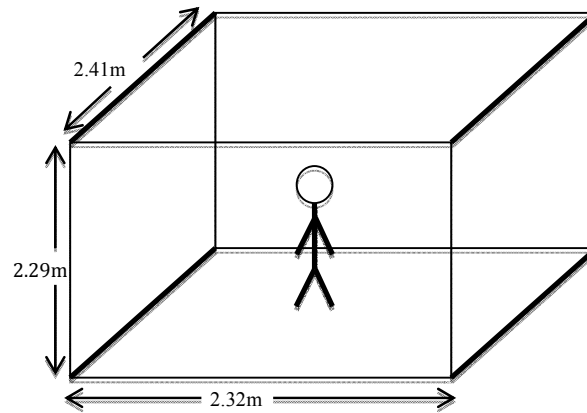


Figure 3: Experimental Environment

The real test environment is shown in Figure 4, where the shielded room is located inside CWINS lab and the RF sensors are mounted on the surface of human body. We investigated into the RF propagation modeling for the on-body to on-body communication links in this environment.



(a) Experimental Equipment and Test Subject



(b) Shielded Room

Figure 4: Experimental Environment

### 2.6.2 Measurement Setup

An extensive measurement is performed with the use of Agilent Vector Network Analyzer (VNA) to obtain  $S_{21}$  parameters. In the channel measurements, three sets of antennas are used during the measurements, all of which are omni-directionally working at 400 MHz, 2.25 GHz and 4.5 GHz within MICS, ISM and UWB bands. Antennas used for narrowband measurement at 400 MHz consist of a loop antenna as the receiver and a helical antenna as the transmitter; monopole antennas, working in a frequency band from 2.1 GHz to 2.4 GHz, are designated to send a single tone waveform at 2.25 GHz from transmitter to receiver; and patch antennas (SkyCross™ SMT-3TO10M-A) whose working frequency range is 3 GHz and 8 GHz are proposed to send and to receive a single tone waveform at 4.5 GHz. The three sets of antenna are shown in Figure 5 below.



(a) Loop Antenna and Helical Antenna Working at 400 MHz



(b) Monopole Antenna Working at 2.25 GHz



(c) Patch Antenna Working at 4.5 GHz

Figure 5: Three Sets of Antenna used in Measurement

Short time channel gain variations were measured using Agilent E8363B Vector Network Analyzer (VNA) shown in Figure 6. A continuous single tone signal waveform at 400 MHz, 2.25 GHz, and 4.5 GHz with a transmission power of 0 dBm was generated respectively by Transmission (TX) port of VNA in time domain. S21 Parameter, measured and stored in the PC in real time, was analyzed and evaluated off-line. In the 20 second interval, the network analyzer took samples of amplitudes of the received signal at the rate of 80 samples/s. Therefore the maximum Doppler shift measurable is 40 Hz, and resolution is 0.012 Hz.



Figure 6: Agilent E8363B Vector Network Analyzer

All measurements were based on different motions, where transmitting (TX) and receiving (RX) antennas were attached to different positions of human body. Using a scenario-based approach <sup>[23]</sup>, a scenario set, denoted by  $S = \{F, M, TX, RX\}$ , is composed of a frequency set  $F$ , a motion set  $M$  and two antenna position sets  $TX$  and  $RX$ . In the motion set, three different human movements have been measured: standing still, walking and jogging on a spot, denoted as  $M = \{\text{Stand, Walk, Jog}\}$ . Only respiration and palpitation exist when the human body is standing still. For the walking cycle, the human body is walking with arms and feet moving slowly and repeatedly in a small range. When the human body is jogging, both arms and feet moved back and forth very quickly, which would cause greater channel fluctuation. The frequency set  $F$  is composed of  $F = \{400 \text{ MHz, } 2.25 \text{ GHz, } 4.5 \text{ GHz}\}$ , where the increasing frequency of transmitters would have impact on small scale fading characteristics of body area network.

The transmitting and receiving antennas are placed at different positions on the test subject's body. For the on body to on body communication, the receiver is fixed at the right hip of the test subject, since the coordinator in the BANs is often considered as the center to receive data from other sensors in-body or on-body. The receiver set is  $RX = \{\text{Right Hip}\}$ . And the transmitter is strapped to Back, Left Wrist, Left Ankle and Right Ankle, represented by  $TX = \{\text{Back, Left Wrist, Left Ankle, Right Ankle}\}$ . The communication link between right ankle and right hip is Line-of-Sight (LOS) propagation, while other communication links from left wrist, left ankle and back to right hip are considered as Non-Line-of-Sight (NLOS) propagation. Figure 7 shows the locations of antennas on the tested subject. The blue points indicate the possible transmitter antenna position and the red point is the receiver antenna placement.

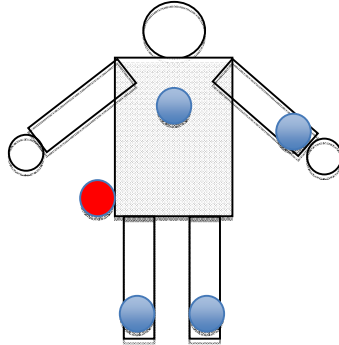


Figure 7: Antenna placement on the surface of human body

The antenna separation among these body mounted sensors is shown in Table 6. Different transmission range would have different impact on the path loss, as will be discussed in the next chapter.

Table 6: Antenna Separations for on-body to on-body link

TX	Back	Left Wrist	Left Ankle	Right Ankle
Antenna separation (mm)	88.90	111.76	139.69	121.92

### 3 Propagation Characteristics of Human Body Motions

#### 3.1 Path Loss Model

According to the path loss model <sup>[72]</sup>, the statistical path loss model has been derived in the form of the following equation.

$$PL(d) = PL(d_0) + 10\alpha \log_{10}(d) \quad (4)$$

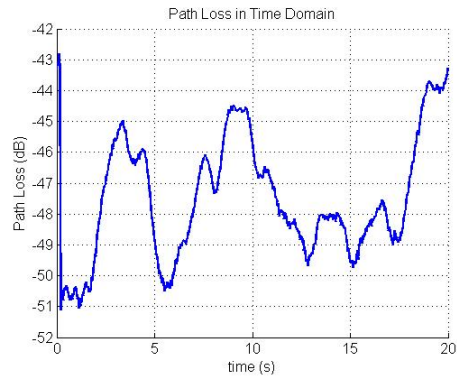
where  $PL(d_0) = 10\log_{10}\left(\frac{P_t}{P_0}\right) = -10\log_{10}G_tG_r\left(\frac{\lambda}{4\pi}\right)^2$ , which is the path loss in the first meter. The path loss is closely related to the antenna separation and it changes slowly with the distance between the transmitter and receiver.

In this section, we present path loss models for the relationship between the averaged received power and the distance between the transmitter and the receiver. This distance-power relationship could be used for coverage among these body mounted medical devices. Using VNA, the path loss  $PL(d)$  in  $dB$  from the transmitter to receiver is obtained by:

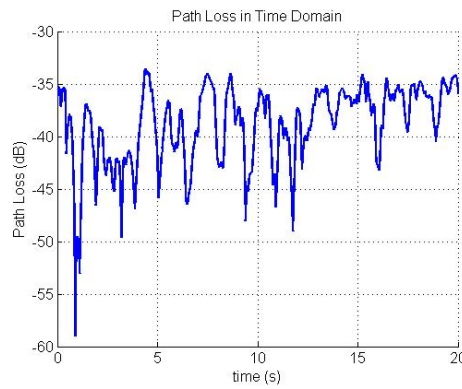
$$PL(d) = 20\log |S_{21}| \quad (5)$$

Where  $S_{21}$  is the scalar linear gain. This is simply scalar voltage gain as the linear ratio of the output voltage and the input voltage.

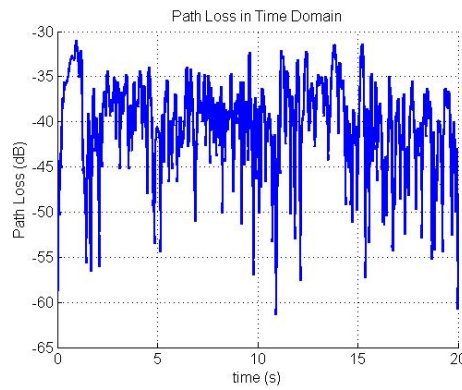
For the dynamic channels caused by human body movements, it is very difficult to derive a fixed distance-power relationship. Therefore we analyze the maximum path loss, the minimum path loss, the mean and the variance for each scenario. For scenario set S1 =  $\{2.25\text{GHz}\}$ ,  $\{\text{Stand, Walk, Jog}\}$ ,  $\{\text{Left Ankle}\}$ ,  $\{\text{Right Hip}\}$ , the time domain data are shown in Figure 8 below, where the antenna separation is 139.69 mm in static scenario. The path loss varies in a range of 8.2925 dB for standing, 25.4256 dB for walking, 30.4314 dB for jogging. The variation of path loss also increments when the intensity of motion increases.



(a) Path Loss for Stand Motion



(b) Path Loss for Walking

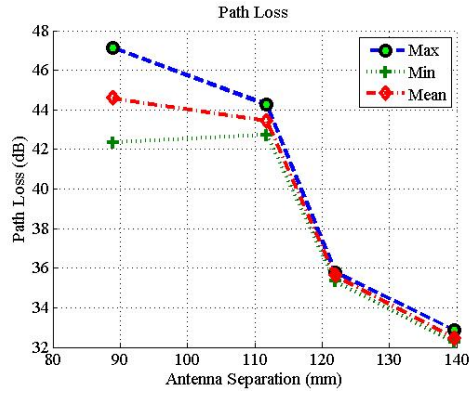


(c) Path Loss for Jogging

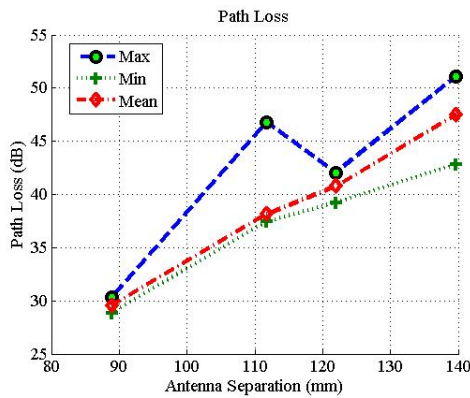
Figure 8: Time Domain Data for Standing, Walking and Jogging Motions, Left Ankle to Right Hip, 2.25GHz.

The summarized results for all the scenarios are shown in Table 7 for 400 MHz, Table 8 for 2.25 GHz and Table 9 for 4.5 GHz. For different antenna separations, the relationship between path loss and antenna separation for the standing motion are shown in Figure 9 below. In the free-space, the path loss is proportional to the logarithm of the antenna

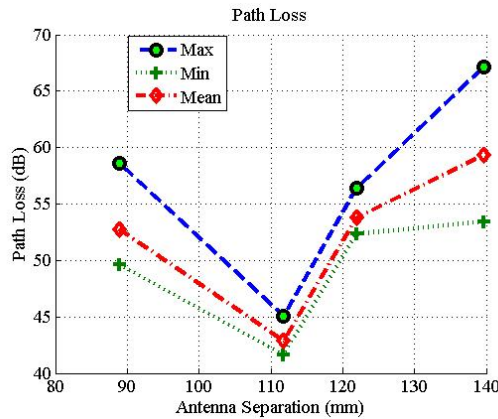
separation. When we consider the path loss for different human body motions, it does not vary according to the path loss model described in eq.4. For the 400 MHz, the channel suffers from deep fading when the transmitter antenna is placed at the back of human body, where breathing is the most influencing factor.



(a) Path Loss at 400 MHz for Standing



(b) Path Loss at 2.25 GHz for Standing



(c) Path Loss at 4.5 GHz for Standing

Figure 9: Maximum, Minimum and Mean of Path Loss at 400 MHz, 2.25 GHz, 4.5 GHz for Standing Motion

As the intensity of motions increases, the upper bound of path loss increases and the lower bound of path loss decrements. Except the range characteristics, the mean and variance of path loss in time domain is also statistically analyzed to provide as an indication of different motions. Table 7, 8 and 9 also shows the mean and variance for different center frequency. The range of path loss data varies considerably between different movements. The variation is an important feature when attempting to distinguish between possible motions.

Table 7: Path Loss for 400 MHz

Antenna Position	Motion	Maximum Path Loss (dB)	Minimum Path Loss (dB)	Path Loss Range	Path Loss mean (dB)	Path Loss Variation
Back	Stand	47.1488	42.3669	4.7818	44.5848	0.9889
	Walk	59.7022	45.5456	14.1566	49.8408	6.5676
	Jog	81.8554	42.3287	39.5267	53.9787	25.3460
Left Wrist	Stand	44.258	42.7338	1.5242	43.4391	0.1053
	Walk	44.0262	30.6025	13.4237	34.9540	5.3646
	Jog	49.5456	30.1517	19.3939	38.2696	11.0196
Left Ankle	Stand	32.8673	32.2366	0.6307	32.4562	0.0159
	Walk	35.0065	30.0469	4.9596	31.5253	0.9651
	Jog	42.7912	28.3675	14.4238	32.7367	7.7416
Right Ankle	Stand	35.7959	35.3448	0.4512	35.6182	0.0077
	Walk	46.8073	33.1908	13.6165	38.3890	8.0918
	Jog	43.2125	24.0535	19.1590	28.8432	11.0716

Table 8: Path Loss for 2.25 GHz

Antenna Position	Motion	Maximum Path Loss (dB)	Minimum Path Loss (dB)	Path Loss Range	Path Loss mean (dB)	Path Loss Variation
Back	Stand	30.3085	28.8099	1.4986	29.5321	0.1874
	Walk	47.9087	28.9765	18.9321	34.9060	7.8953
	Jog	64.4396	31.8968	32.5428	41.3900	24.4960
Left Wrist	Stand	46.8056	37.4452	9.3604	38.1361	0.3522
	Walk	57.0295	30.8259	26.2035	40.9452	18.7119
	Jog	59.6926	25.9274	33.7652	35.2925	24.7338
Left Ankle	Stand	51.1067	42.8142	8.2925	47.5087	3.7828
	Walk	59.006	33.5534	25.4526	38.9877	14.1840
	Jog	61.4071	30.9757	30.4314	40.7798	27.0567
Right Ankle	Stand	42.0613	39.1789	2.8824	40.7668	0.5338
	Walk	78.34	31.0109	47.3291	39.1497	41.8973
	Jog	56.2398	28.6039	27.6359	38.6875	23.8783

Table 9: Path Loss for 4.5 GHz

Antenna Position	Motion	Maximum Path Loss (dB)	Minimum Path Loss (dB)	Path Loss Range	Path Loss mean (dB)	Path Loss Variation
Back	Stand	58.5983	49.6259	8.9724	52.7215	3.5503
	Walk	83.6773	45.6699	38.0074	54.8756	25.4209
	Jog	77.3137	44.3949	32.9188	55.9779	32.7843
<hr/>						
Left Wrist	Stand	45.0966	41.6227	3.4739	42.8875	0.9854
	Walk	74.6919	42.9598	31.7321	52.2063	30.2601
	Jog	70.3539	43.0998	27.2540	54.0882	22.5069
<hr/>						
Left Ankle	Stand	67.158	53.4394	13.7187	59.3197	7.6558
	Walk	74.6117	42.9559	31.6558	52.5264	27.4258
	Jog	75.8169	44.4109	31.4060	54.5276	22.6047
<hr/>						
Right Ankle	Stand	56.3956	52.3496	4.0460	53.7640	0.8707
	Walk	74.3064	42.1481	32.1583	50.4317	19.0877
	Jog	72.6759	43.0925	29.5835	52.6473	21.9299

### 3.2 Statistical Analysis of Human Body Motions

The statistical characterization of the channels is based on the received signal amplitude, which are needed for the calculation of the average error rate for different transmission techniques over a fading wireless channel. To calculate the error rate, it is important to understand the error rate behavior over the statistics of fading channels. We take consideration of the varying body movements, different frequencies and various antenna positions into account. Normal, Gamma, Rayleigh, Weibull, Nakagami-m and Lognormal distributions are considered as the potential fading statistical distributions for body movements. Averaged fade duration, level crossing rate and outage probability are also discussed to provide accurate parameters for body area communication system design. Furthermore, the Doppler spread, Root Mean Squared (RMS) Doppler spread and coherence time are evaluated to provide a quantitative description to be used for activity classification.

### 3.3 First Order Statistical Characterization

According to different measurement scenarios, the statistical distributions of the envelop fading are summarized for each of the scenario, where effects of human body motions, antenna positions, and transmission frequencies are all taken into account in this section. The Normal, Gamma, Rayleigh, Weibull, Nakagami-m and Lognormal distributions are

considered as potential statistical models for received signal strength in time domain. Probability Density Function (PDF) of these six common probabilistic distributions are described below <sup>[69]</sup>.

- Normal distribution

$$f(x|\mu, \sigma) = \frac{1}{\sigma\sqrt{2\pi}} \exp\left\{-\frac{(x-\mu)^2}{2\sigma^2}\right\} \quad (6)$$

where  $\mu$  is the mean,  $\sigma^2$  is the variance and  $x$  is the envelope amplitude of the received power. The normal distribution suggests the averaged received signal strength forms the Gaussian distribution function. The cumulative distribution function (CDF) of normal distribution is given by

$$F(x; \mu, \sigma) = \frac{1}{2} \left[1 + \operatorname{erf}\left(\frac{x-\mu}{\sqrt{2}\sigma}\right)\right] \quad (7)$$

- Gamma distribution

$$f(x|a, b) = \frac{1}{b^a \Gamma(a)} x^{a-1} \exp\left\{-\frac{x}{b}\right\} \quad (8)$$

where  $a$  is the shape parameter,  $b$  is the scale parameter and  $x$  is the envelope amplitude of the received signal. The cumulative distribution function of Gamma function is given by

$$F(x; a, b) = \frac{1}{\Gamma(a)} \gamma(a, \frac{x}{b}) \quad (9)$$

- Rayleigh distribution

$$f(x|\sigma) = \frac{x}{\sigma^2} \exp\left\{-\frac{x^2}{2\sigma^2}\right\}, \quad x \in \{0, +\infty\} \quad (10)$$

where  $x$  is the envelope amplitude of received signal,  $\sigma^2$  is the mean power of the received signal. Rayleigh distribution is the most popular distribution function used for statistical modeling of the envelop fading of radio signals. And it is considered as a reasonable envelop fading channel model of a received signal for mobile communication systems. The cumulative distribution function of Rayleigh distribution is given by

$$F(x; \sigma) = 1 - e^{-x^2/2\sigma^2} \quad (11)$$

- Weibull distribution

$$f(x|\gamma) = \begin{cases} \frac{k}{\gamma} \exp\left\{-\left(\frac{x}{\gamma}\right)^k\right\} & x \geq 0 \\ \mathbf{0} & \textit{otherwise} \end{cases} \quad (12)$$

where  $x$  is the envelope amplitude of received signal,  $k$  is the shape factor,  $\gamma$  is the scale factor. Both the shape and scale factors are positive to characterize the Weibull distribution. The Weibull distribution is considered to show a good fit to experimental fading channel measurements in outdoor environments. Weibull distribution also exhibits a good fit for some cases on-body channel fading models. The cumulative distribution function of Weibull distribution is given by

$$F(x; \gamma) = \mathbf{1} - e^{-(x/\gamma)^k} \quad (13)$$

- Nakagami-m distribution

$$f(x|\mathbf{m}, \omega) = \frac{2m^m}{\Gamma(m)\omega^m} x^{2m-1} \exp\left\{-\frac{m}{\omega} x^2\right\} \quad (14)$$

where  $\Gamma(\cdot)$  is the Gamma function,  $x$  is the envelope amplitude of received signal,  $m$  is the shape factor and  $\omega$  is a controlling speed. A special case is when  $m = 1$ , Nakagami-m fading performs similar as Rayleigh fading with an exponentially distributed power. Nakagami-m distribution <sup>[73]</sup> is regarded as the best fit to some urban multipath measurements occasionally. The cumulative distribution function of Namagami-m distribution is given by

$$F(x; \mathbf{m}, \omega) = \frac{\gamma(m, \frac{m}{\omega} x^2)}{\Gamma(m)} \quad (15)$$

- Lognormal distribution

$$f(x|\mu, \sigma) = \frac{1}{x\sigma\sqrt{2\pi}} \exp\left\{-\frac{(\ln x - \mu)^2}{2\sigma^2}\right\} \quad x \in \{\mathbf{0}, +\infty\} \quad (16)$$

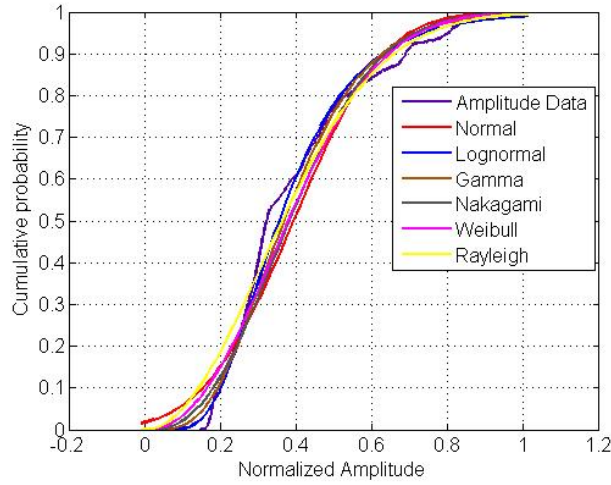
where  $x$  is the envelope amplitude of received signal,  $\mu$  is the mean of distribution, and  $\sigma$  is the standard deviation of the Log-normal distribution. The Lognormal distribution suggests that the decibel value of the averaged received signal strength forms a Gaussian distribution function. And it is used to model large-scale variations in the received signal strength in indoor and urban radio channels. The cumulative distribution function of the Lognormal distribution is given by

$$F(x; \mu, \sigma) = \frac{1}{2} + \frac{1}{2} \operatorname{erf} \left[ \frac{\ln x - \mu}{\sqrt{2\sigma^2}} \right] \quad (17)$$

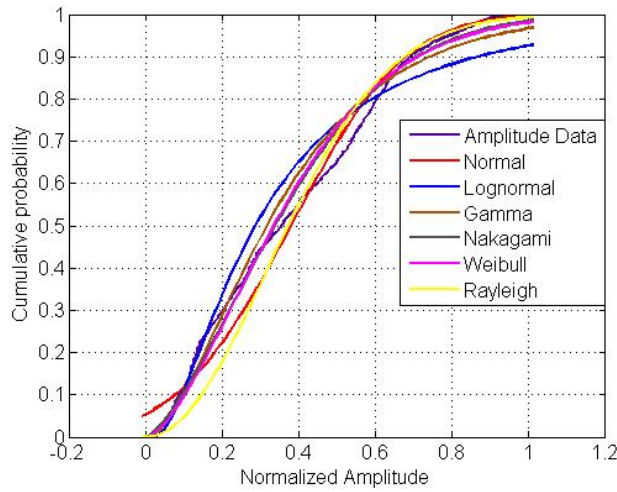
The amplitude is normalized to the maximum amplitude value. Therefore, the CDF of the amplitude is distributed between 0 and 1. In order to compare the goodness of statistical distribution fittings, we obtain the negative log likelihood ratio between the CDF of measurements and theoretical Cumulative Density Function (CDF) for the Normal, Gamma, Rayleigh, Weibull, Nakagami-m and Lognormal distributions.

Figure 10 shows a comparison of CDF fittings for scenario set S1 = {{2.25 GHz}, {Stand, Walk, Jog}, {Left Ankle}, {Right Hip}} in the shielded room. In this scenario, Weibull distribution has the maximum log likelihood ratio for jogging movement. Therefore, we consider Weibull distribution as the best fit for this scenario.

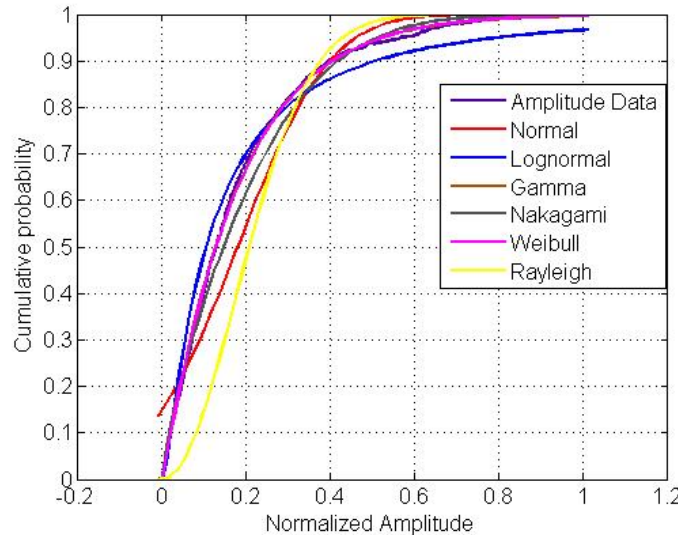
Table 10 shows the negative log likelihood of these six common probability distribution of Normal distribution, Lognormal distribution, Gamma distribution, Nakagami-m distribution, Weibull distribution and Rayleigh distribution at 2.25 GHz. For scenario set S1, the best fitting for the standing motion is Lognormal; the best fitting for walking motion is Nakagami-m; the best fitting for jogging motion is Weibull.



(a) Standing Still



(b) Walking on a Spot



(c) Jogging on a Spot

Figure 10: Cumulative Distribution Function Fittings for the transmission link from left ankle to right hip of at 2.25 GHz for standing, walking and jogging movements

Table 10 gives parameters for these CDF distributions fitted to the envelope of the normalized received signal strength for scenario set S via the negative log likelihood. For a total number of 36 measurements of scenario set S, there are sixteen scenarios fitted into Weibull distribution. Based on a case by case analysis, Lognormal and Weibull distributions fit better for standing motion. There are five cases falls into Weibull distribution and five cases falls into Lognormal distribution for standing motion. Nakagami-m and Weibull distribution are good candidates for a statistical model for

walking motion. Nakagami-m distribution fits better in five cases and four cases of walking motion fall into Weibull distribution for the walking motion. For the jogging motion, Gamma distribution and Weibull distribution are better candidates than other distributions. Weibull distribution fits into seven cases and Gamma distribution fits into three cases for jogging motion.

Table 10: Cumulative Distribution Fittings for 400 MHz, 2.25 GHz and 4.5 GHz

(a) 400 MHz Single Tone Waveform

Antenna Placement	Body motions	Normal $\mu, \sigma$ $-NlogL$	Lognormal $\mu, \sigma$ $-NlogL$	Gamma $a, b$ $-NlogL$	Nakagami $m, w$ $-NlogL$	Weibull $k, \gamma$ $-NlogL$	Rayleigh $\sigma$ $-NlogL$
Back	Stand	0.636573, 0.144726, -822.8594	-0.477734, 0.229544, -849.2287	19.3383, 0.0329177, -849.9565	5.03769, 0.426158, -843.8681	0.694838, 4.81837, -804.039	0.461605, -109.3731
	Walk	0.428414, 0.224625, -119.5161	-1.00302, 0.591497, -175.1843	3.37604, 0.126898, -229.3472	1.0384, 0.233963, -229.0731	0.485014, 2.02561, -228.5637	0.342026, -228.3528
	Jog	0.121489, 0.139656, -879.9153	-2.67664, 1.18377, -1742.9	1.01338, 0.119884, -1772.8	0.341163, 0.0342512, -1640.5	0.119944, 0.973471, -1773.7	0.130865, -624.8668
Left Wrist	Stand	0.832109, 0.0617265, -2186.3	-0.186605, 0.075503, -2162.5	177.91, 0.00467712, -2171.8	45.1691, 0.696213, -2179.7	0.860112, 15.0824, -2173.6	0.590006, 210.1733
	Walk	0.41316, 0.187291, -410.3487	-1.00413, 0.534026, -340.4986	4.3191, 0.0956588, -445.2157	1.31206, 0.205757, -465.9071	0.466293, 2.33446, -462.1922	0.320747, -432.1229
	Jog	0.203037, 0.166555, -598.0871	-1.87996, 0.767347, -1161.8	1.90046, 0.106836, -1113.3	0.573095, 0.0689471, -988.5387	0.223401, 1.35492, -1067.6	0.185671, -780.1574
Left Ankle	Stand	0.94656, 0.0273019, -3491.5	-0.055345, 0.0292815, -3468.0	1179.15, 0.000802745, -3476.1	297.918, 0.896722, - 3483.8	0.958668, 45.0471, -3634.2	0.669598, 405.1001
	Walk	0.723654, 0.141764, -855.9421	-0.346473, 0.226276, -662.1582	21.875, 0.0330813, -740.1438	6.13568, 0.54376, -801.0025	0.778982, 6.38018, -932.2769	0.521421, 70.5249
	Jog	0.428698, 0.205363, -262.9594	-1.00876, 0.641208, -55.2559	3.24823, 0.131979, -204.6061	1.07959, 0.225929, -277.9967	0.482953, 2.19345, -284.8665	0.336102, -275.0730
Right Ankle	Stand	0.933472, 0.0193967, -4038.4	-0.069058, 0.0206413, -4049.4	2338.48, 0.000399178, -4045.9	582.194, 0.871747, - 4042.2	0.943505, 43.0327, -3778.9	0.660207, 381.8467
	Walk	0.360055, 0.190198, -385.7000	-1.19924, 0.655239, -325.3910	2.96927, 0.121261, -429.9747	0.963884, 0.165792, -466.1916	0.406143, 1.97577, -465.6716	0.287917, -465.4818
	Jog	0.410615, 0.227965, -95.9017	-1.10995, 0.767333, 70.1500	2.42795, 0.16912, -106.5844	0.833529, 0.22054, -170.4008	0.460569, 1.82722, -162.0036	0.332069, -151.8007

(b) 2.25 GHz Single Tone Waveform

Antenna Placement	Body motions	Normal $\mu, \sigma$ $-N\log L$	Lognormal $\mu, \sigma$ $-N\log L$	Gamma $a, b$ $-N\log L$	Nakagami $m, w$ $-N\log L$	Weibull $k, \gamma$ $-N\log L$	Rayleigh $\sigma$ $-N\log L$
Back	Stand	0.848754, 0.0853918, -1667.0	-0.168982, 0.0997091, -1689.4	100.244, 0.00846692, -1683.5	25.0942, 0.72767, -1676.6	0.888379, 10.6457, -1592.3	0.603188, 252.6847
	Walk	0.307738, 0.185117, -429.0301	-1.36394, 0.647798, -607.1834	2.85216, 0.107897, -657.6934	0.864643, 0.128949, -615.7388	0.347116, 1.76548, -627.8468	0.253918, -604.0734
	Jog	0.179898, 0.175728, -512.3035	-2.22381, 1.1653, -1043.5	1.12067, 0.160527, -1151.0	0.391516, 0.0632244, -1086.9	0.184141, 1.05922, -1.1490	0.177798, -368.6381
Left Wrist	Stand	0.853051, 0.0940221, -1513.0	-0.167059, 0.14525, -1084.4	61.7193, 0.0138215, -1290.7	17.8244, 0.736531, -1395.5	0.891058, 12.3197, -1665.9	0.606849, 268.9720
	Walk	0.146352, 0.144022, -830.6574	-2.33855, 0.999904, -1472.0	1.34179, 0.109072, -1514.0	0.430522, 0.0421484, -1386.1	0.15412, 1.14423, -1499.5	0.14517, -833.8468
	Jog	0.186266, 0.164855, -614.5048	-2.15846, 1.17303, -928.3860	1.18519, 0.157161, -1102.7	0.424852, 0.061855, -1081.9	0.19404, 1.11876, -1104.5	0.175862, -508.2449
Left Ankle	Stand	0.391669, 0.186979, -413.0112	-1.04092, 0.449024, -676.7629	4.98752, 0.0785298, -627.4034	1.35498, 0.188344, -556.4250	0.444424, 2.24365, -532.9719	0.306875, -514.7312
	Walk	0.37733, 0.23539, -44.6139	-1.25688, 0.868224, 32.7104	1.92146, 0.196377, -126.6559	0.679568, 0.197752, -183.4908	0.419002, 1.57945, -164.3367	0.314446, -91.2185
	Jog	0.178401, 0.171834, -548.1643	-2.26543, 1.23818, -1013.1	1.05856, 0.168531, -1159.6	0.381245, 0.0613354, -1120.8	0.181076, 1.0376, -1159.7	0.175122, -350.5834
Right Ankle	Stand	0.697915, 0.121321, -1105.1	-0.374115, 0.168483, -1178.3	34.7506, 0.0200835, -1159.2	8.68605, 0.501795, -1136.0	0.750417, 5.89734, -1017.0	0.500897, -13.7527
	Walk	0.284339, 0.235298, -45.2422	-1.87991, 1.49374, -96.0009	0.935004, 0.304105, -414.5410	0.376304, 0.136179, -487.8587	0.285607, 1.01241, -412.3126	0.26094, 308.7650
	Jog	0.165055, 0.164322, -619.6824	-2.33319, 1.16673, -1216.6	1.07644, 0.153335, -1285.1	0.37893, 0.0542281, -1221.7	0.167154, 1.03035, -1283.5	0.164663, -439.2278

(c) 4.5 GHz Single Tone Waveform

Antenna Placement	Body motions	Normal $\mu, \sigma$ $-NlogL$	Lognormal $\mu, \sigma$ $-NlogL$	Gamma $a, b$ $-NlogL$	Nakagami $m, w$ $-NlogL$	Weibull $k, \gamma$ $-NlogL$	Rayleigh $\sigma$ $-NlogL$
Back	Stand	0.529034, 0.209094, -234.1549	-0.724592, 0.436223, -216.9086	5.85053, 0.090425, -256.7787	1.70605, 0.32357, -272.2925	0.596087, 2.7848, -274.7080	0.402225, -155.0313
	Walk	0.200734, 0.180513, -469.3206	-2.09074, 1.1883, -799.3509	1.16952, 0.171639, -981.0411	0.418209, 0.0728588, -954.4584	0.208544, 1.10936, -982.6837	0.190865, -354.6198
	Jog	0.12086, 0.127319, -1027.9	-2.78863, 1.4097, -1642.6	0.86922, 0.139044, -1791.8	0.324592, 0.0308072, -1756.8	0.116142, 0.917615, -1790.9	0.124111, -615.2336
Left Wrist	Stand	0.757367, 0.162755, -635.0115	-0.302991, 0.228911, -574.0634	20.0987, 0.0376823, -601.7434	5.40857, 0.600077, -624.7135	0.822574, 5.64788, -681.8244	0.547758, 158.6344
	Walk	0.201123, 0.179388, -479.3230	-2.14254, 1.2882, -753.0662	1.06388, 0.189047, -968.0662	0.396405, 0.0726105, -972.0807	0.20592, 1.06559, -971.0679	0.190539, -277.2080
	Jog	0.138789, 0.131317, -978.4212	-2.51726, 1.23158, -1424.5	1.05726, 0.131272, -1561.2	0.384194, 0.0364958, -1533.2	0.140953, 1.0394, -1561.6	0.135085, -778.3166
Left Ankle	Stand	0.324589, 0.206222, -256.2854	-1.32304, 0.642722, -554.3361	2.68218, 0.121017, -537.3220	0.807001, 0.147859, -476.7527	0.366036, 1.68645, -494.9540	0.2719, -450.5633
	Walk	0.180957, 0.160111, -661.2210	-2.22175, 1.22276, -963.2178	1.11316, 0.162561, -1140.8	0.409151, 0.0583648, -1137.5	0.186674, 1.08801, -1143.9	0.170829, -499.9038
	Jog	0.152835, 0.149056, -775.6965	-2.42544, 1.26882, -1229.9	1.04931, 0.145653, -1406.6	0.377009, 0.0455621, -1363.0	0.154845, 1.03283, -1406.8	0.150934, -570.2239
Right Ankle	Stand	0.697892, 0.140455, -870.7818	-0.382181, 0.218571, -774.7176	22.3974, 0.0311594, -816.4416	6.06767, 0.506768, -848.7342	0.754165, 5.89407, -906.3981	0.503373, 14.9323
	Walk	0.211446, 0.161349, -648.8990	-1.9174, 1.02224, -762.8482	1.52028, 0.139084, -961.6184	0.530728, 0.0707265, -959.9136	0.229124, 1.3148, -971.8924	0.188051, -679.4876
	Jog	0.173576, 0.155015, -712.9709	-2.27774, 1.24595, -1022.7	1.08583, 0.159855, -1205.2	0.401207, 0.0541433, -1203.1	0.178091, 1.07067, -1207.5	0.164535, -530.4517

After comparison of negative log-likelihood of these possible distributions, a fitted distribution is selected for each scenario in Table 11 below.

Table 11: Fitted Statistical Distribution for Each Scenario

(a) 400 MHz Single Tone

Fitting	Stand	Walk	Jog
Back	Gamma	Gamma	Weibull
Left Wrist	Normal	Nakagami	Lognormal
Left Ankle	Weibull	Weibull	Weibull
Right Ankle	Lognormal	Nakagami	Nakagami

(b) 2.25 GHz Single Tone

Fitting	Stand	Walk	Jog
Back	Lognormal	Gamma	Gamma
Left Wrist	Weibull	Gamma	Weibull
Left Ankle	Lognormal	Nakagami	Weibull
Right Ankle	Lognormal	Nakagami	Gamma

(c) 4.5 GHz Single Tone

Fitting	Stand	Walk	Jog
Back	Weibull	Weibull	Gamma
Left Wrist	Weibull	Nakagami	Weibull
Left Ankle	Lognormal	Weibull	Weibull
Right Ankle	Weibull	Weibull	Weibull

### 3.4 Second Order Statistical Characterization

In BANs, different human body motions, antenna positions and center frequencies will result in shadow fading. And the received signal strength fluctuates extensively according to the characteristics of these channels. Given a certain threshold, the performance of the receiver is deteriorated due to the deep fading of channel, which will also give rise to a higher error rate. The statistics of level crossing (fade) rate and fade duration are the other two important parameters for designing medical sensors in BANs. Figure 11 describes the basic concept and parameters related to the level crossing rate and fading duration.

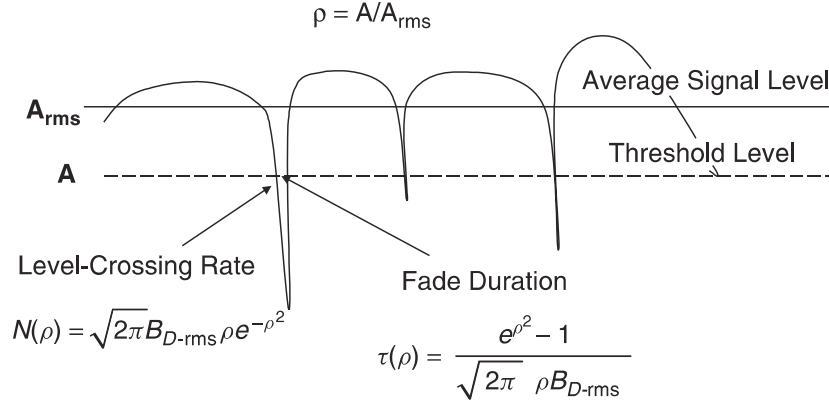


Figure 11: Second Order Statistics: Level-Crossing Rate and Fade Duration

### 3.4.1 Level Crossing Rate

The level crossing rate is defined as the average number of downward crossings of a certain threshold  $T$  per second. For a Rayleigh fading envelope distribution, the level crossing rate is defined as  $N(\rho)$  per second by

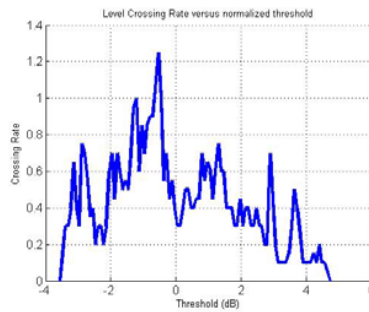
$$N(\rho) = \sqrt{2\pi B_D} \rho e^{-\rho^2} \quad (18)$$

Where  $\rho = A/A_{rms}$  is the ratio of the threshold level to the RMS amplitude of the fading envelope and  $f_M = 0.5B_D$  is the maximum Doppler spread of the signal.

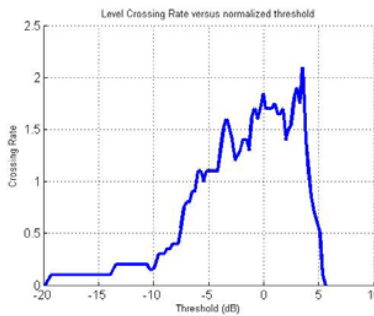
For different human body motions, we could not derive a fixed equation for the level crossing rate, since the envelope distributions are not determined. But we could obtain the normalized level crossing rate  $N(\rho)$  versus normalized threshold  $\rho$  in decibel for scenario set S1, where  $N(\rho)$  is normalized to the RMS value of the number of downward crossings and  $\rho$  is normalized to the RMS value of the envelope of the signal, as shown in fig.12. For low values of normalized threshold  $\rho$  below -4 dB of the standing motion, we rarely have a fade crossing this threshold. As the normalized threshold  $\rho$  increases, the number of fades crossing the threshold also increases until  $\rho$  is zeros, which means that the actual threshold reaches the RMS value of the envelope of the signal. After the threshold, the number of downward crossings decreases when the threshold is increased. Up to a point, there is no fading below the threshold any more.

For the three human motions defined in S1, the jogging motion had the greatest variation of channel fading with a peak value of 7.25 Hz. Communication links for walking has a

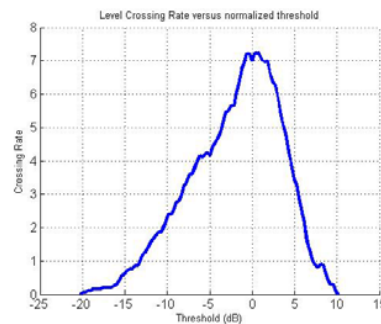
less crossing rate where the maximum level crossing rate is 2.10 Hz, since it is not as intense as jogging and the channel suffers from less shadow fading across the normalized threshold  $\rho$ . As a result of relatively stable motion, the level crossing rate is the smallest for standing, where the peak value is 1.25 Hz. Only a small number of fade crossings happen for a certain normalized threshold  $\rho$ . There is a potential relationship between the level crossing rate and Doppler spread caused by human body motions.



(a) Level Crossing Rate for Standing Motion



(b) Level Crossing Rate for Walking Motion



(c) Level Crossing Rate for Jogging Motion

Figure 12: Level Crossing Rate for Scenario Set S1

The summarized level crossing rate could be found in table 12 for all the possible

scenarios described in the measurement setup. The peak value of level crossing rate keeps increasing for standing, walking and jogging motions.

Table 12: Level Crossing Rate

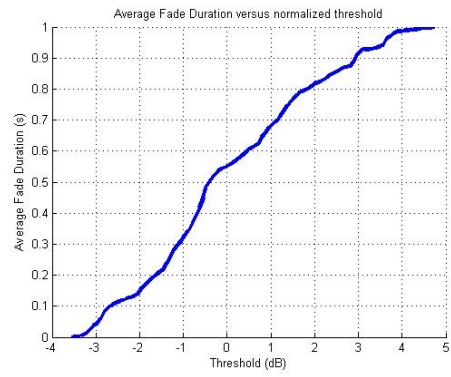
Antenna Position	Motion	Maximum Level Crossing Rate for 400MHz	Maximum Level Crossing Rate for 2.25 GHz	Maximum Level Crossing Rate for 4.5 GHz
Back	Stand	1.1000	0.7000	1.2500
	Walk	2.0000	3.5000	5.6000
	Jog	5.4500	7.2000	8.6000
Left Wrist	Stand	2.0000	2.1000	1.7500
	Walk	2.5000	3.2000	4.3000
	Jog	4.4500	6.1500	10.5000
Left Ankle	Stand	1.9000	1.2500	1.9000
	Walk	1.8000	2.1000	4.4000
	Jog	3.4000	7.2500	10.8000
Right Ankle	Stand	3.0500	1.4500	3.1000
	Walk	1.5000	1.9000	5.2500
	Jog	2.1500	7.6500	10.8500

### 3.4.2 Average Fade Duration

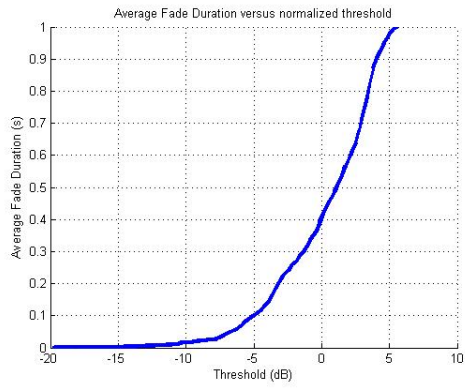
The average fade duration, also referred to as outage duration, is calculated as the average time duration when fading is below a certain threshold. The average fade duration  $\tau(\rho)$  for Rayleigh fading is defined as

$$\tau(\rho) = \frac{e^{\rho^2} - 1}{\sqrt{2\pi}\rho B_D} \quad (19)$$

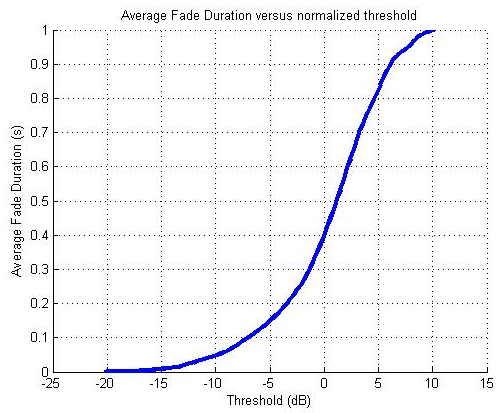
Where  $\rho$  is the given threshold. Figure 13 explicitly gives the average fade duration versus normalized threshold  $\rho$  for scenario set S1, which shows that the standing motion has the fastest increasing speed compared with walking and jogging motions. For the total measurement duration of 20 s, the averaged fade duration time is a non-decreasing function of the normalized threshold. For a lower value of  $\rho_0$ , there is almost no fading duration below the normalized threshold. As the normalized threshold increases, the fade duration keeps on rising until it reaches to the measurement time duration (20 s) as the normalized threshold arrives at its peak amplitude.



(a) Fade Duration for Standing



(b) Fade Duration for Walking



(c) Fade Duration for Jogging

Figure 13: Fade Duration for Scenario Set S1

### 3.4.3 Outage Probability

For a given threshold, the outage probability is computed as the probability distribution of fading when the signal power drops below this threshold. It is a measure of the quality of transmission in a mobile radio channel. If the average number of downward crossings for a normalized level is denoted as  $N(\rho)$  and the average fade duration is  $\tau(\rho)$ , then the outage probability is calculated as

$$\mathbf{Prob}(\alpha < \rho) = \tau(\rho) \times N(\rho) \quad (20)$$

And the percentage of time that the system can send information is given as

$$\mathbf{S} = \mathbf{1} - \mathbf{Prob}\{\alpha < \rho\} = \mathbf{1} - \tau(\rho) \times N(\rho) \quad (21)$$

IEEE 802.15.6 standard <sup>[62]</sup> has proposed that the latency requirement is 125 ms for medical applications and 250 ms for non-medical applications. In order to satisfy these requirements, a higher normalized threshold, coming from Path Loss model is claimed to maintain the throughput of the unstable channel in packet communications.

### 3.5 Doppler Spread Spectrum

It is well known from the analysis of electromagnetic signals that if there is a relative motion between the source and the receiver, an apparent change will occur in frequency between the source of a wave and the receiver of the wave. If either the source or the receiver moves towards the other, the receiver will perceive a higher frequency. This is because the receiver will receive a greater number of electromagnetic waves per second and interpret the greater number of waves as a higher frequency. Conversely, if the source and the receiver are moving apart, the receiver will receive a smaller number of electromagnetic waves per second and will perceive a lower frequency. In both cases, the frequency produced by the source will remain constant. The maximum Doppler frequency shift is determined by the velocity of the movement  $v_m$  and the length of propagation wave  $\lambda = \frac{c}{f_c}$  by

$$\pm f_m = \frac{v_m}{\lambda} \quad (22)$$

where  $c$  is the propagation velocity and  $f_c$  is the transmitting frequency. When the

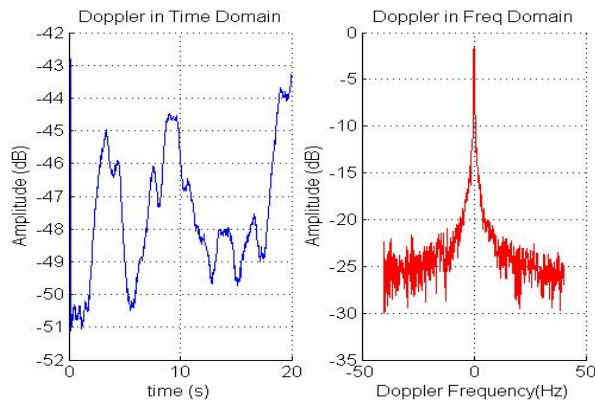
transmitter is moving toward the receiver, the Doppler frequency shift  $f_m$  would be positive. On the other hand,  $f_m$  would be negative if transmitter moves away from the receiver. Hence, the maximum value of  $f_m$  could be approximate from Doppler spread BD of the on-body to on-body communication.

From the narrowband measurement results, we have the time domain response  $H(f_c; t)$  received from an unmodulated sine wave transmitted at 400 MHz, 2.25 GHz and 4.5 GHz respectively. By design, each measurement is a sample of an ergodic process and stationary. All the following analysis below assumes that the channel is wide-sense stationary at a minimum <sup>[70]</sup>.

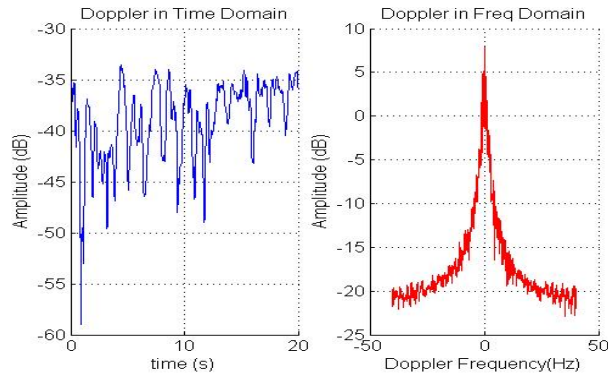
Applied a threshold of -10 dBm in the frequency domain, Doppler spread  $D(\lambda)$  could be derived from the Fourier transform of the time domain data  $H(f_c; t)$ , where

$$D(\lambda) = \int_{-\infty}^{+\infty} H(f_c; t) e^{-j2\pi\lambda t} dt \quad (23)$$

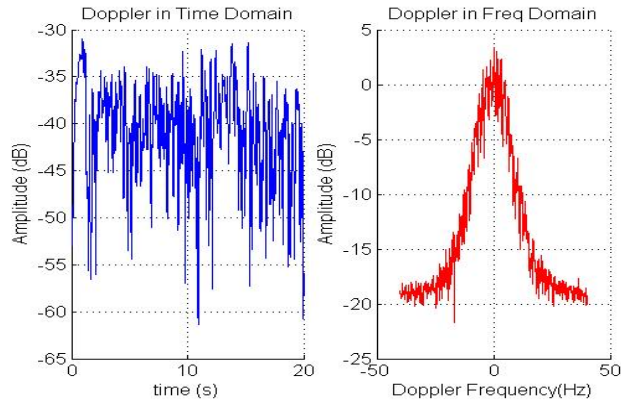
A set of Doppler spreads for a specific scenario S1 = {{2.25 GHz}, {Stand, Walk, Jog}}, {Left Ankle}, {Right Hip}} is shown in fsig.14, including both time domain response  $H(f_c; t)$  and corresponding response  $D(\lambda)$  in frequency domain. The Doppler spreads for standing, walking and jogging motions are approximately 0.5507 Hz, 4.0843 Hz and 10.8344 Hz for the communication link between left ankle and right hip at 2.25 GHz.



(a) Stand Still



(b) Walk on the Spot



(c) Jog on a Spot

Figure 14: Time Domain and Frequency Domain Analysis of Scenario Set S1

For the on-body to on-body communication, Doppler spread varies approximately from 0.5 to 11 Hz for scenario set S1. Table 13 lists Doppler spreads for each scenario defined in Sect.2.6.2. The conclusion drawn from table 13 is that the Doppler spread increases approximately from 0.1 to 12 Hz for different antenna placement, different center frequency and three human body movements. And as the transmission range which is related to positions of TX antenna, Doppler spreads also rises in a small range when the distance between RX and TX increases. Table 14 lists a comparison of Doppler spread for Scenario Set S2, where  $S2 = \{\{400 \text{ MHz}, 2.25 \text{ GHz}, 4.5 \text{ GHz}\}, \{\text{Walk}\}, \{\text{Left Ankle}\}, \{\text{Right Hip}\}\}$ . For the transmission link from left ankle to right hip of walking motion, the Doppler spread increases in a small range. But for all the scenarios, the Doppler spread is not proportionally related to the center frequency.

Table 13: Doppler Spread for All the Scenarios at 400 MHz, 2.25 GHz, 4.5 GHz

(a) Doppler Analysis for 400 MHz

Antenna Position	Motion	Doppler (Hz)	RMS Doppler (Hz)	Coherence Time (ms)
Back	Stand	0.4255	0.5802	209.8786
	Walk	0.8594	1.0300	135.4084
	Jog	2.5682	1.7671	71.4551
Left Wrist	Stand	0.2753	0.4949	350.1076
	Walk	2.9620	1.6181	109.1818
	Jog	7.1952	2.5509	74.2856
Left Ankle	Stand	0.1752	0.4532	688.4473
	Walk	2.4906	1.4476	188.9173
	Jog	7.1214	2.4516	47.2303
Right Ankle	Stand	0.1001	0.4956	291.9244
	Walk	2.2236	1.5050	150.6865
	Jog	6.4080	2.5150	39.1484

(b) Doppler Analysis for 2.25 GHz

Antenna Position	Motion	Doppler (Hz)	RMS Doppler (Hz)	Coherence Time (ms)
Back	Stand	0.6383	0.7758	724.0871
	Walk	5.2516	2.2093	123.2081
	Jog	8.5041	2.7276	47.3489
Left Wrist	Stand	0.5006	0.6975	234.4692
	Walk	4.7885	2.0608	104.6887
	Jog	12.0006	3.1149	40.6528
Left Ankle	Stand	0.5507	0.7696	377.2509
	Walk	3.5419	1.8789	124.6821
	Jog	10.8344	3.0082	28.8768
Right Ankle	Stand	1.3392	0.9833	1050.60
	Walk	4.7997	2.0063	128.9503
	Jog	11.5501	3.1837	38.4998

(c) Doppler Analysis for 4.5 GHz

Antenna Position	Motion	Doppler (Hz)	RMS Doppler (Hz)	Coherence Time (ms)
Back	Stand	0.4756	0.5856	474.8717
	Walk	3.3000	1.6951	50.2929
	Jog	5.3948	2.2459	26.2686
Left Wrist	Stand	0.7259	0.8366	475.5905
	Walk	3.7213	1.7641	72.9752
	Jog	7.4471	2.6017	18.0017

Left Ankle	Stand	0.4255	0.6349	357.8102
	Walk	4.0843	1.6861	90.0661
	Jog	6.5477	2.6133	16.6652
Right Ankle	Stand	0.3755	0.5616	390.0243
	Walk	3.8277	1.7594	89.3603
	Jog	7.3216	2.8870	13.9869

Table 14: Comparison of Doppler Spread for Scenario Set S2

Transmitter Placement	Frequency	Doppler Spread (Hz)	RMS Doppler Bandwidth (Hz)
Left Ankle	400 MHz	2.4906	1.4476
	2.25 GHz	3.5419	1.8789
	4.5 GHz	4.0843	1.6861

### 3.6 RMS Doppler Spread

A more specific estimation of Doppler spread is the RMS Doppler bandwidth <sup>[70]</sup> defined by

$$f_N = \left[ \frac{\int \lambda^2 V(\lambda) d\lambda}{\int V(\lambda) d\lambda} \right]^{1/2} \quad (24)$$

where  $V(\lambda)$  is the Fourier transform of the complex auto-correlation function of  $H(f_c; t)$ . RMS Doppler bandwidth is proposed to describe Doppler shift by calculating the weighted signal power rather than a simply overall width of the spectrum in a more scientific method.

For the scenario set S, the RMS Doppler bandwidth changes in a range of 0.4–4 Hz, where difference comes from various human body motions, center waveform frequency, and antenna positions on the test subject. In table 13, for the standing still motion, RMS Doppler bandwidth is always below one, which shows a concentrated distribution of signal power. While for walking and jogging motions, RMS Doppler bandwidth is much larger than that of standing still, since signal power is dispersedly distributed in the frequency domain. Doppler spread spectrums in fig.14 have shown an example of power distribution in frequency domain, where the Doppler Spread increases from (a) to (b) to (c). For a scenario set S2, table 15 illustrated that RMS Doppler spread bandwidth increases in a small range for the communication link from left ankle to right hip at different center frequency. But the RMS Doppler spread does proportionally relate to the

transmission center frequency.

### 3.7 Shape of Doppler Spread Spectrum

In the on-body to on-body channel, the transmitter and receiver could be either stationary or mobile. The relative mobility will lead to different Doppler shapes in frequency domain, where the “Bell-Shaped” Doppler spectrum are relative to center frequency and human body motions. In this study, we obtained maximum likelihood estimates of received signal strength in dB with respect to frequency variations of three curves, which is used to characterize and model channels in past researches.

- Laplacian

$$F(f) = \frac{a}{b+cf^2} + d \quad (25)$$

where  $f$  is the sampling frequency.

- Gaussian

$$F(f) = \sum_{i=0}^{n-1} a_i \exp(-(f_0 - f_i)^2 / c_i^2) \quad (26)$$

this is an  $n$ th order Gaussian model, where  $f$  is the sampling frequency. We use the 4-th order Gaussian curve as a candidate for the shape of Doppler spread spectrum.

- Polynomial

$$F(f) = \sum_{i=0}^{n-1} p_i f^i \quad (27)$$

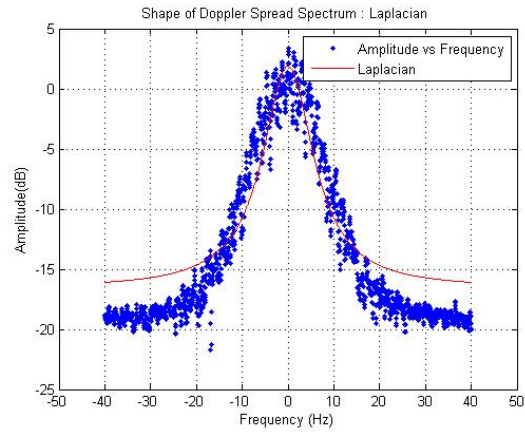
This is an  $n$ th order Polynomial model, where  $f$  is the sampling frequency. We use the 4-th order Polynomial curve as a candidate for the shape of Doppler spread spectrum.

In order to compare goodness of the three curve fittings, we consider root mean square error (RMSE) between the proposed curves and actual measured data. Given total deviation of measured values with the fit to the measured values, we come to the estimation of standard deviation of random component in measured data, and is defined as

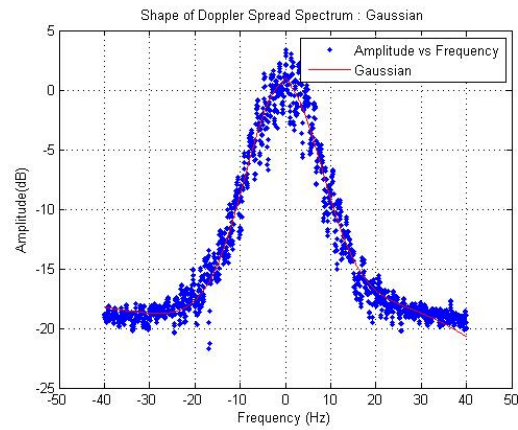
$$RMSE = \sqrt{MSE(\hat{\theta})} = \sqrt{E((\hat{\theta} - \theta)^2)} \quad (28)$$

Where  $\hat{\theta}$  is an estimator with respect to the measured data  $\theta$  leading to the least RMSE values.

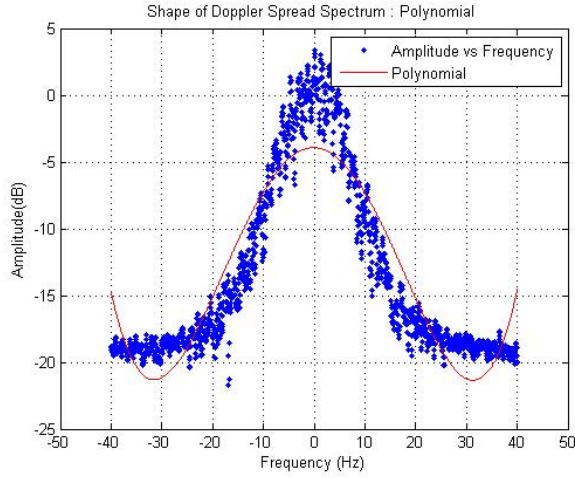
Figure 15 shows a sample of shape fittings for scenario S3 = {{2.25 GHz}, {Jog}, {Left Ankle}, {Right Ankle}}. The 4th order Gaussian estimator has the minimum RMSE 1.2503, which shows a better performance than the Laplacian or Polynomial estimator.



(a) Laplacian Fitting



(b) 4-th order Gaussian Fitting



(c) 4-th order Polynomial Fitting

Figure 15: Shape of Doppler Spread Spectrum for Scenario Set S2

For all the considered scenarios, the estimated shape is shown in table 15 below.

Table 15: Estimate Doppler Spread Shape for Scenario Set S

(a) Center frequency at 400 MHz

Transmitter Placement	Movement	Gaussian (RMSE)	Polynomial (RMSE)	Laplacian (RMSE)	Best Fit
Back	Stand	1.5556	2.7620	2.5246	Gaussian
	Walk	1.5573	2.9677	3.4680	Gaussian
	Jog	1.5623	2.7473	4.9783	Gaussian
Left Wrist	Stand	1.5577	3.1874	2.5327	Gaussian
	Walk	1.2879	3.3299	4.3967	Gaussian
	Jog	1.5426	2.7538	3.9092	Gaussian
Left Ankle	Stand	1.8447	2.6659	2.0905	Gaussian
	Walk	1.3382	3.0904	4.2168	Gaussian
	Jog	2.5206	3.2646	2.2528	Laplacian
Right Ankle	Stand	1.4869	2.3832	1.7931	Gaussian
	Walk	1.9683	3.3608	4.6428	Gaussian
	Jog	1.5118	2.8692	4.9422	Gaussian

(b) Center frequency at 2.25 GHz

Transmitter Placement	Movement	Gaussian	Polynomial	Laplacian	Best Fit
Back	Stand	1.6717	2.8621	2.7583	Gaussian
	Walk	1.3376	2.9252	3.0400	Gaussian
	Jog	1.4709	2.7434	3.0424	Gaussian
Left Wrist	Stand	1.0378	1.7610	2.1399	Gaussian
	Walk	1.3275	4.0592	6.0163	Gaussian
	Jog	15.9193	2.6757	7.1874	Polynomial
Left Ankle	Stand	1.5800	2.6943	1.4931	Laplacian
	Walk	1.0414	3.2636	1.0877	Gaussian
	Jog	1.2503	2.7156	2.7462	Gaussian
Right Ankle	Stand	0.9967	2.4638	2.9908	Gaussian
	Walk	1.3204	4.0858	1.4053	Gaussian
	Jog	1.6557	2.7096	5.1726	Gaussian

(c) Center frequency at 4.5 GHz

Transmitter Placement	Movement	Gaussian	Polynomial	Laplacian	Best Fit
Back	Stand	1.5198	2.7898	2.2770	Gaussian
	Walk	1.3888	2.9584	1.3737	Laplacian
	Jog	1.5267	1.8955	2.6266	Gaussian
Left Wrist	Stand	1.4376	2.5096	1.4731	Gaussian
	Walk	1.3592	3.6857	1.3874	Gaussian
	Jog	1.4725	1.5991	3.8102	Gaussian
Left Ankle	Stand	1.5807	2.9347	2.1678	Gaussian
	Walk	1.4257	3.4260	5.5908	Gaussian
	Jog	1.4472	1.6969	2.9549	Gaussian
Right Ankle	Stand	1.4753	2.7258	1.5158	Gaussian
	Walk	1.6347	3.5181	6.1423	Gaussian
	Jog	1.5364	1.6077	4.7368	Gaussian

Comparing the RMSE for the Laplacian, Gaussian and Polynomial estimators, the 4th order Gaussian function is a good candidate for the shape of the Doppler spread spectrum of different human body movements. But it does not always perform better than Laplacian and Polynomial estimators for several cases.

### 3.8 Coherence Time

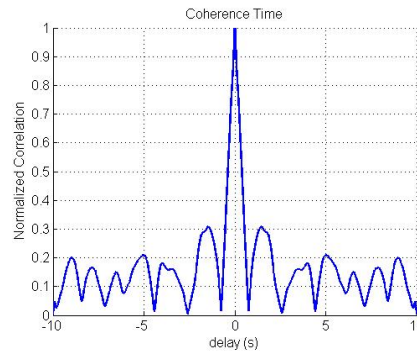
Coherence time is the description of time dispersive nature of the channel in time domain, equivalent to Doppler spread in frequency domain. It is actually a statistical measurement of the time duration over which the channel impulse response is essentially invariant. In other words, coherence time is the time duration over which two received signal has a strong amplitude correlation. In a baseband transmission, a distortion will occur when bandwidth of the signal is greater than the inverse of coherence time. Coherence time and Doppler spread are inversely proportional to each other.

$$f_m = \frac{c}{T_c} \quad (29)$$

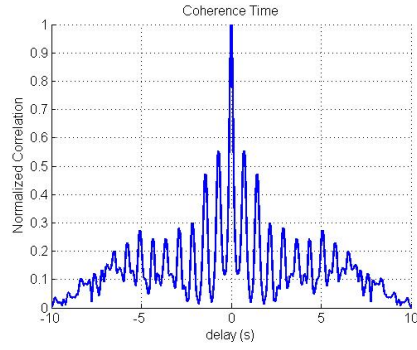
where  $c$  is a constant value. Channel coherence time is typically defined as the time duration over which the normalized auto correlation coefficients of time domain data is above 0.5, defined by

$$\rho(m) = \frac{\sum_{n=1}^{N-|m|} \{x(n+m) - m_x\} \{x^*(n) - m_x\}}{|r(n+m)| \times |r(n)|} \quad (30)$$

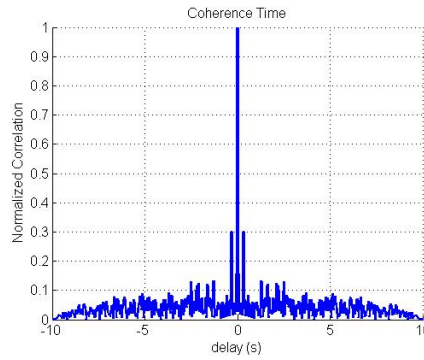
where  $m_x$  is the mean value with  $\frac{1}{N} \sum_{n=1}^N x(i)$  and  $|r(n)| = \sum_{n=1}^N \{x(n) - m_x\}^2$ . The correlation function for scenario S1 is shown in fig.16 below.



(a) Coherence Time for Standing Motion



(b) Coherence Time for Walking Motion



(c) Coherence Time for Jogging Motion

Figure 16: Coherence Time for Scenario Set S1

Hence, the coherence time  $T_c$  is  $377.2509\text{ ms}$  for standing,  $124.6821\text{ ms}$  for walking and  $28.8768\text{ ms}$  for jogging, which means that a maximum symbol transmission rate  $\frac{1}{T_c}$  of  $2.65\text{ Hz}$  for standing,  $8.02\text{ Hz}$  for walking and  $34.63\text{ Hz}$  for jogging is required to avoid distortion from frequency dispersion for the communication link from left ankle to right hip at  $2.25\text{ GHz}$  in digital communication system. Table 13 shows the summary of coherence for all the possible communication links at MICS, ISM and UWB bands. As the intensity of human body movements increases, the coherence time will decrease sharply, since the channel suffers from greater fading and invariant in a shorter duration. The coherence time is usually below  $90\text{ ms}$  for jogging motion, around  $100\text{ ms}$  for walking motion and more than  $200\text{ ms}$  for standing motion.

## 4 Activity Classification with Inertial Sensors

### 4.1 Sensors on Smartphones

During the past several decades, tremendous development of the microelectronics has enabled sensors and mobile devices with unprecedented characteristics. These small, high computation and low cost sensors interact with people in a sensor pervasive environment. Smartphones with built-in sensors could continuously monitor location, motion and various environmental conditions. These mechanical sensors would provide relatively accurate data. The location sensors report the physical location of the device, including orientation sensors and magnetometers. The motion sensors monitor device movements, e.g. acceleration, forces and gravity. The environmental sensors measure various environmental parameters, such as pressure, illumination and humidity.

In this thesis, we use four Samsung Exhibit II as the device to collect data and model the human body motion offline. This Samsung Exhibit II has an Android operating system with a 2.3.3 API level. There are more than seven build-in sensors: GP2A Proximity Sensor, AK8975 Magnetic Field Sensor, AK8975 Orientation sensor, BMA222 Acceleration Sensor, GP2A Light Sensor, etc. In order to differentiate human body motions standing, walking and jogging, we use the mean and variance of the linear accelerometer, orientation and gravity as the features to the neural networks along with Received Signal Strength features discussed in chap.3. Figure 17 shows the coordinate system (relative to a device) that is used as the description of sensor's coordinate system.

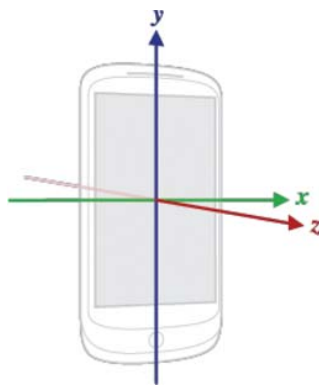


Figure 17: Coordinate System that is used by the Android Smartphones

We extracted features from the accelerometer and orientation sensor in Samsung Exhibit II. The accelerometer sensor measures the acceleration force in  $m/s^2$  along x axis, y axis

and z axis, including the gravity of the earth. The orientation sensor is highly related to the physical of the device, which could monitor the degrees of rotation relative to the three physical axes.

## 4.2 Behavior of Sensors

### 4.2.1 Data Collection

In order to understand the performance of built-in sensors on the smartphone, we placed the smartphone on the desktop to analyze the stability of accelerometer and orientation sensors. The accelerometer provides the acceleration along each device axis, including gravity. The linear acceleration is calculated by the following relationship

$$\mathbf{linear\ acceleration} = \mathbf{acceleration} - \mathbf{acceleration\ due\ to\ gravity} \quad (31)$$

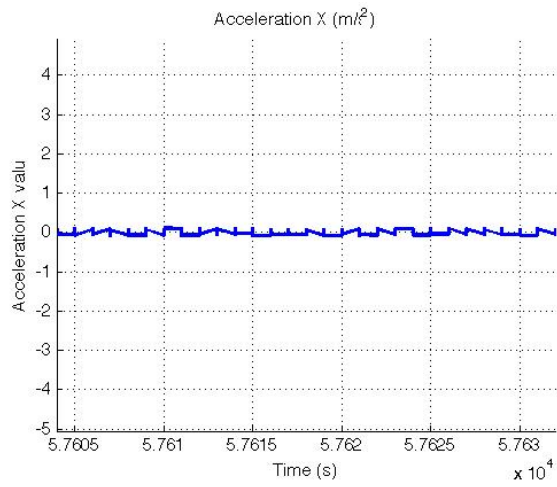
We use a sliding window with a size of 2048 samples. The time domain data of accelerometer sensor and orientation sensor for three axes are shown in fig.18 and fig.19 respectively. And the statistical results are shown in table 16 for accelerometer sensor and table 17 for orientation sensor.

Table 16: Stability of Accelerometer Sensor

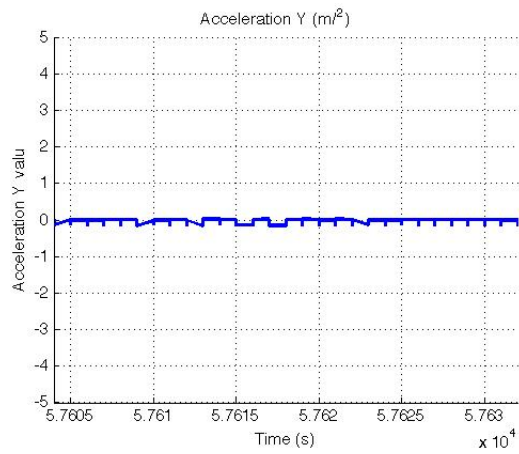
Coordination	X	Y	Z
Mean	5.2437e-04	-3.2102e-04	8.5280e-04
Variance	0.0057	0.0012	0.0056

Table 17: Stability of Orientation Sensor

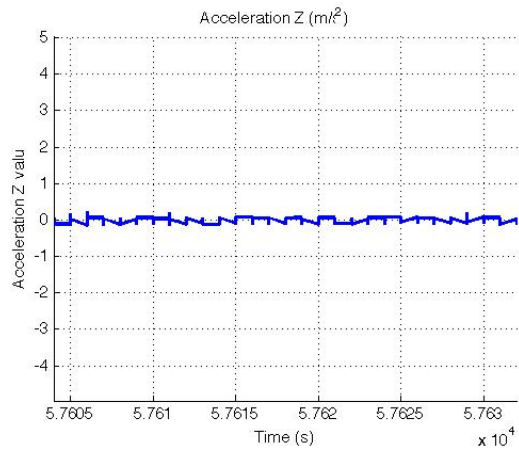
Coordination	X	Y	Z
Mean	16.0985	0.9146	1.2102
Variance	0.0778	0.0409	0.1869



(a) Acceleration x axis

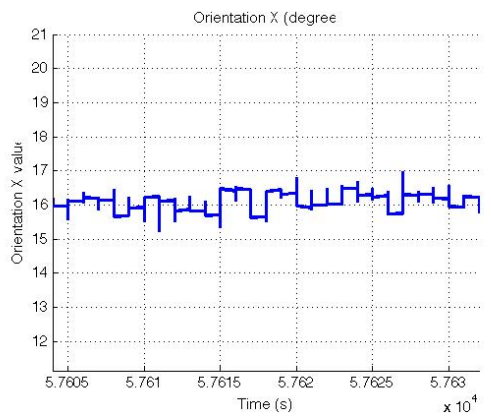


(b) Acceleration y axis

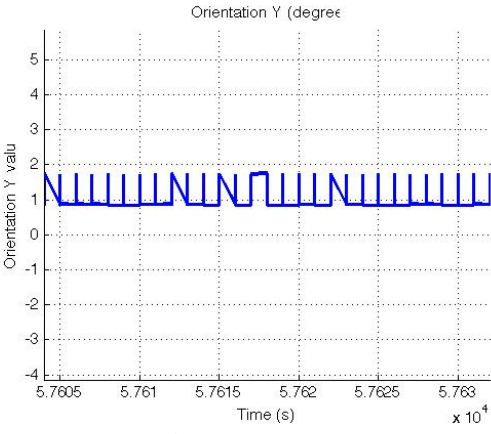


(c) Acceleration z axis

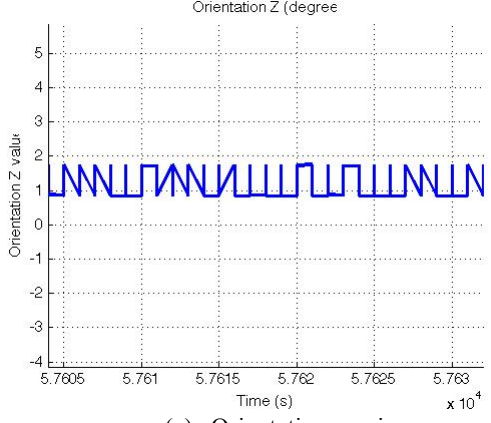
Figure 18: Time Domain data of accelerometer sensor



(a) Orientation x axis



(b) Orientation y axis



(c) Orientation z axis

Figure 19: Time Domain data of orientation sensor

Instability of these mechanical sensors introduces bias into measurement, and is required to be eliminated from measurement of human body movements.

Similar as the measurement setup discussed in chapter 2, four Android phones are attached to back, left wrist, left ankle and right ankle on the surface of human body,

which is the same placement as RF sensors. Real Time data of three different human body movements (standing, walking and jogging) are collected in a three-minute interval. The first 10 samples and the last 10 samples are discarded to reduce the error. Ten sets of data are collected, processed and evaluated for activity classification.

#### 4.2.2 Mean and Variance

Based on the collected data, statistical analysis of accelerometer and orientation sensors are discussed in this part. Mean and variance of different human body motions are important features to distinguish between three possible motions. The DC component is the mean acceleration and orientation values of the signal over the sampling window. The variance of acceleration and orientation values is reflective of the intensity of body movements.

#### 4.2.3 Energy

The energy<sup>[67]</sup> feature is defined as the sum of the discrete Fast Fourier Transformation (FFT) component magnitudes of the signal, normalized by the number of samples. Additionally, the DC component of the signal is excluded in the calculation. The energy feature is defined as

$$E = \frac{\sum_{i=1}^n |FFT(x_i)|}{n} \quad (31)$$

where  $n$  is the number of samples and  $x_i$  is the  $i$ th signal amplitude.

#### 4.2.4 Frequency-domain entropy

The frequency-domain entropy<sup>[67]</sup> measures the information of the uncertainty associated with each sample in the data stream. It represents the expected value of information contained in the discrete FFT component of the reported signal. The frequency-domain entropy is calculated as the entropy of the normalized signal strength.

$$H(X) = \sum_{i=1}^n P(x_i) I(x_i) = \sum_{i=1}^n P(x_i) * \log \frac{1}{P(x_i)} \quad (32)$$

where  $P(x_i) = \frac{|FFT(x_i)|}{\sum_{i=1}^n |FFT(x_i)|}$ . And the DC component should also be excluded from this calculation.

### 4.3 Activity Classification

The human body activity classification has tremendous application in medical, entertainment, security, etc. For instance, patients with obesity or diabetes are often required to follow an amount of regular exercises as part of their treatment; patients with heart attack diseases need to be remotely monitored in case of accident. These could be achieved by differentiating and tracking a variety of human body movement. The recognition of human activities could be approached with the assistance of wearable sensors, including RF and inertial sensors. Extracted features are mostly related to the user's movements (e.g. accelerometers), environmental variables (e.g. temperature) or physiological signals (e.g. ECG). With body mounted accelerometers, human body activities could be classified [74, 75]. As the emerging of smart devices, a variety of activity recognition applications are evolved for smartphones [76-80]. Accurately classify activities would also enhance the indoor geolocation [81].

#### 4.3.1 Activity Recognition Architecture and Methods

Activity classification problem could be solved with machine learning algorithms, which requires training stage and evaluation stage. The training stage generates an activity recognition model from the attributes extracted from the measured time series datasets. The evaluation stage is to test unknown datasets with the prior trained learning model. The architecture for the activity classification is shown in fig.20 below.

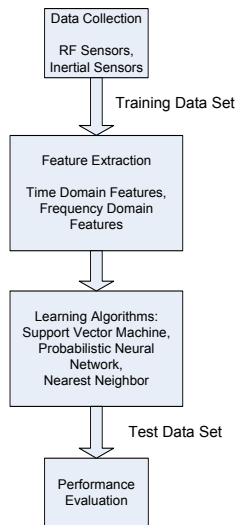


Figure 20: Activity Classification Architecture

In order to achieve high classification accuracy, several issues need to be carefully considered in the algorithm design.

- 1) Target activity types. There are a lot of activity types required to classify with each other: ambulation activities (e.g. walking, jogging, climbing stairs, descending stairs), transportation movements (e.g. Riding a bus, cycling, driving), daily activities (e.g. eating, drinking, working, watching, reading, washing), etc. The complexity and intensity of a variety of activities would introduce different pattern recognition problem. Moreover, the overlapped activities would bring more difficulty into the activity classification problem. In the following discussion, we assume each body activity is separated from others.
- 2) Feature selection. With wearable RF and inertial sensors, signal strength attributes, motion attributes, location, environmental attributes could be measured and processed for the learning algorithms. Features in the processed dataset should be carefully extracted to reduce redundancy and irrelevancy that might negatively affect the recognition accuracy.
- 3) Learning algorithms. In order to discover classification pattern, machine learning algorithms are developed and evaluated to describe, analyze and predict data. The learning algorithms are divided into three categories: supervised learning, unsupervised learning and semi-supervised learning. The supervised learning algorithms include Decision Tree classifier, Bayesian Networks, Neural Network, Support Vector Machines, Fuzzy Logic method, Regression methods, Hidden Markov models, working with labeled data. The unsupervised learning method deals with unlabeled data. But unsupervised learning might be hard to be used to differentiate activities. Semi-supervised learning algorithm is developed by allowing part of the data to be unlabeled.

A variety of activity classification systems has been researched, developed and evaluated in the past several decades. Maurer presented “eWatch”<sup>[82]</sup> recognition system that embeds accelerometer, light sensor, thermometer and microphone sensor inside. A C4.5 Decision Tree is applied to the time domain features to achieve an accuracy up to 92.5% for six ambulation activities. “Cosar” framework<sup>[83]</sup> for activity recognition is proposed by Daniele Riboni where real-time data are collected

with two accelerometers and GPS sensor under the Android platform. Statistical and ontological reasoning are applied to achieve an overall accuracy around 93%. “ActiServ”<sup>[76]</sup> made use of a fuzzy inference system to classify ambulation with built-in accelerometer in mobile phones. Yet it would sacrifice long runtime duration with a top accuracy level. A Hidden Markov Model (HMM)<sup>[84]</sup> to recognize the body activity is derived to predict activity, based on the measured angular velocity and 3D deviation of the acceleration signals.

#### 4.3.2 Feature Extraction

The variance, energy and entropy of time domain data extracted from the accelerometer and orientation sensor are analyzed to provide as features for activity classification. Moreover, the path loss range, variance of path loss, the maximum level crossing rate, Doppler spread, RMS Doppler spread and coherence time are also applied to classify three human body motions.

#### 4.3.3 Backpropagation Network

Backpropagation was created by generalizing the Widrow-Hoff learning rule to multiple-layer networks and nonlinear differentiable transfer functions. The scale conjugate gradient algorithm<sup>[68]</sup> is applied to the train data set to generate a function approximate to learn the behavior of backpropagation network. This algorithm, designed to avoid line search, is a combination of the conjugate gradient approach and model-trust region approach.

The propagation network architecture is shown in the fig.21 below. The training data set goes into Input. Weight and bias are iteratively adjusted to minimize the mean square error for feedforward networks - the average squared error between the network outputs and the target outputs.

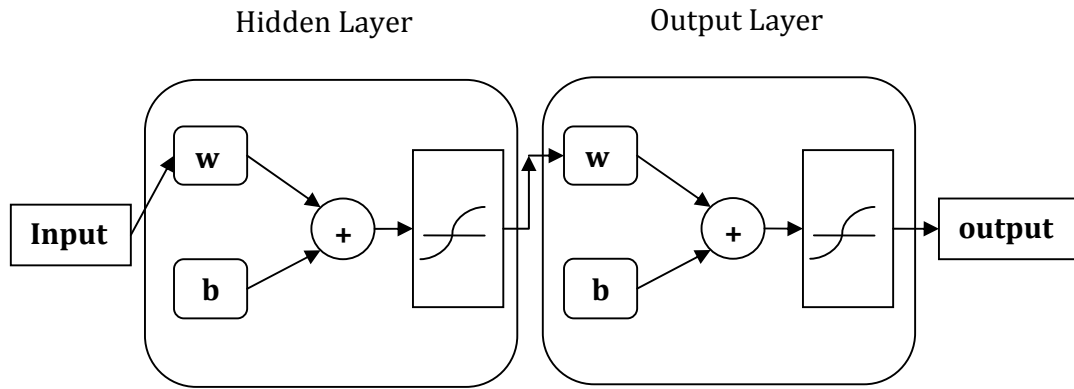


Figure 21: Propagation Network Architecture

The comparison of backpropagation algorithm on different data sets is shown in table 18 below, where the RF sensors can detect human body motions with an accuracy of 96.67%, more accurate than assisted with accelerometer and orientation sensor.

Table 18: Comparison of Different Machine Learning Algorithms

Sensors	BP	PNN	kNN	SVM
Inertial	75%	83.3%	91.7%	83.3%
RF	96.67%	75%	83.3%	96.67%
Inertial & RF	96.67%	83.3%	91.7%	91.7%

The performance of validation is shown in fig.22 below.

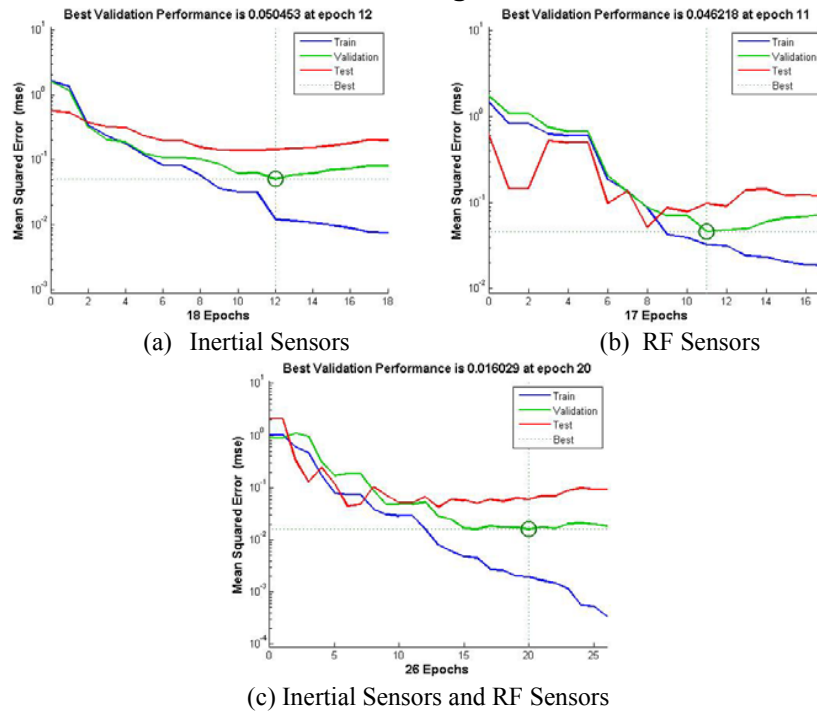


Figure 22: Performance Validation

#### 4.3.4 Probabilistic Neural Network (PNN)

Artificial Intelligence has gained great prominence in the area of pattern recognition. Probabilistic Neural Network (PNN) [85, 86] was first proposed by Donald F. Specht in 1988 could be used for the human body activity classification problem. Fig.23 shows the neural network architecture for classification of input patterns  $X$  into two categories. The input unit does not perform any computation functionalities. It simply feeds input data to the pattern units. In the pattern units, the exponentiation activation function is used to replace the commonly used sigmoid activation function for back-propagation

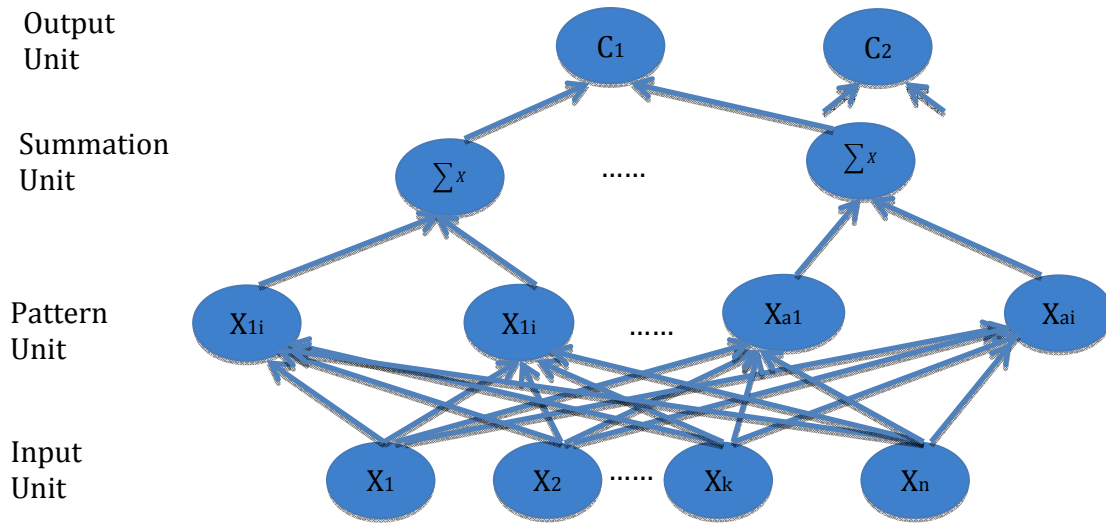


Figure 23: Neural Network Architecture for Classification

Each pattern neuron forms a product of the input vector  $x_k$ :

$$\varphi_{ai} = \frac{1}{(2\pi d)^{d/2}} \exp \left[ -\frac{(x-x_{ai})^T(x-x_{ai})}{2\sigma^2} \right] \quad (33)$$

Where  $x_{ai}$  is the  $i$ th training vector from category  $a$ ,  $d$  is the dimension of the input feature vector,  $\sigma$  is the smooth factor. Smooth factors would have different effects on the estimated PDF. The summation unit would accumulate and average the inputs from the pattern units which correspond to the same activity class.

$$f_a = \frac{1}{m} \sum_{i=1}^m \varphi_{ai} \quad (34)$$

Where  $m$  denotes the number of training vectors in category  $a$ . Assuming an equal priori probability for each category, the classification of each pattern vector is made according to the Bayes' Rule:

$$c(x) = \mathit{argmax}\{f_a(x)\} \quad a = 1, 2, \dots, n \quad (35)$$

The output units represent the results of activity classification.

For the three target human body motions, the PNN algorithm assisted with RF sensors and inertial sensors provides an accuracy of 83.3%. Potentially, the detection accuracy of PNN algorithm would increase if more distinguished features are provided, since this algorithm essentially calculates the relevance between the target data set and the training data set by the kernel function.

#### 4.3.5 $k$ -Nearest Neighbor ( $k$ -NN)

The  $k$ -nearest neighbor algorithm is a lazy learning approach to solve activity classification problem based on the closed training sets in the feature space. The  $k$ -nearest neighbor algorithm is among the simplest of all machine learning algorithms: an object is assigned to the class most common among its  $k$  nearest neighbors. This algorithm finds the estimated class with local optimality. Therefore it would require large storage space and intensive computation to achieve high performance.

Like other learning algorithms, a decision boundary is computed through the training stage where the training sets are vectors in a multidimensional feature space labeled individually. In the classification procedure, an unlabeled vector is classified by assigning the label which is most frequently among  $k$  training sets nearest to the query point, where  $k$  is a user-defined constant.

The training set is defined as:

$$x = \{x_1, x_2, \dots, x_n\}$$

Each  $x_i$  is a vector containing  $a$  features,  $x_i = \{x_{1i}, x_{2i}, \dots, x_{ni}\}$ . The Euclidean distance is used as the distance metric to find the nearest point from training set  $x$  to the unlabeled vector .

$$d(y, x_i) = \sqrt{\sum_{k=1}^a (y_k - x_{ik})^2} \quad (36)$$

The count of each category  $k$  is accumulated as  $c(k)$ . Therefore, the unlabeled vector is classified by solving  $\mathit{argmax}(c(x_i))$  subject to  $\sum_{i=1}^a c(x_i) = k$ .

A 4th order nearest neighbor approach is applied to classify the three human body motions, the accuracy with inertial sensors is 91.7%, higher than that with RF sensors. The reason lies in that only six features are provided by the RF sensors, far less than the

72 features with inertial sensors. More features would provide relatively accurate estimation of Euclidean distance defined in eq.41.

#### 4.3.6 Support Vector Machine (SVM)

Support Vector Machine is commonly used for activity classification problem. In order to obtain an “optimal” boundary (the most distant hyperplane from both sets), a kernel function is used to project data sets to higher dimensional space with the aim of finding a linear decision boundary to partition the data.

The boundary hyperplane is expressed as

$$\mathbf{w}^T \mathbf{x} + \mathbf{b} = 0 \quad (37)$$

where  $w$  is the weight coefficient vector and  $b$  is a bias term. The optimal boundary maximizes the minimum of the distance between the training vector and the boundary and is formalized to a optimization problem as

$$\begin{aligned} & \text{minimize} && \mathbf{w}^T \mathbf{w} \\ & \text{subject to} && \mathbf{y}_i(\mathbf{w}^T \mathbf{x}_i + \mathbf{b}) \geq 1 \end{aligned} \quad (38)$$

where  $y_i = \begin{cases} -1, & \text{if } x_i \text{ belong to one set} \\ 1, & \text{if } x_i \text{ belong to the other set} \end{cases}$

This optimization problem could be achieved by Lagrange’s method of indeterminate coefficients. The Lagrange’s equation is defined as

$$L(\mathbf{w}, \mathbf{b}, \mathbf{a}_i) = \frac{1}{2} \mathbf{w}^T \mathbf{w} - \sum_i \mathbf{a}_i [\mathbf{y}_i(\mathbf{w}^T \mathbf{x}_i + \mathbf{b}) - 1] = -\frac{1}{2} \sum_i \sum_j \mathbf{a}_i \mathbf{a}_j \mathbf{y}_i \mathbf{y}_j \mathbf{x}_i^T \mathbf{x}_j + \sum_i \mathbf{a}_i \quad (39)$$

where  $a_i \geq 0$  is the indeterminate coefficients. Solve this conditional optimization problem with derivative of  $L(w, b, a_i)$ , we could reduce it to a quadratic programming problem which finds  $a_i$  to maximize  $L(w, b, a_i) = -\frac{1}{2} \sum_i \sum_j \mathbf{a}_i \mathbf{a}_j \mathbf{y}_i \mathbf{y}_j \mathbf{x}_i^T \mathbf{x}_j + \sum_i \mathbf{a}_i$ , subject to  $\sum_i \mathbf{a}_i \mathbf{y}_i = 0, \mathbf{a}_i \geq 0$ .

Kernel method is used to find the nonlinear boundary by transformation the vector space to a higher dimensional space, so that a nonlinear separable data could be linearly separable after transformation. Let  $\Phi$  denotes the transformation to higher dimensional space. The kernel function is defined to the distance in transformed space is related to the original distance in the low dimensional spaces.

$$\mathbf{K}(\mathbf{x}, \mathbf{x}') = \Phi(\mathbf{x})^T \Phi(\mathbf{x}') \quad (40)$$

In this thesis, we use the Gaussian kernel function.

$$\mathbf{K}(x, x') = \exp\left(-\frac{\|x-x'\|^2}{\sigma^2}\right) \quad (41)$$

However, unlike previous three approaches, this method can only classify the data set into two categories. We organize the overall data into static motion composed of standing scenario and dynamic motion composed of walking and jogging scenarios. Applied the SVM algorithms, the accuracy can achieve 96.67% with RF characteristics. Yet, an accuracy of 83.3% is obtained with only accelerometer and orientation sensor. Future work needs to classify human body motion into more than two categories with improved algorithms.

## 5 Conclusion and Future Work

### 5.1 Conclusion

This thesis is concerned with the continuous monitoring of human body movements, with a view toward a variety of potential health-care applications. The physical implementations of such monitoring systems will utilize wireless Body Area Networks (BANs), which in turn implies communication links (channels) between sensors and RF elements in each such network. In this thesis, the propagation characteristics of channels are measured, modeled and evaluated with body mounted sensors. The thesis investigated probabilistic models that are derived for wireless communication and human body activity classification. Using a Vector Network Analyzer, three human body motions were measured at MICS band, ISM band and UWB band: standing, walking and jogging. The body mounted sensors were placed at the subject's back, left wrist, left ankle, right ankle and right hip, intended to track the subject's breathing, as well as movements of the hands and feet.

The statistical distribution of received signal strength was investigated with six common distributions: Normal distribution, Gamma distribution, Rayleigh distribution, Weibull distribution, Nakagami-m distribution and Lognormal distribution. Evaluated using the negative log likelihood of the received signal strength, all the measured scenarios were fitted into one of the candidate distributions. The results indicate that the Rayleigh distribution is not suitable for describing any of the three human body movements. Generally, the Weibull distribution is found to be a suitable candidate for all three body motions. But for better accuracy, the Lognormal distribution provides a better fit for standing scenarios in several cases, while the Nakagami-m distribution fits better for walking motion in several cases and the Gamma distribution fits better in a few cases for jogging scenarios.

Level crossing rate and average fading duration are important parameters typically used to describe channel fading characteristics, especially the fluctuation of received signal strength. Doppler spread represents the relative motion between the transmitter and the receiver. For the standing scenario, the Doppler spread is found to be always below 1 Hz.

For the walking scenario, the Doppler spread is greater than that for the standing scenario, specifically, around 3 Hz. The jogging scenario will introduce maximum Doppler spread, which is greater than 6 Hz. The coherence time is also analyzed to describe the time dispersive nature of the channel. It is inversely proportional to the Doppler spread. The coherence time is usually below 90 *ms* for jogging scenarios, around 100 *ms* for walking scenarios and more than 200 *ms* for standing scenarios. Moreover, the shape of the Doppler spectrum is described with a Laplacian model, 4<sup>th</sup> order Gaussian model or Polynomial model. By comparing observed RMSE for each of these candidate models, it is found that most of the Doppler spread shapes could be well described with a 4<sup>th</sup> Gaussian model. However, several cases could also be described with a Laplacian model or a Polynomial model.

The inertial sensors, including accelerometer and orientation sensor inside smart devices, are also used to characterize the three human body motions. Mean, variance, energy and entropy are extracted as features to classify different human body motions. The quantitative characteristics of channel modeling for different human body motions could also be applied to solving the activity classification problem. In the thesis, the back propagation, probabilistic neural network, *k*-Nearest Neighbor and support vector machine algorithm are applied to differentiate human body activities. The detection accuracy can be improved with both RF sensors and inertial sensors.

## 5.2 Future Work

In order to obtain more accurate channel models, more empirical data must be gathered and evaluated. More extensive data collection campaigns would enable more detailed characterization of the BAN channels and the features that can be utilized in machine learning algorithms. Moreover, the future work should also address the design of algorithms for activity classification, including study of a wider range of activity types, such as sitting, falling down, standing up, eating, and drinking.

## 6 Reference

- [1] Ruijun Fu, Yunxing Ye, Ning Yang, K. Pahlavan, "Doppler spread analysis of human motions for BodyArea Network applications", 22nd International Symposium on Personal Indoor and Mobile Radio Communications (PIMRC), pp.2209-2213, 2011.
- [2] Ruijun Fu, Yunxing Ye, Kaveh Pahlavan, "Characteristic and Modeling of Human Body Motions for Body Area Network Applications", International Journal of Wireless Information Networks (IJWIN), Volume 19, Number 3, pp.219-228, 2012.
- [3] Ruijun Fu, Yunxing Ye, Ning Yang, K. Pahlavan, " Heterogeneous Cooperative Localization for Social Networks with Mobile Devices", 23rd International Symposium on Personal Indoor and Mobile Radio Communications (PIMRC), 2012.
- [4] Yi Wang, Ruijun Fu, Yunxing Ye, U. Khan, K. Pahlavan, "Performance bounds for RF positioning of endoscopycamera capsules", Biomedical Wireless Technologies, Networks, and Sensing Systems (BioWireleSS), p.71-74, Jan.2011.
- [5] Yunxing Ye, U. Khan, N. Alsindi, Ruijun Fu, K. Pahlavan, "On the accuracy of RF positioning in multi-Capsuleendoscopy", 22nd International Symposium on Personal Indoor and Mobile Radio Communications (PIMRC), pp. 2173-2177, 2011.
- [6] Kaveh Pahlavan, Yunxing Ye, Umair Khan, Ruijun Fu, "RF localization inside human body: Enabling micro-robotic navigation for medical applications", 2011 International Conference on Localization and GNSS (ICL-GNSS), pp. 133-139, June 2011.
- [7] Kaveh Pahlavan, Yunxing Ye, Ruijun Fu, Umair Khan, "Challenges in Channel Measurement and Modeling for RF Localization Inside the Human Body", International Journal of Embedded and Real-Time Communication Systems (IJERTCS), Volume 3, Issue 3, 2012.
- [8] Shen Li, Jie He, Ruijun Fu, Kaveh Pahlavan, "A Hardware Platform for Performance Evaluation of In - body Sensors," in 6th International Symposium on Medical Information and Communication Technology (ISMICT2012), La Jolla, 2012.
- [9] Xin Zheng, Guanqun Bao, Ruijun Fu, Kaveh Pahlavan, "The performance of Simulated Annealing Algorithms for Wi-Fi Localization using Google Indoor Map," IEEE Vehicular Technology Society, 2012.
- [10] G. Dimakis, V. Prabhakaran, and K. Ramchandran, "Fading results from narrowband measurements of the indoor radio channel. Symposium on Information Processing in Sensor Networks," IPSN, Los Angeles, pp. 111–117, 2005.
- [11] St. Jude Medical Company, <http://www.sjm.com/>.
- [12] GivenImaging Company, "Endoscopy Capsule," <http://www.givenimaging.com/en-us/Innovative-Solutions/Capsule-Endoscopy/Pages/default.aspx>.

- [13] Jason W.P. Ng, Benny P.L. Lo, Oliver Wells, Morris Sloman, Nick Peters, Ara Darzi, Chris Toumazou, and Guang-Zhong Yang, "UbiMon: Ubiquitous Monitoring Environment for Wearable and Implantable Sensors," London Technology Network, Mar 2004.
- [14] CodeBlue: An Ad Hoc Sensor Network Infrastructure for Emergency Medical Care, David Malan, Thaddeus Fulford-Jones, Matt Welsh, Steve Moulton, MobiSys 2004 Workshop on Applications of Mobile Embedded Systems (WAMES 2004), June, 2004.
- [15] Sensor Networks for Emergency Response: Challenges and Opportunities, Konrad Lorincz, David Malan, Thaddeus Fulford-Jones, Alan Nawoj, Antony Clavel, Victor Shnayder, Geoff Mainland, Steve Moulton, Matt Welsh, IEEE Pervasive Computing, Oct/Dec, 2004.
- [16] Konstantas, Dimitri and Halteren van, Aart and Bults, Richard and Wac, Katarzyna and Jones, Val and Widya, Ing and Herzog, Rainer (2004), "MobiHealth: Ambulant Patient Monitoring Over Public Wireless Networks," Mediterranean Conference on Medical and Biological Engineering, MEDICON 2004, 31 July - 5 Aug 2004, Island of Ischia, Naples, Italy.
- [17] D. Cypher, N. Chevrollier, N. Montavont, and N. Golmie, "Prevailing over wires in healthcare environments: benefits and challenges," IEEE Communications Magazine, Vol. 44, No. 4, pp. 56, 2006.
- [18] Kamyay Yekeh Yazdandoost, Kamran Sayrafian-Pour, "15-08-0780-09-0006-tg6-channel-model", April 2009.
- [19] Takahiro Aoyagi, Jun-ichi Takada, Kenichi Takizawa, Norihiko Katayama, Takehiko Kobayashi, Kamyay Yekeh Yazdandoost, Huan-bang Li and Ryuji Kohno, "Channel model for wearable and implantable WBANs," IEEE 802.15-08-0416-01-0006, July 2008.
- [20] Jung-Hwan Hwang, Il-Hyoung Park, and Sung-Weon Kang, "Channel model for human body communication," IEEE 802.15-08-0577-00-0006, August 2008.
- [21] Minseok Kim, Jun-ichi Takada, Bin Zhen, Lawrence Materum, Tomoshige Kan, Yuuki Terao, yohei Konishi, Kenji Nakai, Takahiro Aoyagi, Ryuji Kohno, "Statistical property of dynamic BAN channel gain at 4.5 GHz," IEEE 802.15-08-0489-02-0006, Sept.2008.
- [22] Dino Miniutti, Leif Hanlen, David Smith, Andrew Zhang, Daniel Lewis, David Rodda, Ben Gilbert, "Narrowband channel characterization for body area network," IEEE 802.15-08-0421-00-0006, July 2008.
- [23] R. D. Errico, L. Ouvry, "A statistical model for on-body dynamic channels," International Journal of Wireless Information Networks, Vol. 17, pp. 92–104, 2010.
- [24] Huan-Bang Li, Takizawa K., Bin Zheri, R. Kohno, "Body Area Network and Its Standardization at IEEE 802.15.MBAN," Mobile and Wireless Communications Summit, pp.1-5, 2007.
- [25] Aastha Gupta, Thushara D. Abhayapala, "Body Area Networks: Radio channel modelling and propagation characteristics," Australian Communications Theory Workshop (AusCTW ), 2008.

- [26] Y. Zhao, Y. Hao, A. Alomainy, and C. Parini, "Uwb on-body radio channel modelling using ray theory and sub-band fdtd method," *IEEE Trans. On Microwave Theory and Techniques*, Special Issue on Ultra-Wideband, vol. 54, no. 4, pp. 1827–1835, 2006.
- [27] J. Ryckaert, P.D. Doncker, R. Meys, A.D.L. Hoye, and S. Donnay, "Channel model for wireless communication around human body," *Electronic Letters*, vol. 40, no. 9, 2004.
- [28] J.A. Ruiz, J. Xu, and S. Shiamamoto, "Propagation characteristics of intra-body communications for body area networks," *3rd IEEE Conf. on Consumer Communications and Networking*, Vol. 1, pp. 509–503, 2006.
- [29] T. Zasowski, G. Meyer, F. Althaus, and A. Wittneben, "Propagation effects in uwb body area networks," *IEEE International Conference on UWB*, pp. 16–21, 2005.
- [30] S. L. Cotton and W. G. Scanlon, "A statistical analysis of indoor multipath fading for a narrowband wireless body area network," in *17th IEEE Intl. Symp. Personal, Indoor & Mobile Radio Comms. (PIMRC)*, pp. 1–5, Helsinki, Finland, Sept. 2006.
- [31] S. L. Cotton and W. G. Scanlon, "Characterization and modeling of the indoor radio channel at 868 MHz for a mobile body worn wireless personal area network," *IEEE Antennas Wireless Propagation Letter*, Vol. 6, pp. 51–55, 2007.
- [32] I. Z. Kovacs, G. F. Pedersen, P. C. F. Eggers, and K. Olesen, "Ultra wideband radio propagation in body area network scenarios," in *Proc. ISSSTA, 2004*, pp. 102–106.
- [33] Elisabeth Reusens, Wout Joseph, Benoit Latre, Bart Braem, Gunter Vermeeren, Emmeric Tanghe, Luc Martens, Ingrid Moerman and Chris Blondia, "Characterization of On-Body Communication Channel and Energy Efficient Topology Design for Wireless Body Area Networks," *IEEE Transactions on Information Technology in Biomedicine*, Nov.2009.
- [34] Andrew Fort, Claude Desset, Philippe D, "An ultra-wideband body area propagation channel Model-from statistics to implementation," *IEEE Transactions on Microwave Theory and Techniques*, Vol. 54, Issue: 4, pp. 1820 – 1826, June 2006.
- [35] Fort, C. Desset, P. De Doncker, P. Wambacq, and L. Van Biesen, "An ultra-wideband body area propagation channel modelfrom statistics to implementation," *IEEE Transactions on Antennas and Propagation*, Vol. 54, No. 4, pp. 1820, 2006.
- [36] J. Kim and Y. Rhamat-Samii, "Implanted antennas inside a human body: Simulations, designs and characterizations," *IEEE Transactions on Microwave Theory and Technoques*, Vol. 52, no. 8, pp. 1934—1943, Aug. 2004.
- [37] N. F. Timmons, W. G. Scanlon, "An adaptive energy efficient MAC protocol for the medical body area network," *Wireless Communication, Vehicular Technology, Information Theory and Aerospace & Electronic Systems Technology*, pp. 587-593, May 2009.
- [38] Gengfa Fang, E. Dutkiewicz, "BodyMAC: Energy efficient TDMA-based MAC protocol for Wireless Body Area Networks," *ISCIT 2009. 9th International Symposium on Communications and Information Technology*, pp. 1455-1459, Sept.2009.

- [39] Shyamal Patel, Konrad Lorincz, Richard Hughes, Nancy Huggins, John Growden, David Standaert, Metin Akay, Jennifer Dy, Matt Welsh, Paolo Bonato, "Monitoring Motor Fluctuations in Patients With Parkinson's Disease Using Wearable Sensors," *IEEE Transactions on Information Technology in Biomedicine*, November, Volume 13, Number 6, 2009.
- [40] Raúl Chávez-Santiago, Ali Khaleghi, Ilangko Balasingham and Tor A. Ramstad, "Architecture of an Ultra Wideband Wireless Body Area Network for Medical Applications," 2nd International Symposium on Applied Sciences in Biomedical and Communication Technologies, Nov.2009.
- [41] E. Lubrin, E. Lawrence, and K.F. Navarro, "Wireless remote healthcare monitoring with motes," *Proc. Intl. Conf. on Mobile Business*, pp. 235-241, July 2005.
- [42] N. Herscovici, C. Christodoulou, E. Kyriacou, M. S. Pattichis, C. S. Pattichis, A. Panayides, and A. Pitsillides, "m-health e-emergency systems: current status and future directions," *IEEE Antennas Propagat. Mag.*, Vol. 49, pp. 216–231, Feb. 2007.
- [43] R. Shmidt et al., "Body area network, a key infrastructure element for patient-centered medical applications," *Biomed. Tech. (Berl)*, Vol. 47, pp. 365–368, 2002.
- [44] D. Smith, D. Miniutti, L. Hanlen, A. Zhang, D. Rodda, B. Gilbert, "Dynamic channel measurements around 400MHz for Body Area Networks," *IEEE 802.15-09-0186-00-0006*, Mar. 2009.
- [45] S. L. Cotton, and W. G. Scanlon, "Characterization and modeling of the indoor radio channel at 868 MHz for a mobile body-worn wireless personal area network," *IEEE Antennas and Wireless Propagation Letters*, Vol. 6, pp. 51–55, 2007.
- [46] S. L. Cotton, and W. G. Scanlon, "Characterization and modeling of on-body spatial diversity within indoor environments at 868 MHz," *IEEE Transactions on Wireless Communications*, Vol. 8, No. 1, pp. 14–18, 2009.
- [47] S. L. Cotton, G. A. Conway, and W. G. Scanlon, "A time-domain approach to the analysis and modeling of on-body propagation characteristics using synchronized measurements at 2.45 GHz," *IEEE Transactions on Antennas and Propagation*, Vol. 57, No. 4, pp. 943, 2009.
- [48] H. Yang, A. Alomainy, Z. Yan, C. G. Parini, Y. Nechayev, P.Hall, and C. C. Constantinou, "Statistical and deterministic modeling of radio propagation channels in WBAN at 2.45 GHz," *Proceedings of IEEE Antennas and Propagation Society International Symposium*, Baltimore, pp. 2169, 2006.
- [49] Simon L. Cotton and William G. Scanlon, "An experimental investigation into the influence of user state and environment on fading characteristics in wireless body area networks at 2.45 GHz," *IEEE Transactions on Wireless Communications*, Vol. 8, Issue: 1, pp: 6 – 12, Feb. 2009.
- [50] K. I. Ziri-Castro, W. G. Scanlon, and N. E. Evans, "Measured pedestrian movement and bodyworn terminal effects for the indoor channel at 5.2 GHz," *Europ. Trans. Telecommun.*, Vol. 14, pp. 529–538, Jan. 2004.

- [51] M. Kim, J. Takada, "Statistical Model of 4.5 GHz Narrowband On-Body Propagation Channel with Specific Actions," *IEEE Antennas Wireless Propag. Lett.*, Vol. 8, pp. 1250–1254, 2009.
- [52] B. Zhen, M. Kim, J. Takada, R. Kohno, "Characterization and Modeling of Dynamic On-body Propagation at 4.5 GHz," *IEEE Antennas Wireless Propag. Lett.*, Vol. 8, pp. 1263–1267, 2009.
- [53] N. Katayama, K. Takizawa, T. Aoyagi, J.-I. Takada, Li Huan-Bang, R. Kohno, "Channel model on various frequency bands for wearable body area network," *International symposium on Applied Sciences on Biomedical and Communication Technologies*, Aalborg, pp. 1–5, 2008.
- [54] Z. Jian, D. B. Smith, L. W. Hanlen, D. Miniutti, D. Rodda, B. Gilbert, "Stability of narrowband dynamic body area channel," *IET Microwaves, Antennas and Propagation*, Vol. 8, pp. 53–56, 2009.
- [55] L. Lingfeng, P. De Doncker, and C. Oestges, "Fading correlation measurement and modeling on the front side of a human body," *European Conference on Antennas and Propagation (EuCAP)*, Berlin, pp. 969, 2009.
- [56] K. Sayrafian-Pour, W. -B. Yang, J. Hagedorn, J. Terrill, and K.Y. Yazdandoost, "A statistical path loss model for medical implant communication channels," *Proceedings of IEEE Personal, Indoor and Mobile Radio Communications*, Tokyo, pp. 2995–2999, 2009.
- [57] D. Smith, L. Hanlen, D. Miniutti, J. Zhang, D. Rodda, and B. Gilbert, "Statistical characterization of the dynamic narrowband body area channel," *Applied Sciences on Biomedical and Communication Technologies*, pp. 1–5, 2008.
- [58] D. Smith, L. Hanlen, J. Zhang, D. Miniutti, D. Rodda, and B. Gilbert, "Characterization of the dynamic narrowband on-body to off-body area channel," *Proceedings of IEEE International Conference on Communications (ICC '09)*, Dresden, pp. 14–18, 2009.
- [59] D. Smith, D. Miniutti, L. Hanlen, D. Rodda and B. Gilbert, "Dynamic narrowband body area communications: link-margin based performance analysis and second-order temporal statistics," *Proceedings of the IEEE Conference on Wireless Communications and Networking*, Sydney, pp. 14–18, 2010.
- [60] D. B. Smith, J. Zhang, L. W. Hanlen, D. Miniutti, D. Rodda, and B. Gilbert, "Temporal correlation of the dynamic on-body area radio channel," *Electronics Letters*, vol. 45, pp. 1212, 2009.
- [61] B. Zhen, M. Kim, J. Takada, and R. Kohno, "Characterization and modeling of dynamic on-body propagation," *ICST Conference on Pervasive Computing Technologies for Healthcare*, London, pp.1, 2009.
- [62] B. Zhen, M. Patel, S. Lee, and E. Won, "Body area network (BAN) technical requirements, 15-08-0037-01-0006-ieee-802-15-6-technical-requirements-document-v-4-0".
- [63] L. Liu, F. Keshmiri, C. Craeye, P. D. Doncker, and C. Oestges, "An analytical modeling of polarized time-variant on-body propagation channels with dynamic body scattering," *EURASIP J. Wireless Commun. Network.*, vol. 2011, no. Article ID 362521, pp. 1–12, 2011.

- [64] R. D'Errico and L. Ouvry, "Time-variant BAN channel characterization," in Proc. IEEE 20th Int. Symp. on Personal, Indoor and Mobile Radio Communications, pp. 3000–3004, Sep. 2009.
- [65] M. Kim, J.-I. Takada, "Characterization of Wireless On-Body Channel Under Specific Action Scenarios at Sub-GHz Bands," IEEE Transactions on Antennas and Propagation, Vol. 60, Issue: 11, pp: 5364 - 5372, 2012.
- [66] M. Kim, J.-I. Takada, "Characterization of Wireless On-Body Channel Under Specific Action Scenarios at Sub-GHz Bands," IEEE Transactions on Antennas and Propagation, Vol. 60, Issue: 11, pp: 5364 - 5372, 2012.
- [67] L. Bao and S. Intelle, "Activity recognition from user-annotated acceleration data," Proc. 2<sup>nd</sup> Int. Conference Pervasive Computing, pp. 1 – 17, 2004.
- [68] Moller, M. F., "A scaled conjugate gradient algorithm for fast supervised learning," Neural Networks, vol. 6, pp. 525-533, 1993.
- [69] R. Ganesh, and K. Pahlavan, "Statistical modelling and computer simulation of indoor radio channel, IEEE Proceedings Communications," Vol. 138, No. 3, pp. 153, 2002.
- [70] S.J. Howard, and K. Pahlavan, "Fading results from narrowband measurements of the indoor radio channel. Proceedings of Personal," Indoor and Mobile Radio Communications, London, pp. 92, 1991.
- [71] Dino Miniutti, Leif Hanlen, David Smith, Andrew Zhang, Daniel Lewis, David Rodda, Ben Gilbert, "Narrowband channel characterization for body area network," IEEE 802.15-08-0421-00-0006, July 2008.
- [72] K. Pahlavan and A. H. Levesque, Wireless information networks, Wiley-Inter science, Sept.2005.
- [73] N. Youssef, T. Munakata, and M. Takeda, "Fade statistics in Nakagami fading environments," in Proc. IEEE 4th Intl. Symp. Spread Spectrum Tech. & Appl., Vol. 3, pp. 1244–1247, 1996.
- [74] Andrea Manniniemail and Angelo Maria Sabatini, "Machine learning methods for classifying human physical activity from on-body accelerometer," appears on Sensors, pp. 1154-1175, 2010.
- [75] S. Patel, C. Mancinelli, J. Healey, M. Moy, and P. Bonato, "Using wearable sensors to monitor physical activities of patients with copd: A comparison of classifier performance," 2009 Body Sensor Networks, pp. 234-239, 2009.
- [76] M. Berchtold, M. Budde, D. Gordon, H.R. Schmidtke, M. Beigl, "ActiServ: activity recognition service for mobile phones," 2010 International Symposium on Wearable Computers (ISWC), pp.1-8, 2010.
- [77] O. D. Lara, M.A. Labrador, "A mobile platform for real-time human activity recognition," IEEE Consumer Communications and Networking Conference (CCNC), Page(s): 667 – 671, 2012.
- [78] J. R. Kwapisz, G. M. Weiss, and S. A. Moore, "Activity recognition using cell phone accelerometers," presented at the Proceedings of the Fourth International Workshop on Knowledge Discovery from Sensor Data, pp. 10-18, 2010.

- [79] E. Miluzzo, Hong Lu, D. Peebles, T. Choudhury, A.T. Campbell, "A survey of mobile phone sensing," *IEEE Communications Magazine*, Vol. 48, Issue: 9, Page(s): 140 – 150, Sept. 2010.
- [80] Jennifer R. Kwapisz, Gary M. Weiss, Samuel A. Moore, "Activity recognition using cell phone accelerometer," *ACM SIGKDD Explorations Newsletter archive*, Vol. 12 Issue 2, Pages 74-82, December 2010.
- [81] Zuolei Sun, Xuchu Mao, Weifeng Tian and Xiangfen Zhang, "Activity classification and dead reckoning for pedestrian navigation with wearable sensors," *Measurement Science and Technology*, Vol.20, Issue 1, Jan.2009.
- [82] Uwe Mauer, Asim Smailagic, Daniel P. Siewiorek and Michael Deisher, "Activity recognition and monitoring using multiple sensors on different body positions," *International Workshop on Wearable and Implantable Body Sensor Networks*, Washington DC, IEEE Computer Society, 2006.
- [83] Daniele Riboni and Claudio Betini, "Cosar: hybrid reasoning for context-aware activity recognition," *Personal and Ubiquitous Computing*, vol.15, pp.271-289, 2011.
- [84] C. Zhu and W. Sheng, "Human daily activity recognition in robot-assisted living using multi-sensor fusion," in *IEEE International Conference on Robotics and Automation*, pp.2154-2159, 2009.
- [85] Donald F. Specht, "Probabilistic Neural Networks", *Neural Networks Vol.3* pp.109-118, Aug.1990.
- [86] Donald F. Specht, "Probabilistic neural networks for classification mapping and associative memory," *IEEE International Conference on Neural Networks*, vol.1, Page(s): 525 - 532, July 1988.

## 7 Appendix

### 7.1 Appendix I: Time Domain and Frequency Domain Data

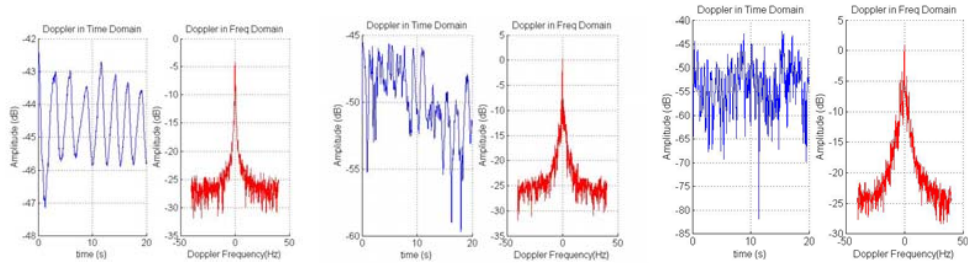


Figure 24: Time Domain and Frequency Domain, Back to Right Hip, Standing, Walking, Jogging, 400 MHz

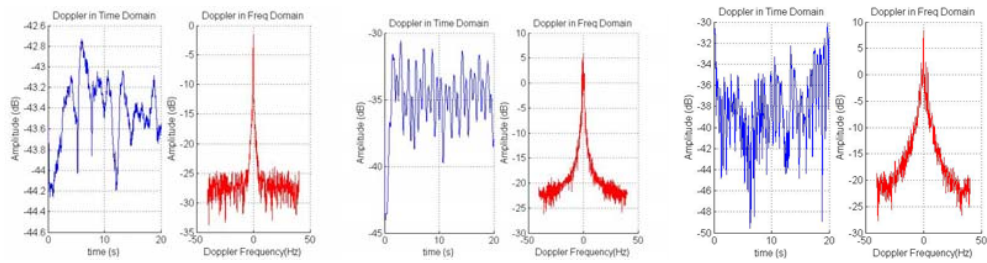


Figure 25: Time Domain and Frequency Domain, Left Wrist to Right Hip, Standing, Walking, Jogging, 400 MHz

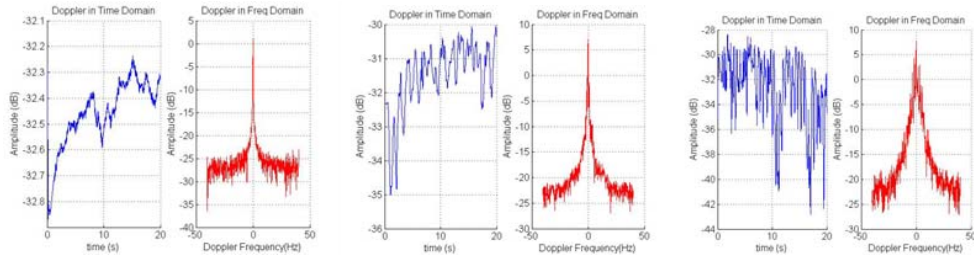


Figure 26: Time Domain and Frequency Domain, Left Ankle to Right Hip, Standing, Walking, Jogging, 400 MHz

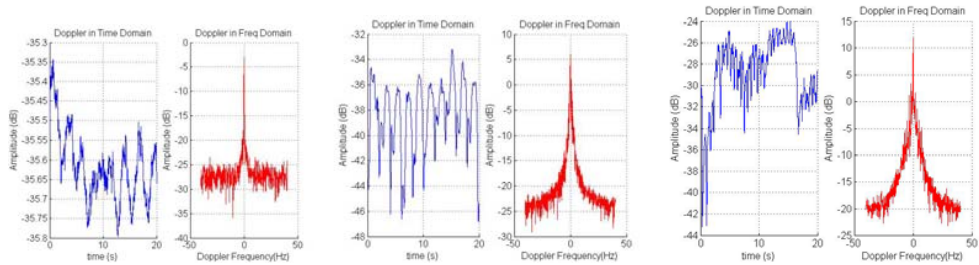


Figure 27: Time Domain and Frequency Domain, Right Ankle to Right Hip, Standing, Walking, Jogging, 400 MHz

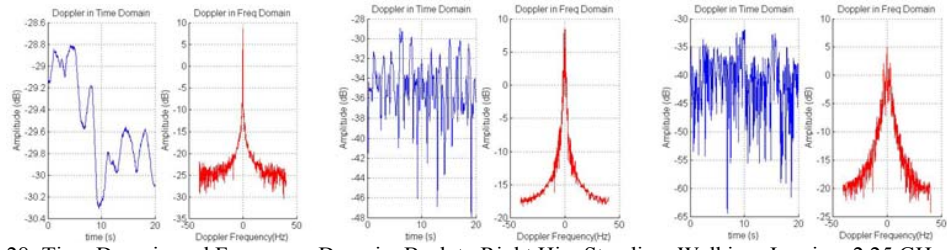


Figure 28: Time Domain and Frequency Domain, Back to Right Hip, Standing, Walking, Jogging, 2.25 GHz

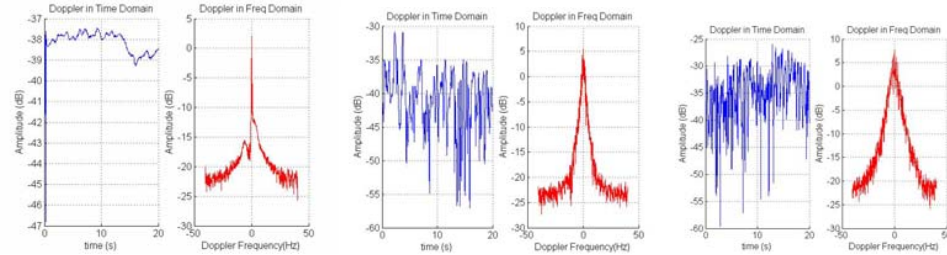


Figure 29: Time Domain and Frequency Domain, Left Wrist to Right Hip, Standing, Walking, Jogging, 2.25 GHz

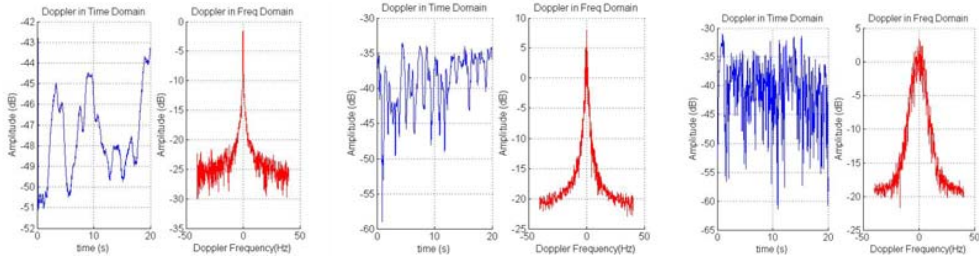


Figure 30: Time Domain and Frequency Domain, Left Ankle to Right Hip, Standing, Walking, Jogging, 2.25 GHz

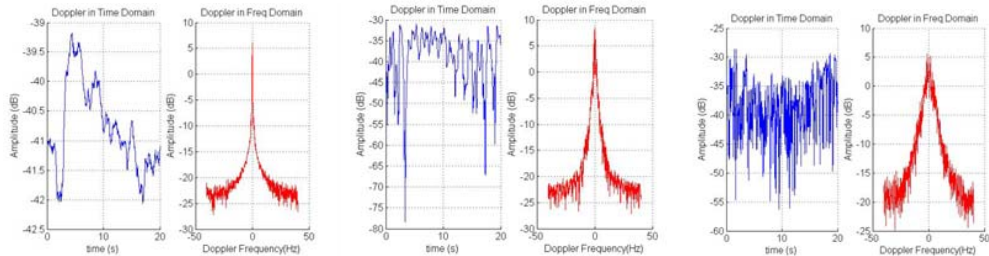


Figure 31: Time Domain and Frequency Domain, Right Ankle to Right Hip, Standing, Walking, Jogging, 2.25 GHz

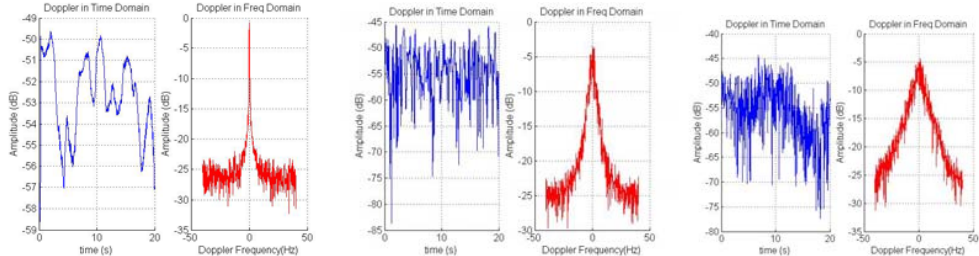


Figure 32: Time Domain and Frequency Domain, Back to Right Hip, Standing, Walking, Jogging, 4.5 GHz

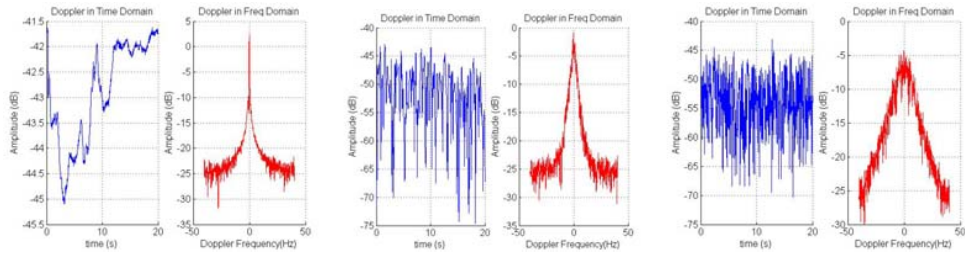


Figure 33: Time Domain and Frequency Domain, Left Wrist to Right Hip, Standing, Walking, Jogging, 4.5 GHz

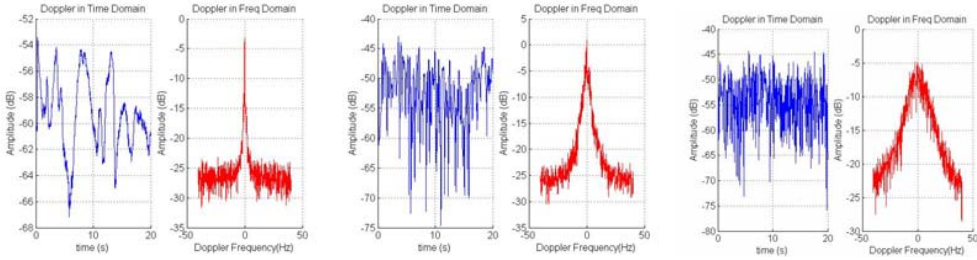


Figure 34: Time Domain and Frequency Domain, Left Ankle to Right Hip, Standing, Walking, Jogging, 4.5 GHz

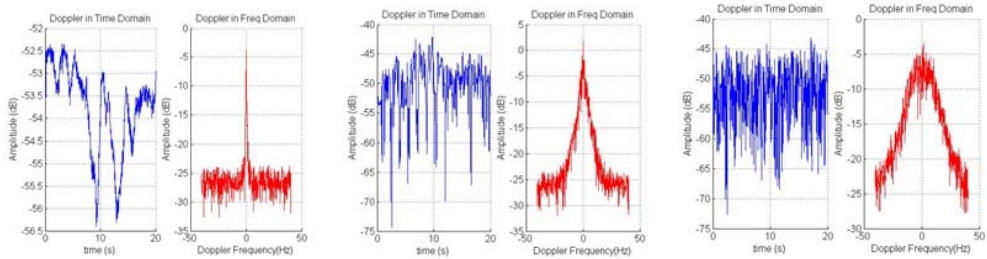


Figure 35: Time Domain and Frequency Domain, Right Ankle to Right Hip, Standing, Walking, Jogging, 4.5 GHz

## 7.2 Appendix II: Statistical Distribution

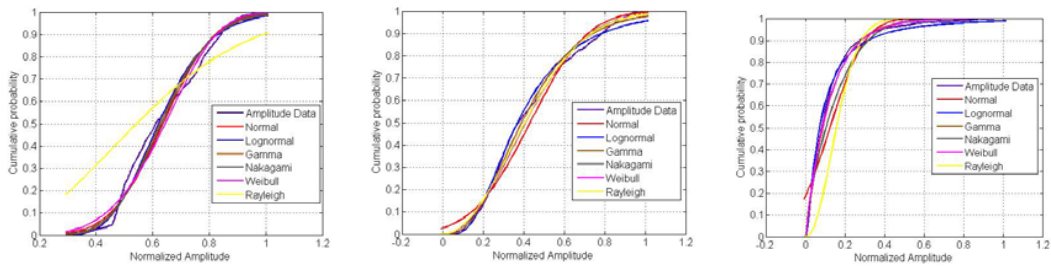


Figure 36: Statistical Distribution, Back to Right Hip, Standing, Walking, Jogging, 400 MHz

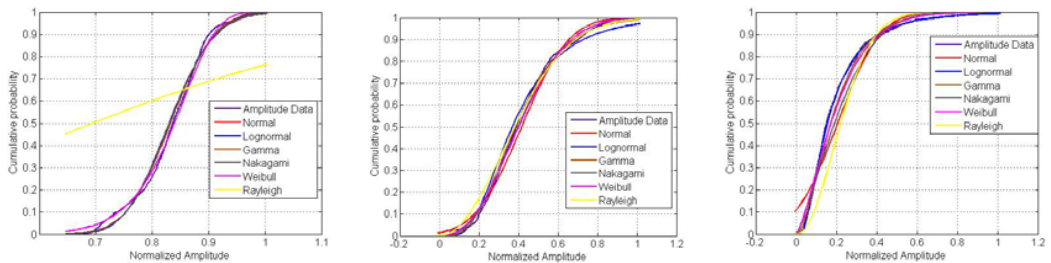


Figure 37: Statistical Distribution, Left Wrist to Right Hip, Standing, Walking, Jogging, 400 MHz

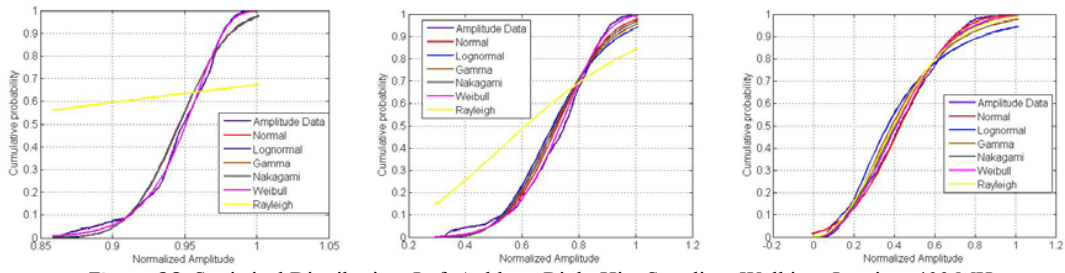


Figure 38: Statistical Distribution, Left Ankle to Right Hip, Standing, Walking, Jogging, 400 MHz

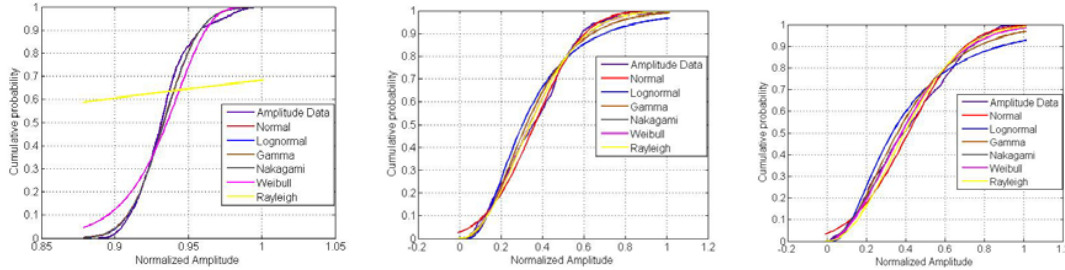


Figure 39: Statistical Distribution, Right Ankle to Right Hip, Standing, Walking, Jogging, 400 MHz

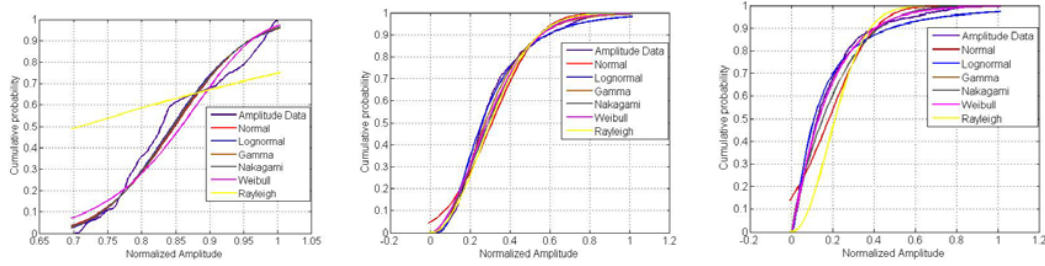


Figure 40: Statistical Distribution, Back to Right Hip, Standing, Walking, Jogging, 2.25 GHz

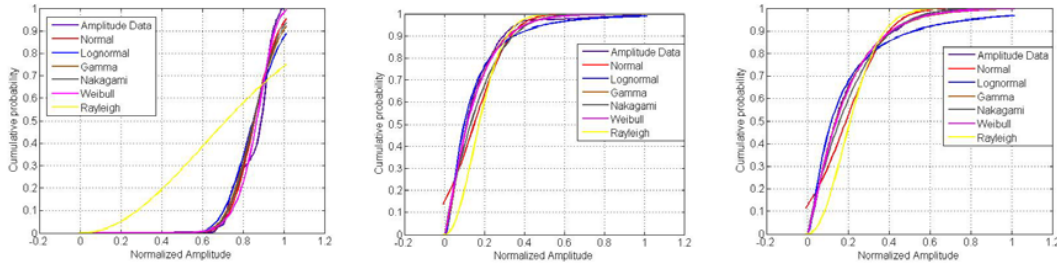


Figure 41: Statistical Distribution, Left Wrist to Right Hip, Standing, Walking, Jogging, 2.25 GHz

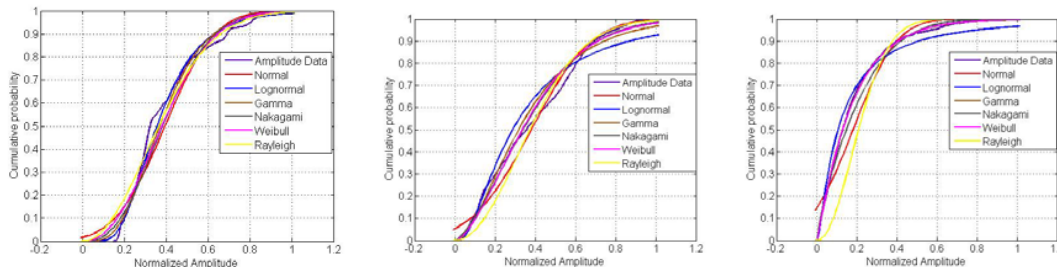


Figure 42: Statistical Distribution, Left Ankle to Right Hip, Standing, Walking, Jogging, 2.25 GHz

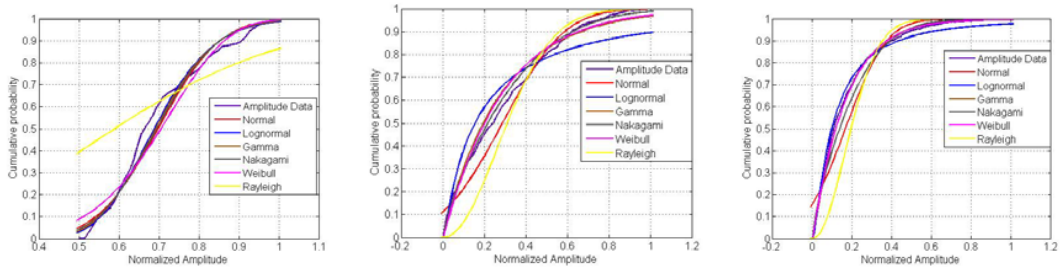


Figure 43: Statistical Distribution, Right Ankle to Right Hip, Standing, Walking, Jogging, 2.25 GHz

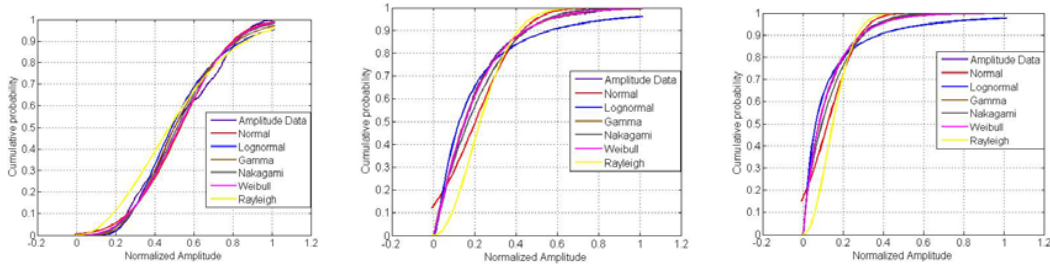


Figure 44: Statistical Distribution, Back to Right Hip, Standing, Walking, Jogging, 4.5 GHz

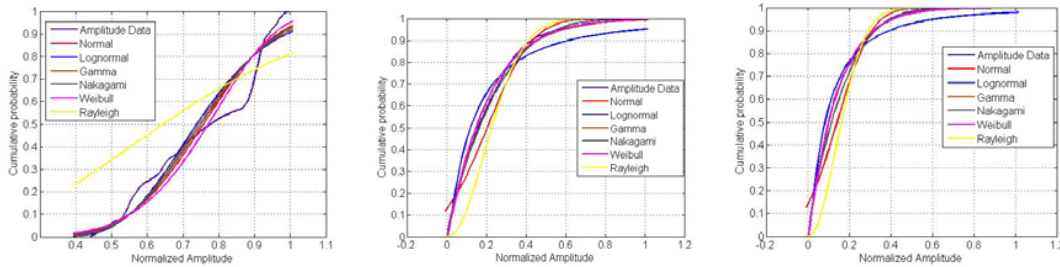


Figure 45: Statistical Distribution, Left Wrist to Right Hip, Standing, Walking, Jogging, 4.5 GHz

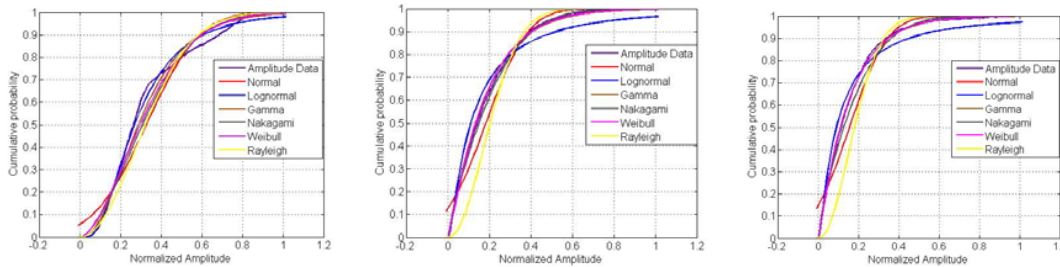


Figure 46: Statistical Distribution, Left Ankle to Right Hip, Standing, Walking, Jogging, 4.5 GHz

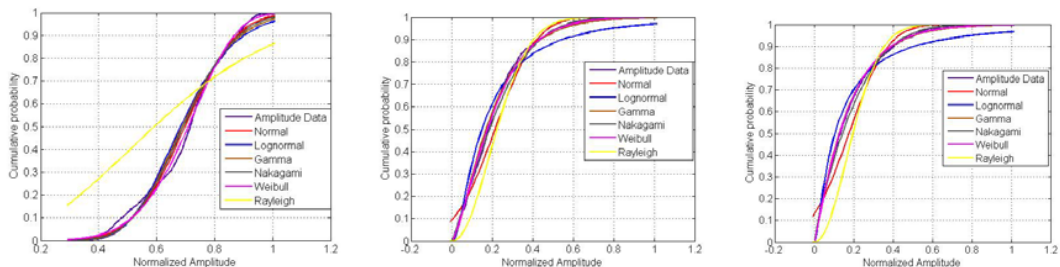


Figure 47: Statistical Distribution, Right Ankle to Right Hip, Standing, Walking, Jogging, 4.5 GHz

### 7.3 Appendix III: Level Crossing Rate

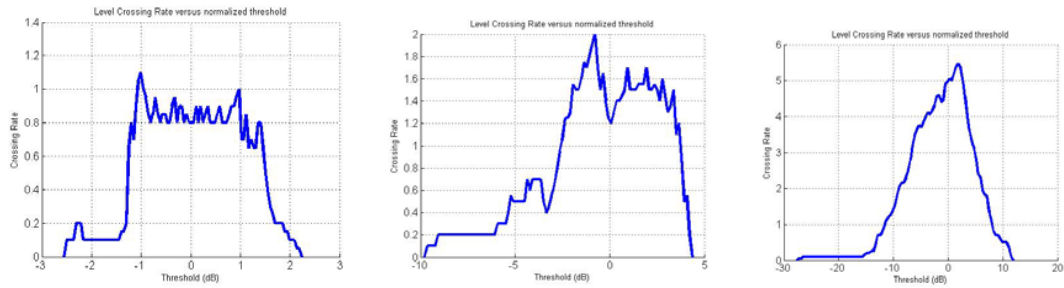


Figure 48: Level Crossing Rate, Back to Right Hip, Standing, Walking, Jogging, 400 MHz

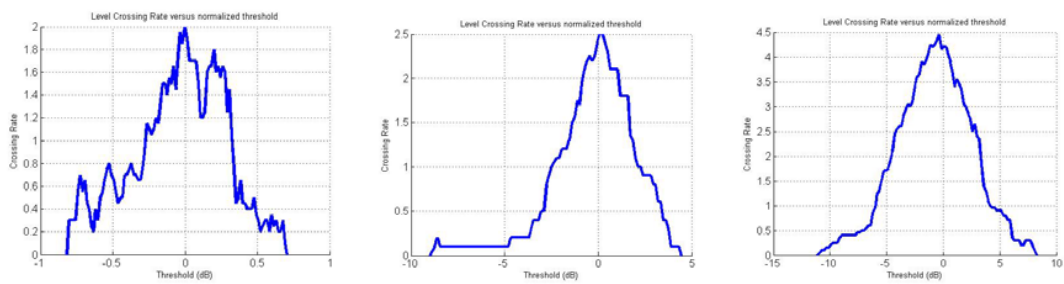


Figure 49: Level Crossing Rate, Left Wrist to Right Hip, Standing, Walking, Jogging, 400 MHz

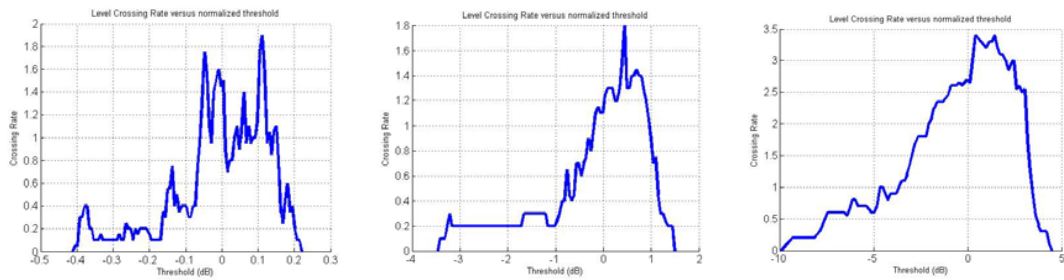


Figure 50: Level Crossing Rate, Left Ankle to Right Hip, Standing, Walking, Jogging, 400 MHz

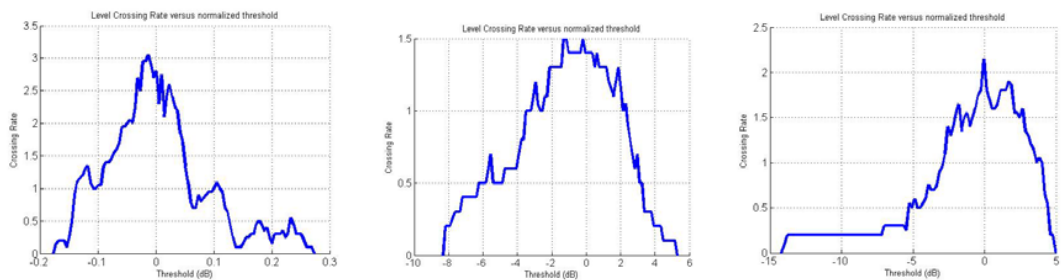


Figure 51: Level Crossing Rate, Right Ankle to Right Hip, Standing, Walking, Jogging, 400 MHz

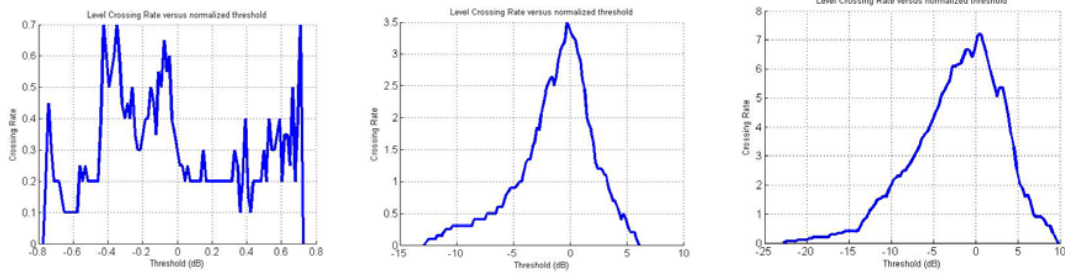


Figure 52: Level Crossing Rate, Back to Right Hip, Standing, Walking, Jogging, 2.25 GHz

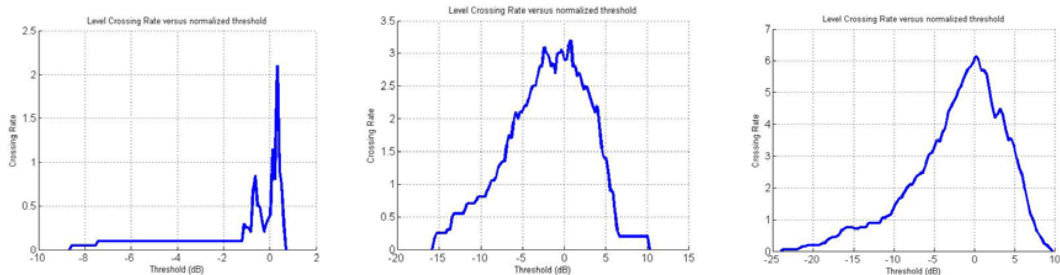


Figure 53: Level Crossing Rate, Left Wrist to Right Hip, Standing, Walking, Jogging, 2.25 GHz

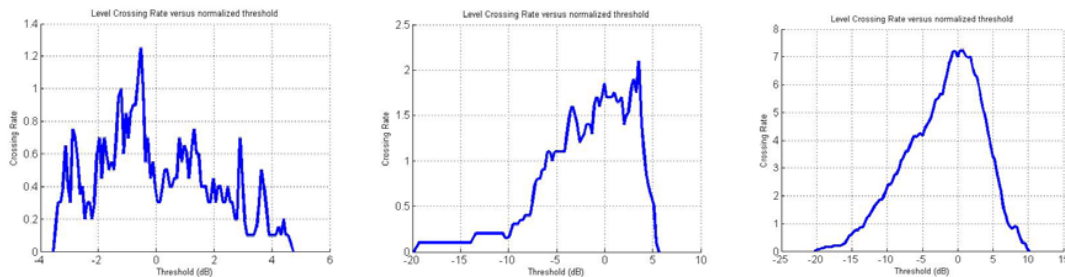


Figure 54: Level Crossing Rate, Left Ankle to Right Hip, Standing, Walking, Jogging, 2.25 GHz

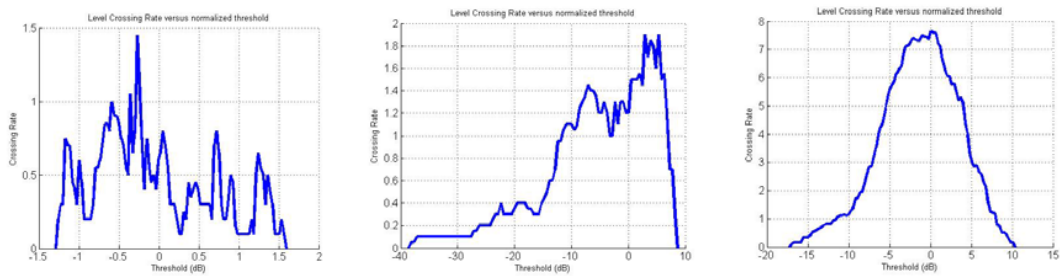


Figure 55: Level Crossing Rate, Right Ankle to Right Hip, Standing, Walking, Jogging, 2.25 GHz

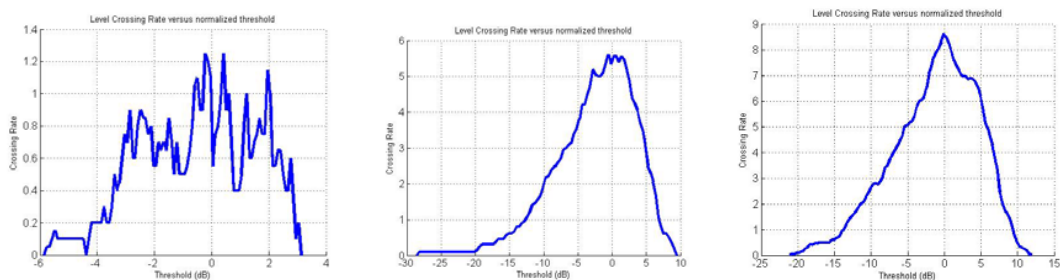


Figure 56: Level Crossing Rate, Back to Right Hip, Standing, Walking, Jogging, 4.5 GHz

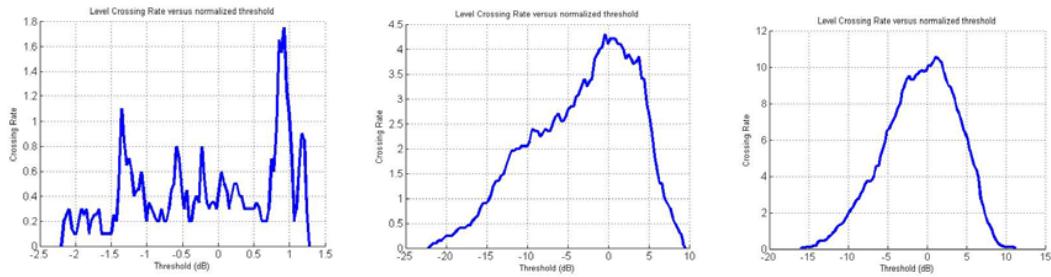


Figure 57: Level Crossing Rate, Left Wrist to Right Hip, Standing, Walking, Jogging, 4.5 GHz

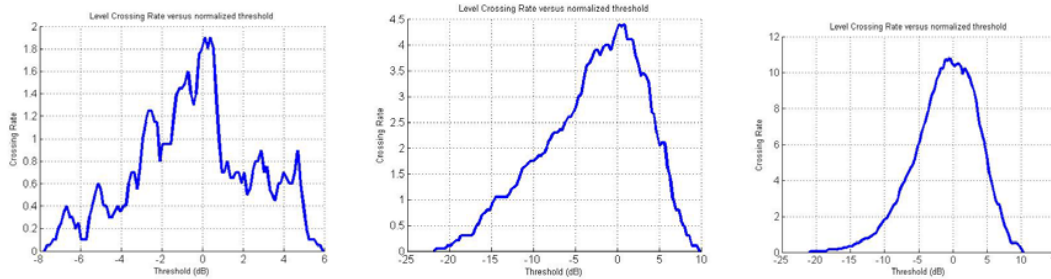


Figure 58: Level Crossing Rate, Left Ankle to Right Hip, Standing, Walking, Jogging, 4.5 GHz

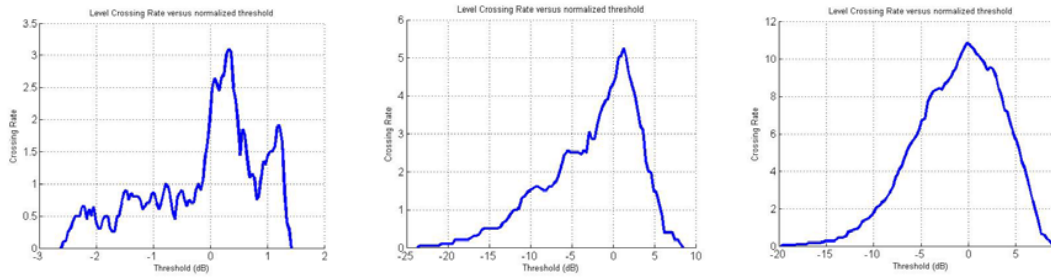


Figure 59: Level Crossing Rate, Right Ankle to Right Hip, Standing, Walking, Jogging, 4.5 GHz

## 7.4 Appendix IV: Averaged Fade Duration

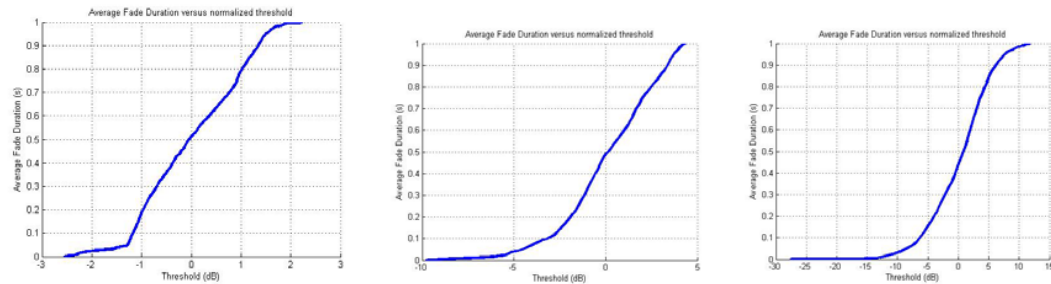


Figure 60: Averaged Fade Duration, Back to Right Hip, Standing, Walking, Jogging, 400 MHz

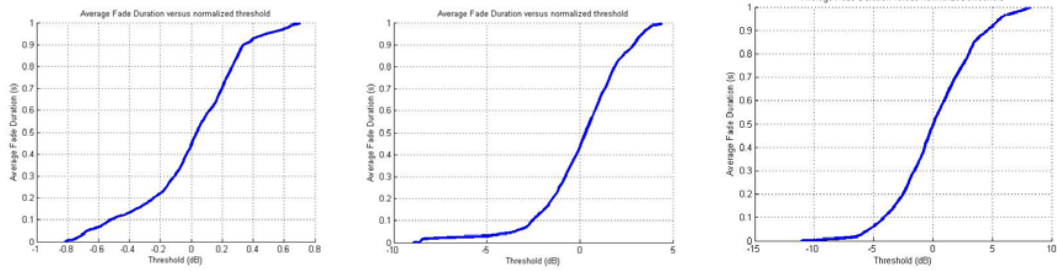


Figure 61: Averaged Fade Duration, Left Wrist to Right Hip, Standing, Walking, Jogging, 400 MHz

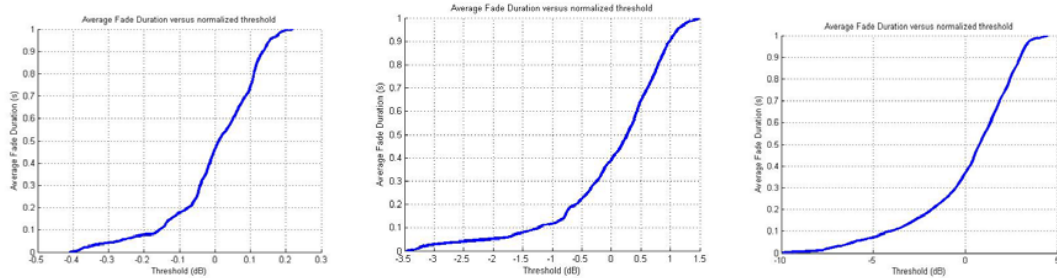


Figure 62: Averaged Fade Duration, Left Ankle to Right Hip, Standing, Walking, Jogging, 400 MHz

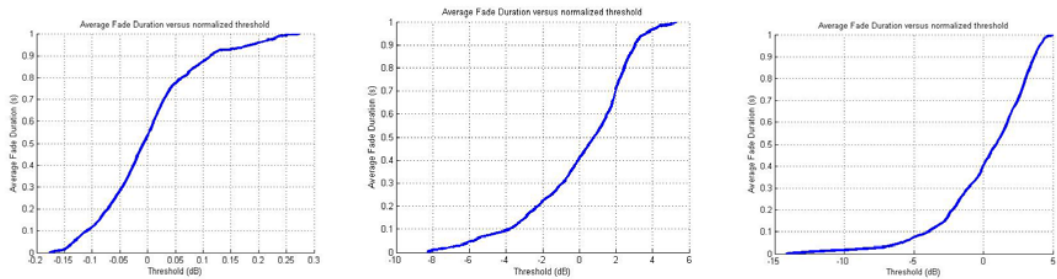


Figure 63: Averaged Fade Duration, Right Ankle to Right Hip, Standing, Walking, Jogging, 400 MHz

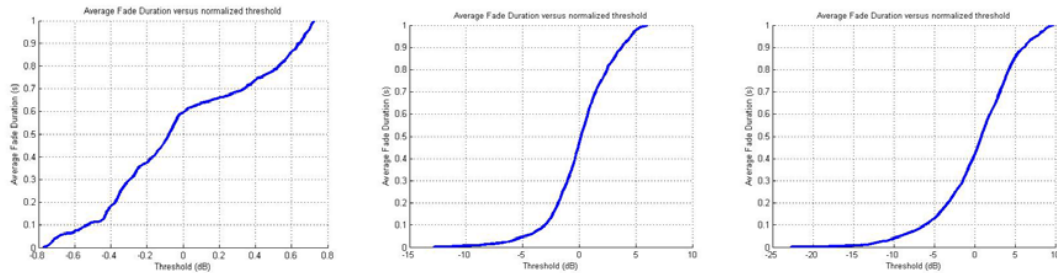


Figure 64: Averaged Fade Duration, Back to Right Hip, Standing, Walking, Jogging, 2.25 GHz

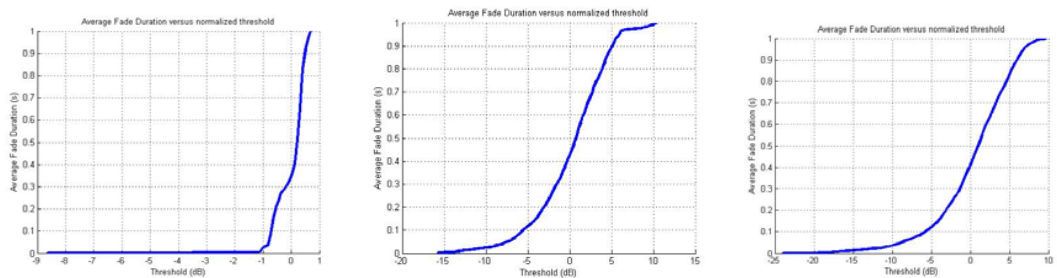


Figure 65: Averaged Fade Duration, Left Wrist to Right Hip, Standing, Walking, Jogging, 2.25 GHz

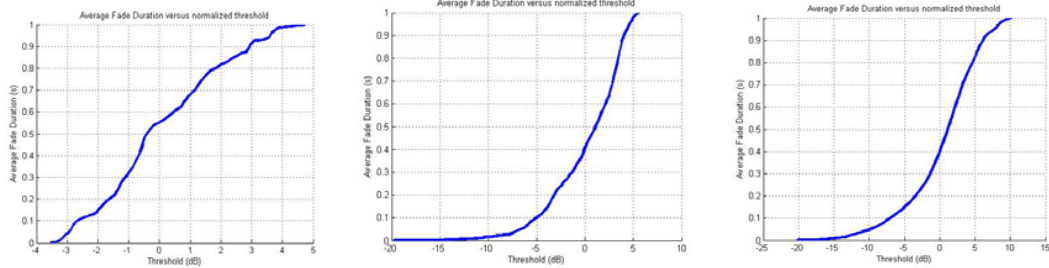


Figure 66: Averaged Fade Duration, Left Ankle to Right Hip, Standing, Walking, Jogging, 2.25 GHz

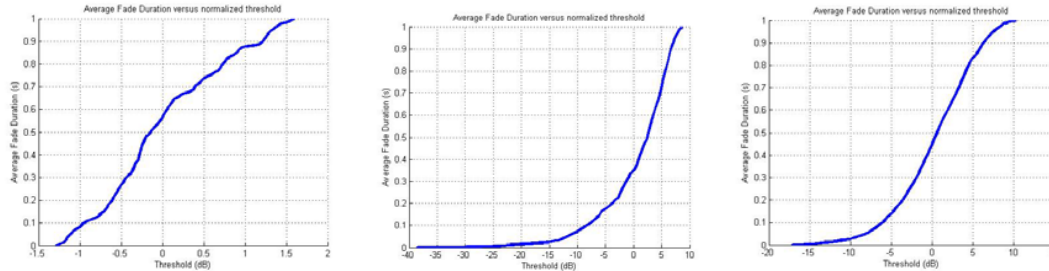


Figure 67: Averaged Fade Duration, Right Ankle to Right Hip, Standing, Walking, Jogging, 2.25 GHz

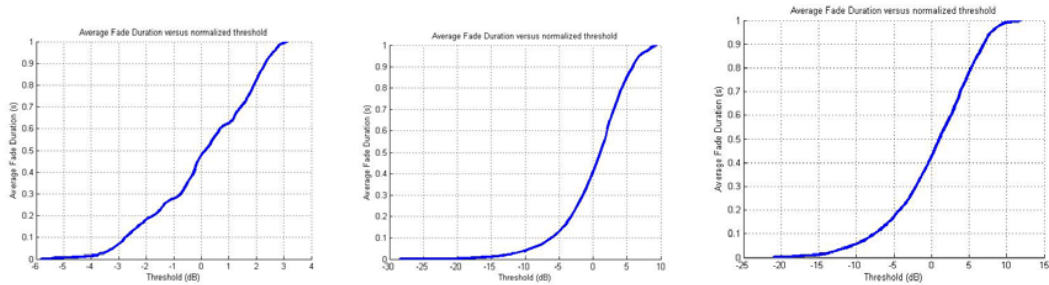


Figure 68: Averaged Fade Duration, Back to Right Hip, Standing, Walking, Jogging, 4.5 GHz

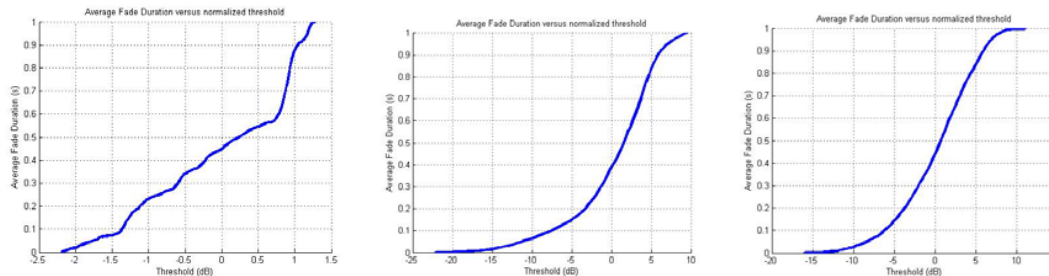


Figure 69: Averaged Fade Duration, Left Wrist to Right Hip, Standing, Walking, Jogging, 4.5 GHz

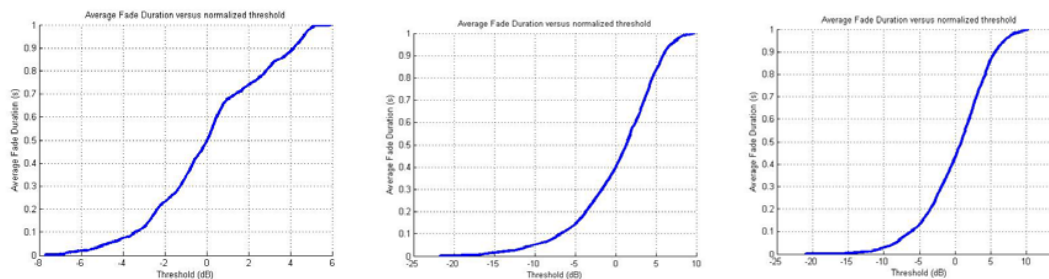


Figure 70: Averaged Fade Duration, Left Ankle to Right Hip, Standing, Walking, Jogging, 4.5 GHz

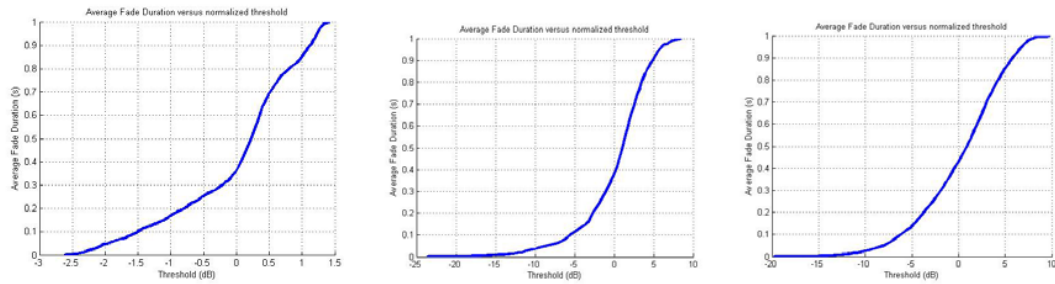


Figure 71: Averaged Fade Duration, Right Ankle to Right Hip, Standing, Walking, Jogging, 4.5 GHz

## 7.5 Appendix V: Coherence Time

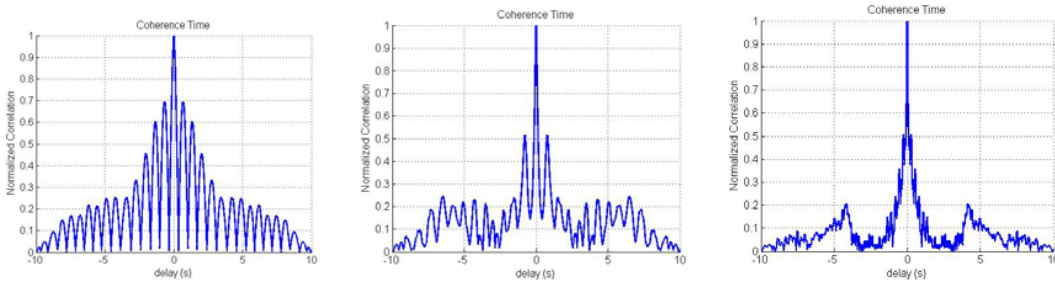


Figure 72: Coherence Time, Back to Right Hip, Standing, Walking, Jogging, 400 MHz

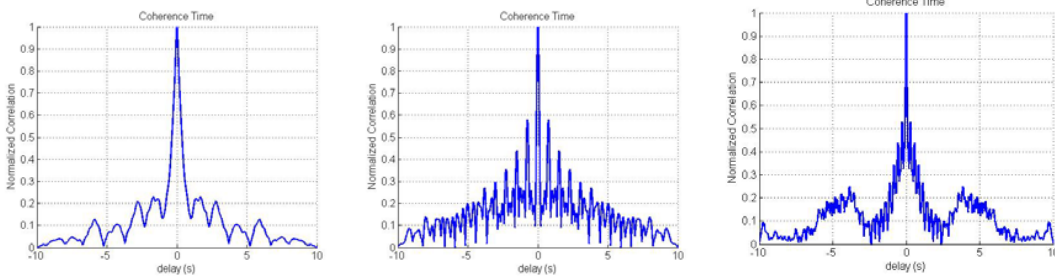


Figure 73: Coherence Time, Left Wrist to Right Hip, Standing, Walking, Jogging, 400 MHz

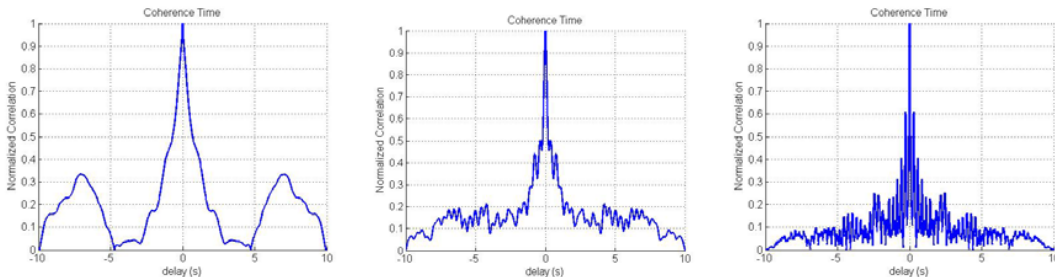


Figure 74: Coherence Time, Left Ankle to Right Hip, Standing, Walking, Jogging, 400 MHz

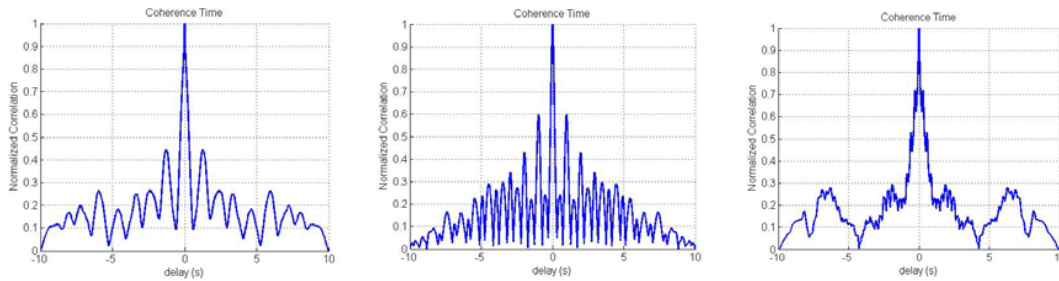


Figure 75: Coherence Time, Right Ankle to Right Hip, Standing, Walking, Jogging, 400 MHz

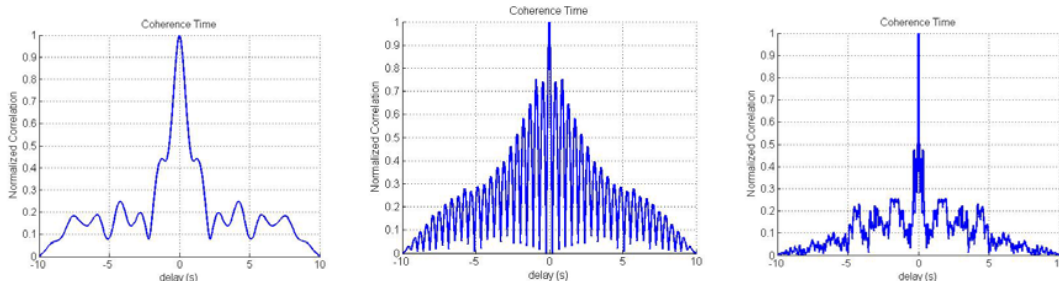


Figure 76: Coherence Time, Back to Right Hip, Standing, Walking, Jogging, 2.25 GHz

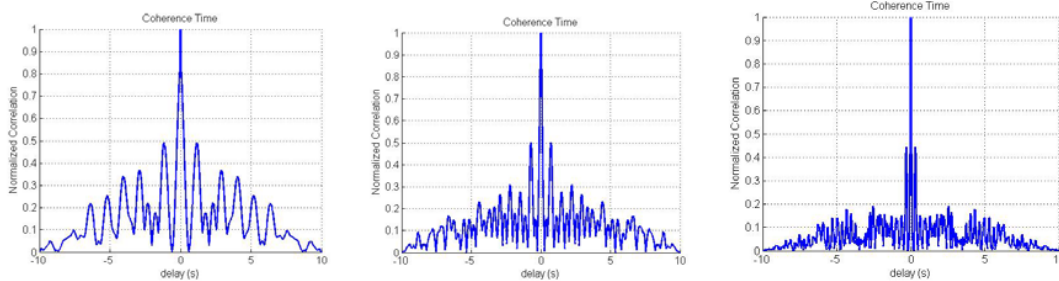


Figure 77: Coherence Time, Left Wrist to Right Hip, Standing, Walking, Jogging, 2.25 GHz

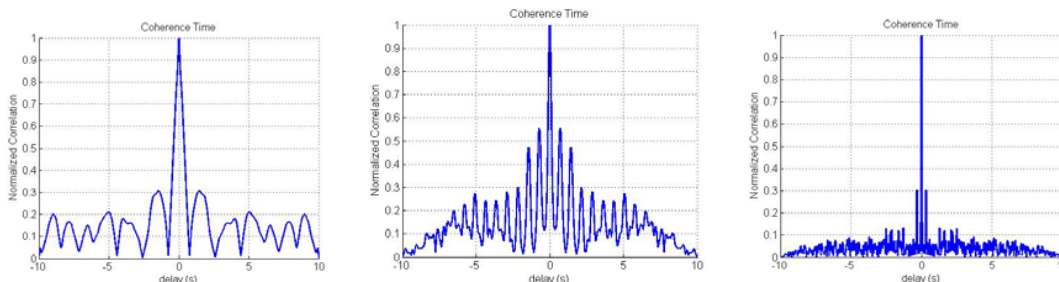


Figure 78: Coherence Time, Left Ankle to Right Hip, Standing, Walking, Jogging, 2.25 GHz

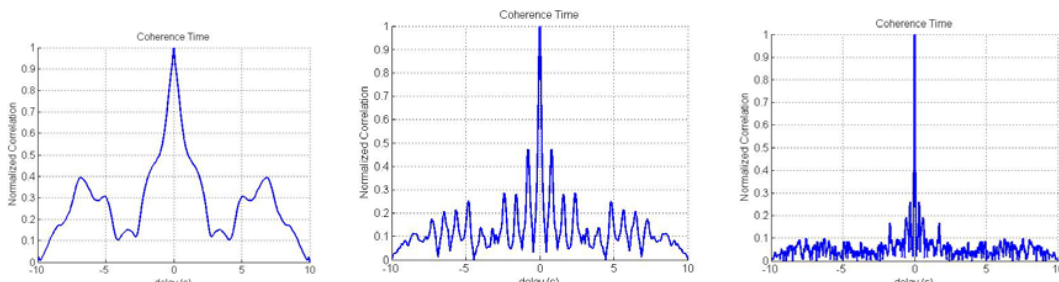


Figure 79: Coherence Time, Right Ankle to Right Hip, Standing, Walking, Jogging, 2.25 GHz

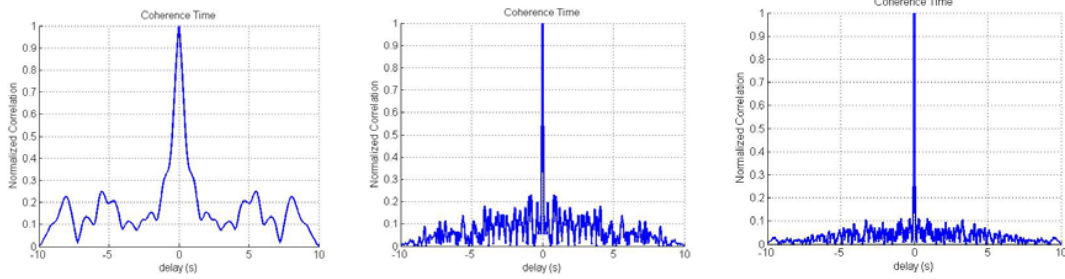


Figure 80: Coherence Time, Back to Right Hip, Standing, Walking, Jogging, 4.5 GHz

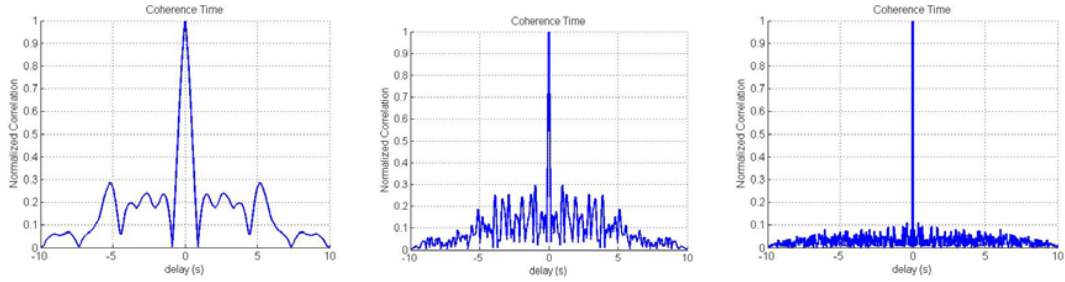


Figure 81: Coherence Time, Left Wrist to Right Hip, Standing, Walking, Jogging, 4.5 GHz

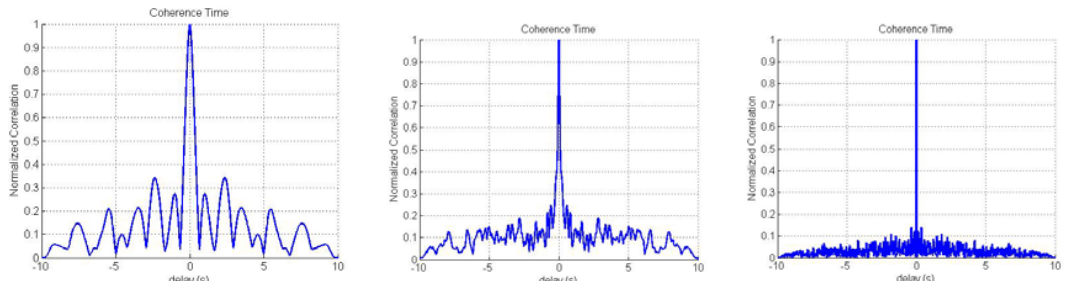


Figure 82: Coherence Time, Left Ankle to Right Hip, Standing, Walking, Jogging, 4.5 GHz

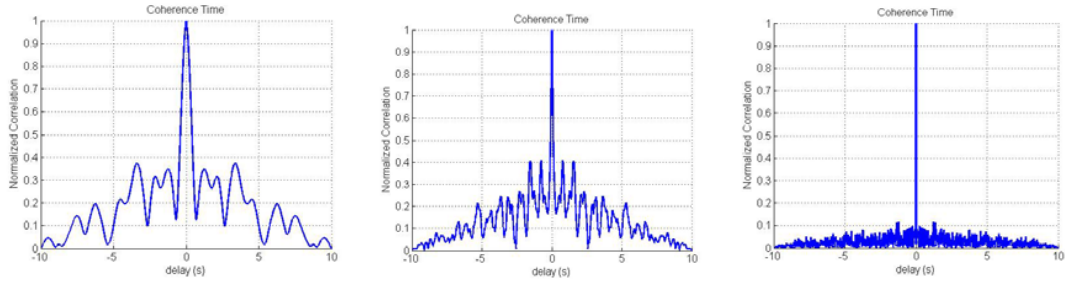


Figure 83: Coherence Time, Right Ankle to Right Hip, Standing, Walking, Jogging, 4.5 GHz